Geometry, kinematics, and Quaternary activity of the brittle Leech River fault zone, southern Vancouver Island, British Columbia, Canada

by

Audrey Graham
Bachelor of Science (Honours), University of Victoria, 2013

A Thesis Submitted in Partial Fulfillment
of the Requirements for the Degree of

MASTER OF SCIENCE

in the School of Earth and Ocean Sciences

© Audrey Graham, 2018
University of Victoria

All rights reserved. This thesis may not be reproduced in whole or in part, by photocopy or other means, without the permission of the author.

Supervisory Committee

Geometry, kinematics, and Quaternary activity of the brittle Leech River fault zone, southern Vancouver Island, British Columbia, Canada

by

Audrey Graham
Bachelor of Science (Honours), University of Victoria, 2013

Supervisory Committee

Dr. Kristin Morell, (School of Earth and Ocean Sciences)
Co-Supervisor

Dr. Victor Levson, (School of Earth and Ocean Sciences)
Co-Supervisor

Dr. Lucinda Leonard, (School of Earth and Ocean Sciences)
Departmental Member

Abstract

Supervisory Committee
Dr. Kristin Morell, (School of Earth and Ocean Sciences)
Co-Supervisor
Dr. Victor Levson, (School of Earth and Ocean Sciences)
Co-Supervisor
Dr. Lucinda Leonard, (School of Earth and Ocean Sciences)
Departmental Member

Southern Vancouver Island lies on the forearc of the Cascadia subduction zone, north of a concave bend in the plate boundary centred around the Olympic Mountains. The bend in the margin coincides with a significant decrease in northward-directed trench-parallel forearc migration, and a network of active crustal faults in the Puget Lowland east of the Olympic Mountains accommodates permanent north-south shortening and transpression. The nature of forearc deformation on southern Vancouver Island is less well constrained, due in part to the unknown extent and kinematics of active crustal faulting. Recent work has shown that a brittle fault zone associated with the Eocene terrane-bounding Leech River fault has produced at least two surface-rupturing earthquakes in the late Quaternary.

I use LiDAR-derived topographic data, slip-sense indicator analysis of slickenlines on fault planes, electrical resistivity tomography (ERT), and ground-penetrating radar (GPR) to investigate the geometry, kinematics, and Quaternary activity along the eastern half of the active, brittle Leech River fault zone. My mapping reveals a complex, near-vertical zone up to 1 km wide and 25 km long that exhibits many characteristics of a strike-slip fault. Displaced Quaternary deposits are observed directly at two sites in the western 8 km of the study area, and inferred through geophysical imagery, topographic data, and liquefaction features to extend to the eastern terrestrial extent of the fault zone towards previously mapped active faults in the Juan de Fuca Strait and the Darrington-Devil's Mountain fault zone in western Washington. I use fault kinematics and geometry to show that the eastern Leech River fault zone has been reactivated as a right-lateral strike-slip fault that accommodates forearc deformation within the modern stress field north of the Olympic Mountains.

Table of Contents

Supervisory Committee ii

Abstract iii

Table of Contents iv

List of Tables vi

List of Figures vii

Acknowledgements viii

1 Introduction 1

2 Background 4

2.1 Tectonic setting 4

2.2 Glacial history 6

3 Methods 8

3.1 Bedrock and surficial mapping 8

3.2 Kinematic and geometric analysis 9

3.3 Electrical resistivity tomography (ERT) 10

3.4 Ground-penetrating radar (GPR) 12

4 Results 14

4.1 Site 1 16

4.2 Site 2 19

4.2.1 Glaciofluvial and fluvial terraces 19

4.2.2 Site 2-A 23

4.2.3 Site 2-B 27

4.2.4 Resistivity and GPR across terraces 30

4.2.5 Site 2 Summary....34
4.3 Site 3....36
4.4 Site 4....41
4.5 Site 5....44
5 Discussion....49
5.1 Late Quaternary activity on the Leech River fault zone....49
5.2 Fault zone geometry....55
5.3 Fault kinematics....56
5.4 Regional Implications....60
6 Conclusions....62
7 References....63
Appendix A: Structural Measurements....75
Appendix B: Site 1 Supplemental Materials....80
Appendix C: Site 2 Supplemental Materials....83
Appendix D: Site 3 Supplemental Materials....102
Appendix E: Site 4 Supplemental Materials....106
Appendix F: Site 5 Supplemental Materials....107

List of Tables

Table 1. Radiocarbon dates from charcoal in terrace deposits at Site 2, and woody material at Site 5.....21

Table 2. Optically Stimulated Luminescence (OSL) ages from quartz and Infrared Stimulated Luminescence (IRSL) ages from feldspar grains in terrace deposits at Site 2.....23

List of Figures

Figure 1. Tectonic setting of the Leech River fault. 2

Figure 2. Riedel Shear schematic and common linkage patterns for a dextral strike-slip fault. Modified from Swanson (2006). 10

Figure 3. Dipole-dipole electrode configuration for electrical resistivity surveys. 11

Figure 4. Generalized structural geomorphic map of the eastern Leech River fault zone. 15

Figure 5. Structural geomorphic map and geophysical imagery from Site 1. 17

Figure 6. Overview of terraces, sample locations, and bedrock exposure at Site 2. 20

Figure 7. Structural data and field photos from Site 2-A. 24

Figure 8. Structural data, field photos, and geophysical profiles from Site 2-B. 29

Figure 9. Proposed fault geometry at Site 2 35

Figure 10. Site 3: Structural geomorphic map, stereonets, field photos, geophysics profiles 37

Figure 11. Site 4: Structural geomorphic map, field photos, topography, geophysics profiles 42

Figure 12. Site 5: Structural geomorphic map, field photos, geophysics profiles 46

Figure 1. Overview of structural data, proposed fault geometry, and regional seismicity. 50

Acknowledgements

Many thanks to Kristin, Lucinda, and Vic for the generous support and mentorship over the course of this project. It was an absolute pleasure to work with all three, and I am very grateful to have had the opportunity to learn from such great scientists both in the field and the office. Thanks also to friends, staff, and faculty at SEOS including David Nelles, Allison Rose, Trevor Mearce, Travis Dawson, Nick Harrichausen, Kendra Colloid, Maria Thorlakson and Theron Finlay for the productive conversations and for making the process enjoyable. Special thanks to Lucinda for all the heavy lifting, and also to Jan Bednarski, Daniel Scanks, Tabor Reedy, and Eva Zhang for the good-natured field assistance during geophysical surveys in sometimes trying terrain. Revisions from Vic greatly improved the robustness of this document. Charly Bank (University of Toronto) generously loaned us his GPR equipment and software license, and Dean Goodman loaned me his time for technical support. My education was supported and enhanced Drs. Christine Regalla, Christie Rowe, Jamie Kirkpatrick, Scott Bennett, and Colin Amos. None of the fieldwork would have been possible without access and support from the CRD watershed crew, especially Sharon Scott and Ron and Nathan at the Goldstream Gate. Lastly, thanks to my amazing friends and family for the motivation and support over the past two and a half years.

1 Introduction

The Canadian Cordillera is often conceptualized as an amalgamation of geologic terranes sequentially accreted to the western margin of the continent through collision of crustal fragments (e.g. Monger et al., 1982; English and Johnston, 2005; Colpron et al., 2007; Johnston, 2008). The Leech River fault, on southern Vancouver Island, British Columbia, Canada, has long been recognized as an important terrane-bounding structure responsible for accretion of the oceanic Crescent terrane to western North America during a significant orogenic event in the late Eocene to early Oligocene (Fairchild and Cowan, 1982; Clowes et al., 1987; Groome et al., 2003). Striking parallel to the lithologic Leech River fault, a complex brittle fault zone comprising 2 – 4 steeply dipping mappable strands is inferred to have experienced left-lateral activity during the accretionary tectonic regimes of the Eocene and Miocene (Fairchild, 1980; Fairchild and Cowan, 1982). More recently, the Leech River fault zone has been shown to have experienced activity in the latest Quaternary (Morell et al., 2017), making it the first recognized active terrestrial fault in southern Canada. The role that the active, brittle Leech River fault zone plays in accommodating deformation of the Cascadia forearc has important implications for regional deformation in the upper crust.

At many of the world's subduction zones, forearcs experience trench-parallel migration (e.g. forearc slivers; Bellier and Sebrier, 1995; Andronicos et al., 1999; Montero et al., 2013), which is influenced by the rheology of the forearc (Lange et al., 2008), relative plate motion obliquity (McCaffrey, 1992), and margin geometry (Beck et al., 1993; Wang, 1996). In southern Cascadia, oblique convergence between the Juan de Fuca and North American plates leads to northward translation of the forearc in Oregon and Washington, often approximated by clockwise rotation of semi-rigid crustal blocks (Wells and Simpson, 2001; McCaffrey et al., 2007; McCaffrey et al., 2013). Near the latitude of the Olympic Mountains, a concave bend in the plate margin results in a decrease in relative plate motion obliquity to the north (Fig. 1; Beck et al., 1993), and a coincident long-term north-south shortening of the forearc by 5 – 6 mm/yr (Mazzotti et al., 2002). Despite extensive Pleistocene glaciations and vegetation, workers have defined a network of crustal faults inland of the Olympic Mountains in the Puget Lowland that currently accommodates permanent margin-parallel shortening on the order of 3 – 3.5 mm/yr (Mazzotti et al., 2002).

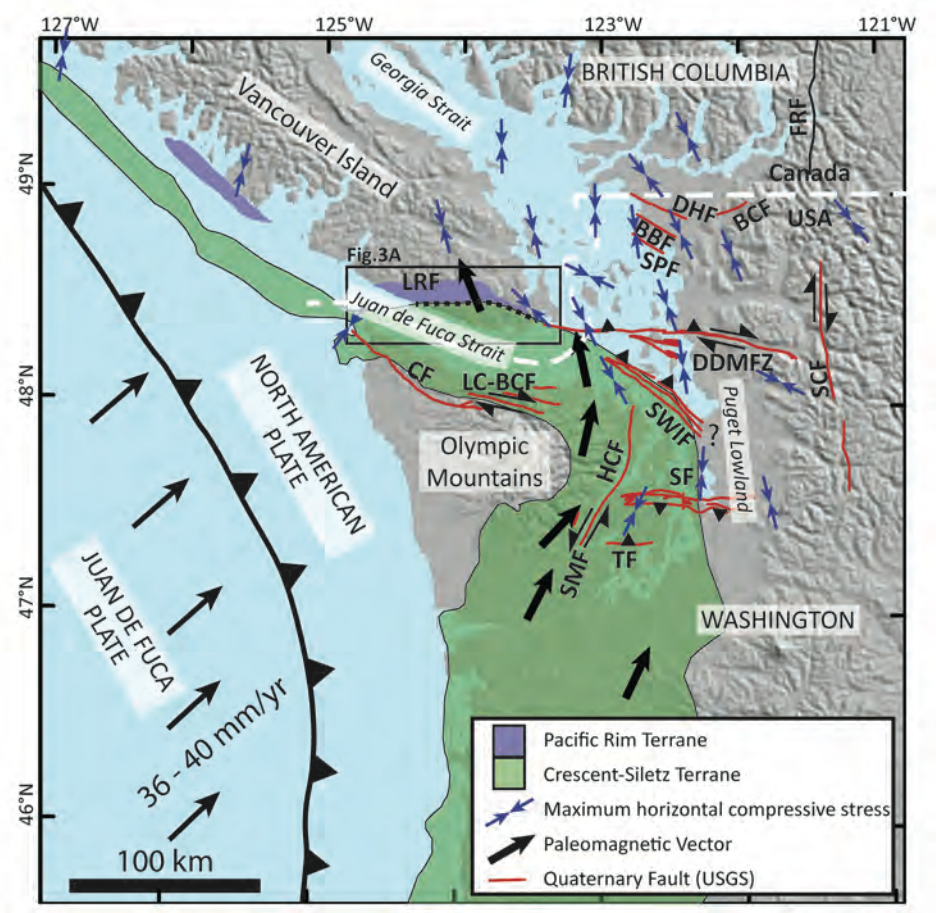

Figure 2. Tectonic setting of the Leech River fault (LRF) at the northern margin of the Crescent-Siletz terrane 'horseshoe' (McCrory and Wilson, 2013). Exposed Pacific Rim terrane on Vancouver Island (Massey et al., 2005). Juan de Fuca plate motion relative to stable North America (DeMets et al., 2010). Paleomagnetic vectors (Beck and Engebretson, 1982) of basalt and maximum horizontal compressive stress from borehole breakouts and crustal seismicity (Balfour et al., 2011; Heidbach et al., 2016). Quaternary faults (USGS, 2010): BBF: Bellingham Basin fault; BCF: Border Creek fault; CF: Calawah fault; DDMFZ: Darrington-Devil's Mountain fault zone; DHF: Drayton Harbour fault (Kelsey et al., 2012); HCF: Hood Canal fault; LC-BCF: Lake Creek-Boundary Creek fault (Nelson et al., 2017); LCF: Little Creek fault; SF: Seattle fault; SPF: Sandy Point fault; SWIF: Southern Whidbey Island fault; TF: Tacoma fault.

However, in southwest BC, evidence for crustal fault activity during or after the Fraser glaciation, in the late Quaternary, remains elusive in part due to the additional challenge of slow strain rates (Mazzotti et al., 2003; McCaffrey et al., 2013). Recent work indicating Quaternary activity along the brittle Leech River fault zone (Bednarski

, 2016; Morell et al., 2017) and its potential offshore equivalent in the Juan de Fuca Strait (Darrington-Devil's Mountain fault zone (DDMFZ) Fig. 1; Barrie and Greene, 2015) demonstrates that the active fault network of western Washington extends west onto southern Vancouver Island.

Here I document evidence for reactivation of the terrane-bounding Leech River fault as a complex brittle structure that actively accommodates forearc strain in southwest BC, north of the Olympic Mountains. I use field observations and measurements of both bedrock and Quaternary deposits to characterize the eastern 25 km of the active, brittle Leech River fault zone, which intersects the coast within 5 km of the city of Victoria (Fig. 1). My results show that the eastern Leech River fault zone comprises a network of several mesoscale brittle faults that cut through bedrock and Quaternary deposits on either side of the ductilely deformed Eocene terrane-bounding Leech River fault. I constrain the kinematic evolution of the brittle structure, with emphasis on the most recent (late Quaternary) activity of the fault zone, using a combination of methods including analysis of slip-sense indicators on slickenlined fault planes, mapping of fault strand geometry, and LiDAR-based topographic analysis. Electrical resistivity tomography (ERT) and ground-penetrating radar (GPR) are used to image Quaternary deposits and bedrock beneath topographic lineaments. My work implies that the Leech River fault zone has been reactivated as a dextral transpressive structure in the present-day stress field of the Cascadia subduction zone, likely as one of a network of active crustal faults that accommodates forearc strain north of the Olympic Mountains.

2 Background

2.1 Tectonic setting

The lithologic Leech River fault originated in the early Eocene when the oceanic Metchosin Igneous Complex of the Crescent terrane was juxtaposed with the meta-accretionary Leech River Complex of the Pacific Rim terrane (Fairchild and Cowan, 1982; Groome et al., 2003). At depth, the terrane-bounding structure dips ~45° towards the northeast, which has led to its interpretation as a subduction thrust (Clowes et al., 1987). To the south, the Crescent terrane extends into the Siletz terrane, a thick (≤ 35 km) oceanic plateau (Trehu et al., 1994; Phillips et al., 2017) that underlies western Oregon and Washington (McCrory and Wilson, 2013). Paleomagnetic declination measurements from basalt exposures of the Crescent-Siletz terrane fan outward around the core of the Olympic Mountains (Fig. 1), suggesting that the terrane experienced structural arching to the east following its accretion (48 – 45 Ma), possibly initiating the formation of the Olympic Mountains through oroclinal bending (Muller, 1977; Beck and Engebretson, 1982; Wells et al., 2014). It has been proposed that left-lateral motion on the Leech River fault throughout the Eocene merged into east-dipping thrusts east of the Olympic Mountains to accommodate this bending (Fairchild, 1979; Muller, 1977). The presence of undeformed late Eocene – Oligocene Carmanah Group sediments above the lithologic Leech River fault at its western extent has been cited previously as evidence that the fault has been inactive since the Eocene (MacLeod et al., 1977; Muller, 1977; Fairchild and Cowan, 1982). However, ~38 km along strike to the east, observations of faulted late Quaternary colluvial units indicates that the eastern half of the brittle Leech River fault zone has been active within the past 15 ka (Morell et al., 2017).

Modern deformation on southern Vancouver Island is the result of ongoing subduction of the Juan de Fuca plate, and can be described in terms of elastic and permanent components (Mazzotti et al., 2002). Margin-normal strain accumulates in the forearc during the interseismic period of the earthquake cycle, and is released elastically with the rupture of the megathrust (Mazzotti et al., 2003; Leonard et al., 2004). Despite the predominance of margin-normal strain in geodetic measurements, crustal seismicity and borehole breakouts indicate a predominantly margin-parallel crustal stress field throughout the northern Cascadia forearc (Wells and Heller,

1988; Wang, 2000; Balfour et al., 2011). On southern Vancouver Island, inversions of crustal earthquake fault plane solutions reveal a crustal stress field dominated by northwest-southeast-directed compression, significantly oblique to the convergence direction (Fig. 1, Balfour et al., 2011). The concentration of crustal seismicity in the Cascadia forearc at depths of 15 – 25 km (Johnson et al., 1999) around the flanks of the Olympic Mountains (Mulder, 1995; Balfour et al., 2011), coincides with a network of mapped active faults.

High-resolution LiDAR-derived topographic data (Haugerud et al., 2003; Sherrod et al., 2004) have been used with a variety of supporting methods to define a network of active crustal faults in the Puget Lowland, east of the Olympic Mountains (Fig.1). The fault kinematics vary from south to north along the margin, overall accommodating predominantly north-south compression and transpression (Johnson et al., 1999; Johnson et al., 2004a). To the southeast of the Olympic Mountains, topographic scarps and geophysical anomalies (Sherrod et al., 2004), seismic reflection profiles (Johnson et al., 1999), and paleoseismic trenching (Kelsey et al., 2008; Blakely et al., 2009) have been used to identify late Quaternary activity on the Saddle Mountain fault zone (SMFZ), the Hood Canal fault (HCF), and the Tacoma (TF) and Seattle (SF) faults. The north-northeast-striking Hood Canal and Saddle Mountain faults are shown to be primarily left-lateral transpressional, whereas the east-west striking Seattle and Tacoma faults have primarily accommodated north-south shortening and uplift along high-angle reverse faults during the Quaternary (Blakely et al., 2002; Johnson et al., 2004a; Sherrod et al., 2004).

On the northern flank of the Olympic Mountains, east-west-striking faults including the Calawah (CF), Lake Creek-Boundary Creek (LC-BCF), Darrington-Devil's Mountain (DDMFZ), and Leech River (LRF) faults experienced left-lateral motion in response to accretionary tectonics in the Eocene to Miocene (MacLeod et al., 1977; Fairchild and Cowan, 1982; Johnson, 1984; Personius et al., 2014; Nelson et al., 2017). However, LiDAR analysis and paleoseismic trenching indicate that both the Lake Creek-Boundary Creek fault (Nelson et al., 2017), and the Darrington-Devil's Mountain fault zone (Hayward et al., 2006; Personius et al., 2014), have experienced right-lateral activity in the Holocene. The Calawah fault (CF), which juxtaposes the Olympic Accretionary Complex and Crescent terrane basalt, has also been shown to be active in the late Quaternary,

though the kinematics are poorly constrained (MacLeod et al., 1977). To the east, both the Southern Whidbey Island fault (SWIF) and Darrington-Devil's Mountain fault zone (DDMFZ) have experienced coseismic slip within 2.7 and 2 ka, respectively (Sherrod et al., 2008; Personius et al., 2014). The Southern Whidbey Island fault, which has experienced at least four Holocene earthquakes, forms the northeastern contact of the Crescent terrane, and its positive flower structure geometry suggests it accommodates transpression (Johnson et al., 1996). Seafloor seismic profiling has been used to extend both the Southern Whidbey Island fault (Sherrod et al., 2008; USGS, 2010) and the Darrington-Devil's Mountain fault zone (Barrie and Greene, 2015) across the Juan de Fuca Strait toward southern Vancouver Island and the eastern terrestrial extent of the Leech River fault zone (Fig. 1).

2.2 Glacial history

Vancouver Island and the Puget Lowland experienced at least three Pleistocene glaciations, most recently the Fraser glaciation in the Late Wisconsinan (Alley and Chatwin, 1979; Blaise et al., 1990), when the Puget and Juan de Fuca lobes of the Cordilleran Ice Sheet reached their maximum extents by 15,000 – 14,000 ^{14}C yr BP (Clague and James, 2002; Mosher and Hewitt, 2004). Rapid retreat of the southwestern Cordilleran ice sheet left southern Vancouver Island ice-free by 13,100 ^{14}C yr BP (Clague and James, 2002; Mosher and Hewitt, 2004). Following deglaciation, southern Vancouver Island experienced a sea-level highstand ~75 m above modern sea level no earlier than 12,360 ± 70 ^{14}C yr BP (Monahan et al., 2000, James et al., 2009). Subsequent isostatic rebound of the crust resulted in a sea-level lowstand of -30 m asl at ~11 200 cal BP (9800 ^{14}C yr BP) on southern Vancouver Island (James et al., 2009), after which local sea-level gradually rose to near its present position by ~ 6 ka (Shugar et al., 2014).

The geomorphology of my study area, along the eastern segment of the Leech River fault, was greatly influenced by the Fraser glaciation. The western portion of the study area lies within the prominent Leech River valley. While the elongation of landforms indicates dominantly southward ice flow, finer flutings imply that the Leech River valley accommodated east-southeast glacial flow subparallel to the structural grain of underlying bedrock during the latest stages of the

Fraser glaciation (Bednarski, 2016). The valley also likely hosted stagnating ice during glacial retreat (Clague and James, 2002). To the east, the lithologic Leech River fault extends beneath the Colwood Delta, a thick (≤ 30 m) package of isostatically raised glacial outwash sediments deposited during the sealevel highstand that accompanied deglaciation (Monahan et al., 2000; Clague and James, 2002; Bednarski, 2016). Kettles form several small lakes and depressions on the delta surface,and the Esquimalt Lagoon, at the eastern extent of my study area, has also been interpreted as a kettle that was occupied by stagnant ice as the Colwood Delta prograded along its margins (Howes and Nasmith, 1983; Yorath and Nasmith, 1995).

The young landscapes of recently glaciated regions present challenges for paleoseismologists because any topographic evidence of fault activity has accrued over relatively few earthquake ruptures, and is therefore smaller in scale than that observed in unglaciated regions (e.g. the San Andreas fault). In the Pacific Northwest, this problem is exacerbated by dense vegetation, which obscures subtle topographic evidence of earthquakes. However, decades of studies have successfully identified active faults in the Puget Lowland using high-resolution topographic and geophysical data (Haugerud et al., 2003; Johnson et al., 2004b). Below I outline a multi-disciplinary research strategy underpinned by high-resolution LiDAR-derived bare earth topographic data to delineate the eastern brittle Leech River fault zone through a densely vegetated area dominated by glacial and postglacial sediment cover.

3 Methods

I use LiDAR-based geomorphic mapping, shallow geophysical surveys, and structural geology field methods to elucidate the geometry, kinematics, and extent of recent faulting along the eastern Leech River fault zone. Fault strands were first delineated using LiDAR-derived topographic data, with emphasis on sites where the topographic expression of faulting appears to extend through Quaternary landforms. Subsequent fieldwork verified the presence of brittle faulting in bedrock exposures and the existence of associated scarps along strike in Quaternary sediments. Electrical resistivity and ground-penetrating radar (GPR) surveys were conducted across selected scarps to verify the presence of faulted Quaternary deposits and image fault geometry to depths of up to 20 m. Further observations of crosscutting relationships, fault characteristics, and structural measurements from slickenlined fault planes were used to constrain the relative timing, geometry, and kinematics of brittle faulting.

3.1 Bedrock and surficial mapping

I targeted my structural geomorphic mapping along the eastern 25 km of the Leech River fault zone using analysis of high-resolution LiDAR-derived topographic data (Terra Remote Sensing, 2004; James et al., 2010). Landforms and fault scarps were initially delineated using a bare-earth DEM and its derivatives including slope, aspect, hillshade and topographic profiles, as well as digital orthophotos (CRD, 2015). Subsequent fieldwork included detailed investigation of both bedrock structure and surficial deposits. I measured and described sedimentary exposures along the fault zone, and collected eight charcoal samples for radiocarbon dating and three sediment samples for luminescence dating.

Charcoal samples were collected using aluminum foil, to avoid contamination from plastic hydrocarbons, and were stored in the refrigerator until shipped to avoid mold growth. Samples were prepared for analysis, including removal of modern rootlets and shaving the surfaces of fragments, by PALEOTEC SERVICES, and analysed by the Keck Carbon Cycle AMS facility, at the University of California, Irvine. The radiocarbon ages reported here were corrected for modern wood levels by the laboratory. I used Oxford Radiocarbon Accelerator Unit (ORAU)'s OxCal

radiocarbon calibration program to calibrate the corrected radiocarbon ages and provide the age ranges in cal yr BP.

Sand samples were collected for luminescence dating by inserting a steel pipe, ~6 cm in diameter, into the exposure to collect sand that has not been exposed to light since its deposition. The USGS Luminescence Geochronology Lab performed multi-grain optically stimulated luminescence (OSL) analysis on quartz and infrared stimulated luminescence (IRSL) on feldspar grains using single aliquot analyses. Luminescence dating methods rely on the assumption that grains were completely bleached during their depositional episode, which can lead to unreliable results in glaciofluvial deposits, where this assumption is rarely valid.

Exposures of brittle fault zones in bedrock were located in the field and the topographic expression of each brittle fault strand was traced along strike on LiDAR imagery to identify sites where scarps cut Quaternary deposits. I visited these scarps to assess the likelihood that they were of tectonic origin, and sites where scarps could not easily be explained by glacial, colluvial, or anthropogenic processes were selected for electrical resistivity and GPR surveys.

3.2 Kinematic and geometric analysis

To elucidate the geometry and kinematics of brittle faulting along the eastern Leech River fault zone, I used analysis of slip-sense indicators on slickenlined fault planes (Petit, 1987; Doblas, 1998; Marshall et al., 2000; Sperner and Zweigel, 2010). I measured slickenlines and inferred the slip-sense of 244 fault planes (Appendix A) using indicators such as plough marks, euhedral crystal growth, crystallization in lee of asperities, and the relative orientation of secondary fractures (Petit, 1987; Doblas, 1998). Field observations of the mineralogy and clay content of faults and crosscutting relationships of both fault planes and sets of slickenlines were used to constrain the relative timing of slip and distinguish between multiple generations of fault activity. I focused my analysis on the geometry and kinematics of the most recent generation of activity that could be identified at each site.

Slickenline and slip-sense data were inverted for strain using open-source FaultKin 7 software (Allmendinger et al., 1989; Marrett and Allmendinger, 1990). I plotted the kinematic P

and T axes and best-fit fault plane solutions for multiple slip-sense indicator measurements from each fault zone on lower-hemisphere projection stereonets. Sets of fault plane measurements from each field site were defined on the basis of fault orientation, kinematics, mineralogy, and field relationships. At many sites, kinematic axes formed multiple clusters, which is an indication that the kinematics of a fault may have varied over the span of its activity (Allmendinger et al., 1989; Marshall et al., 2000). Where possible, fault mineralogy and crosscutting relationships were used to distinguish between multiple generations of faulting, and constrain their relative ages. The geometry of mesoscale fault strands was interpreted using Riedel shear framework, which is typical of strike-slip faults (Fig. 2; Cloos, 1928; Riedel, 1929; Swanson, 2006). Topography and geophysical surveys were used to further identify fault strands that offset Quaternary units.

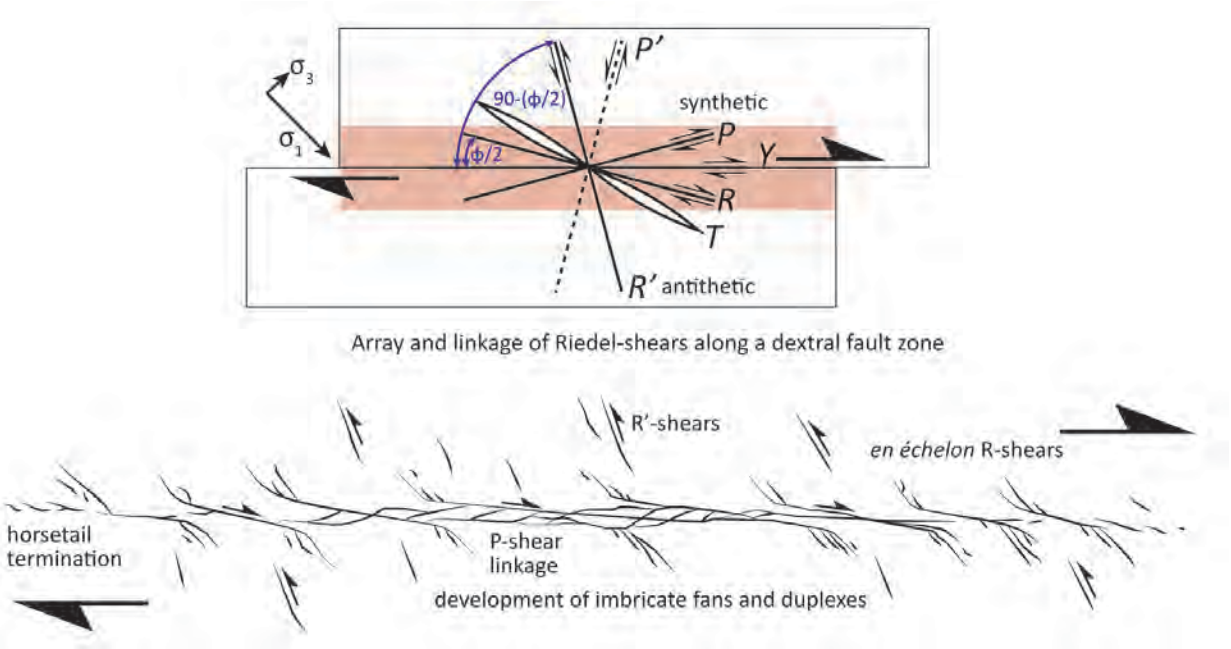

Figure 3. Riedel Shear schematic and common linkage patterns for a dextral strike-slip fault. Modified from Swanson (2006).

3.3 Electrical resistivity tomography (ERT)

In order to confirm the presence of Quaternary faulting and image fault geometry to depth, I collected 19 ground-based electrical resistivity surveys in transects across fault scarps. Electrical resistivity, the inverse of conductivity, indicates a material's resistance to electrical

current flow, and is influenced by the mineralogy, fluid content, porosity, and clay content of geologic materials (Reynolds, 2011). Resistivity is commonly measured by injecting a current (I) into the ground through two source electrodes and measuring the resultant difference in voltage (ΔV) between two receiver electrodes (Fig. 3; Burger et al., 2006).

$$\rho_a = K\frac{\Delta V}{I} \quad \text{(Eq. 1)}$$

, where ρ_a is the measured apparent resistivity (in Ohm-m), I is the injected current (in Amperes), ΔV is the measured potential difference, and K is the geometric factor, which depends on the array configuration (Advanced Geosciences Inc., 2007) . For a dipole-dipole array, Eq. 1 becomes:

$$\rho_a = \pi n(n+1)(n+2)a\frac{\Delta V}{I} \quad \text{(Eq. 2)}$$

, where a is the electrode spacing (in m), and n is the multiple of a between source and receiver electrode pairs (Fig. 3).

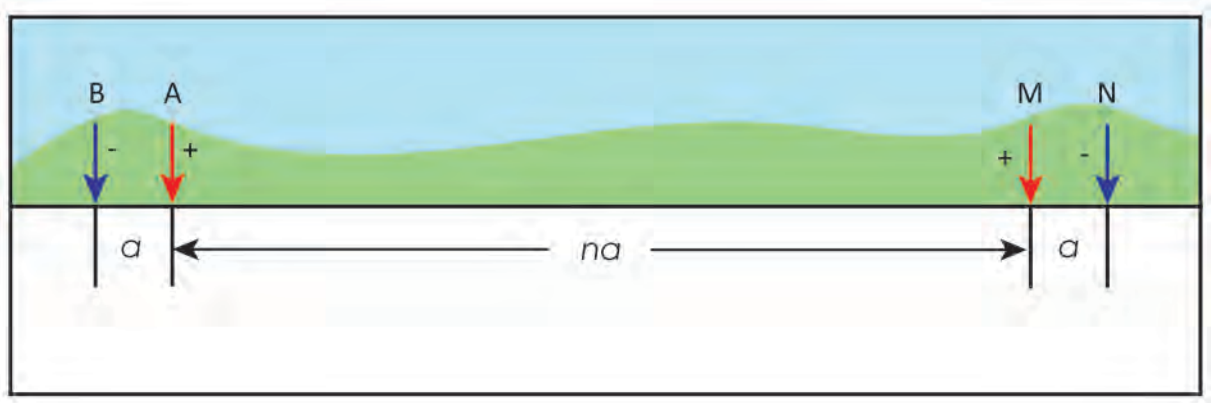

Figure 4. Dipole-dipole electrode configuration, where A and B are transmitting electrodes, and the resulting electric potential is measured between M and N. Adapted from Advanced Geosciences Inc. (2007).

Systematically varying the distance between source and receiver electrodes along an array allows for collection of apparent resistivity measurements along many different paths, which can be inverted to produce an electrical resistivity tomography (ERT) profile (Authemayou et al., 2012). Several studies have used ERT to successfully characterize the geometry of shallow faulting

based on contrasting resistivity values across faults caused by associated changes in mineralogy, pore water distribution, and groundwater flow (Suski et al., 2010; Authemayou et al., 2012; Carbonel et al., 2013).

Resistivity measurements were made with an AGI MiniSting R1/IP, DC-Memory Earth Resistivity Meter and a 28-electrode dipole-dipole array. Electrodes were inserted into the ground at uniform spacing along a linear transect centred on the feature of interest. Most surveys were done with 3 m electrode spacing, which results in an ~81-m-long profile extending to a depth of ~15 m. At sites where higher-resolution shallow imagery was desired, electrode spacing of between 0.5 – 1.5 m was used. Before collecting apparent resistivity measurements, the contact resistance was measured along the array and I applied saline solution at the base of electrodes to support current flow. Apparent resistivity measurements and topographic data were inverted to produce ERT profiles using EarthImager 2D software (Advanced Geosciences Inc., 2011).

3.4 Ground-penetrating radar (GPR)

In order to image faulting to depth and confidently locate the bedrock basement, I colocated a series of ground-penetrating radar (GPR) surveys with my resistivity tomography. GPR emits and measures the return of pulses of electromagnetic (EM) signals to image reflectors in the subsurface, in a manner similar to seismic reflection surveying (Reynolds, 2011). A transmitting antenna (T_x) sends pulses of radiowaves into the ground over a particular bandwidth with the peak power at the centre frequency (f_c) of the selected antenna. The radiowaves propagate in broad beam downward at velocities dependent on the dielectric constant (Ɛ) of the material, which, similarly to electrical resistivity, is highly dependent on water and clay content. As the waves interact with features of the subsurface, they are reflected upward and received by a second antenna (R_x), which scans for reflected waves at a high frequency (e.g. 512 or 1024 scans/sec). The instrument records the two-way travel time of received signals and displays them in a radargram, which can be read as a cross-sectional view of the subsurface.

Ground-penetrating radar (GPR) surveys were conducted using a GSSI SIR 3003 with 100 MHz, 200 MHz, and 400 MHz antennae. A survey wheel measured the distance along the survey

line, and the instrument range was manually adjusted to optimize resolution and depth for each survey. Gain was applied to the data as it was collected at three or five evenly spaced depths, and was optimized later in processing. The software package GPR-SLICE V7.0 was used to display, filter, and migrate radargrams. A static topographic correction, which simply shifts the scan columns in the radargram up and down, was applied using topography profiles extracted from the LiDAR DEM. Dispersion of waves around cobbles in the subsurface results in hyperbolae in radargrams, which were used to calculate the radiowave velocity of the material, and convert time (ns) to depth (m). I interpreted processed radargrams together with ERT, topography, and field observations to identify brittle fault strands and locate the bedrock basement. Previously published GPR imagery of shallow faulting (e.g. McClymont et al., 2010; Carpentier et al., 2012; Ercoli et al., 2013) exhibits characteristics such as truncated and offset reflectors and sharp contrasts in reflective domains. Topographic scarps, ERT and GPR, and crosscutting relationships of slickenlined fault planes were used in concert to map the geometry and infer the kinematics of Quaternary or otherwise recent faulting along the eastern Leech River fault zone.

4 Results

My mapping of the eastern Leech River fault zone reveals a complex zone of *en échelon* and conjugate brittle fault strands up to 1 km wide and 25 km long. This fault zone is oriented parallel to, but does not coincide with, the fault bounding the Metchosin Formation and Leech River Complex, the lithologic Leech River fault. Fault strands are typically steeply dipping to subvertical, and are identified on the basis of topographic scarps and lineaments, bedrock observations, and geophysical profiles. Faults are classified either as observed, inferred (in cases where topography or geophysical imagery suggests that they continue along strike from observed faults), or covered (in cases where they are covered by later deposits, which they do not displace, along strike from observed faults). Similarly, Quaternary activity is indicated as observed where there is direct observation of offset Quaternary deposits, and as inferred where evidence of offset sediments is provided by topography, geophysical profiles, or ambiguous sedimentary evidence. The following section presents analysis of the geometry and kinematics of brittle faulting at five main field sites (Sites 1-5 Figs. 4B, 4C), which together lead to my interpretation of the Leech River fault zone as an active dextral flower structure.

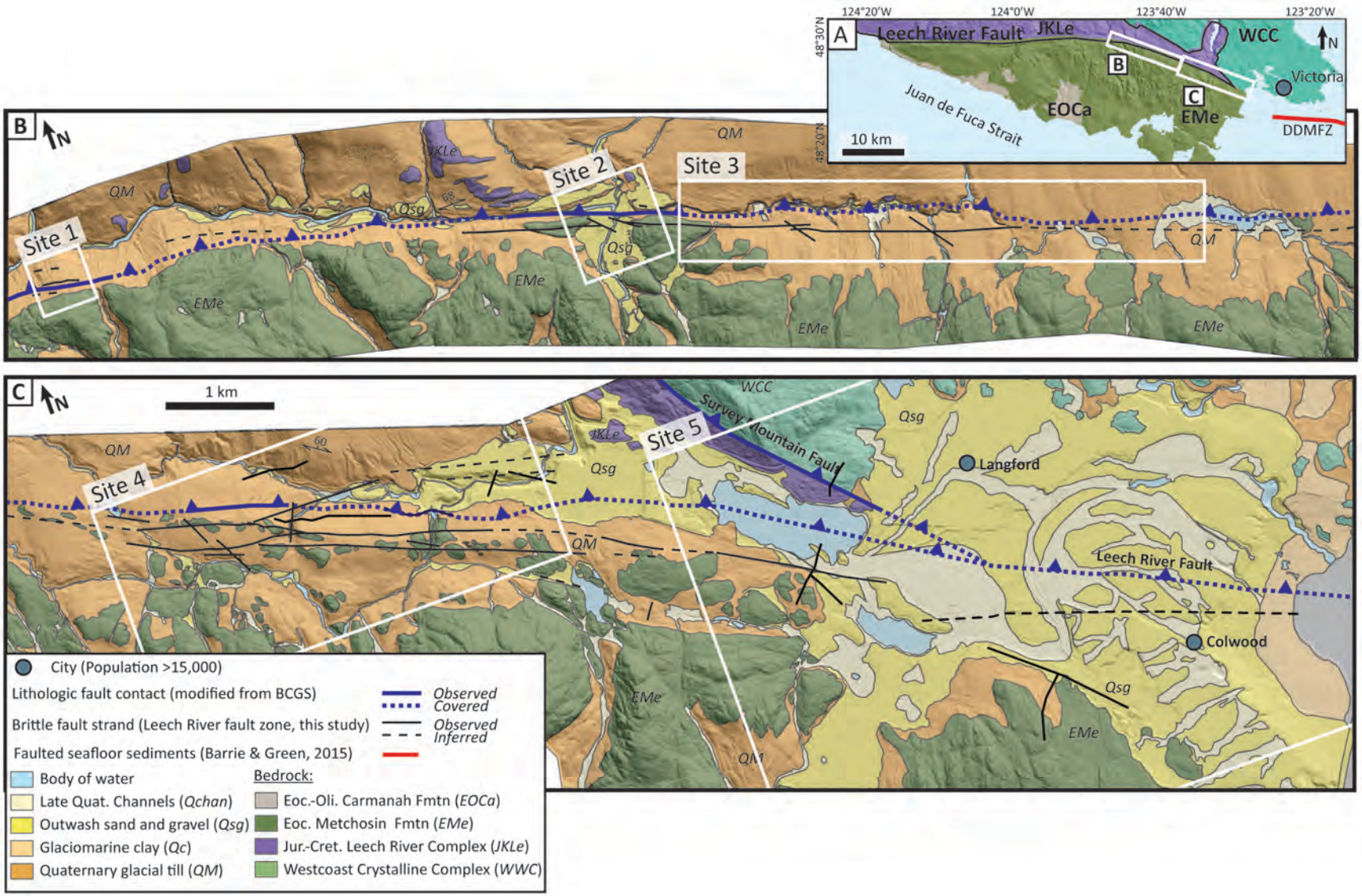
A
124°20'W
124°0'W
123°40'W
123°20'W
48°30'N
48°20'N
Leech River Fault
JKLe
WCC
N
B
C
Victoria
Juan de Fuca Strait
EOCa
EMe
DDMFZ
10 km
B
N
Site 1
Site 2
Site 3
QM
Qsg
JKLe
EMe
C
1 km
Site 4
Site 5
Survey Mountain Fault
Langford
Colwood
Leech River Fault
City (Population >15,000)
Lithologic fault contact (modified from BCGS)
Observed
Covered
Brittle fault strand (Leech River fault zone, this study)
Observed
Inferred
Faulted seafloor sediments (Barrie & Green, 2015)
Body of water
Late Quat. Channels (Qchan)
Outwash sand and gravel (Qsg)
Glaciomarine clay (Qc)
Quaternary glacial till (QM)
Bedrock:
Eoc.-Oli. Carmanah Fmtn (EOCa)
Eoc. Metchosin Fmtn (EMe)
Jur.-Cret. Leech River Complex (JKLe)
Westcoast Crystalline Complex (WWC)

Figure 5. (A) Geologic setting of the study area on southern Vancouver Island. Modified from Massey et al. (2005) with the Leech River fault simplified to a single, lithologic fault contact. DDMFZ: Fault zone imaged by seafloor reflection profiling of Barrie & Greene (2015), interpreted as an extension of the Darrington-Devil's Mountain fault zone. Areas of panels B and C in white rectangles. (B-C) Generalized structural geomorphic map of the eastern Leech River fault zone overlain on LiDAR-derived hillshade image (James et al., 2010). Surficial units are delineated from LiDAR imagery, and modified from Monahan et al. (2000) in the Colwood Delta region to the east. Brittle fault strands (black lines) are observed in bedrock and extended along strike in topography (inferred) on either side of the lithologic Leech River fault, which is modified from Massey et al. (2005) with additional detail in areas of exposure. Detailed field areas, shown in Figs. 5A, 6, 10A, 11A, and 12A, are outlined in white and numbered 1-5.

4.1 Site 1

At the west end of the study area, LiDAR data reveal a >200-m-long uphill-facing scarp cutting a smooth north-facing slope 150 m north of the steep Metchosin Formation cliffs that form the southern boundary of the Leech River valley (Fig. 5A,B). The slope at Site 1 consists of glacial till, presumably of the Fraser glaciation, overlain by a thin (<5 m) colluvial apron incised by a series of debris flow channels. Topographic profiles across the scarp (**F1-1**, Fig. 5B) consistently indicate several metres of north-side-up vertical separation, averaging 3.9 ± 0.9 m along the debris flow channels and 5.7 ± 1.3 m along the associated interfluves (Morell et al., 2017). The systematically greater offset along interfluves than channels has been used to infer that at least two late Quaternary fault ruptures have occurred along a near-vertical fault underlying this scarp (Morell et al., 2017). Paleoseismic trenching in the summer of 2016 confirmed north-side-up displacement of both schist of the Leech River Complex and post-Fraser, late Quaternary units along subvertical to steeply south-dipping fault planes. Several subtle topographic scarps and associated contrasts in geophysical profiles collected ~50 m west of the paleoseismic trenches suggest that **F1-1** is one of several strands that make up a complex fault zone up to 200 m wide cutting late Quaternary till, colluvium, and bedrock straddling the lithologic Leech River fault.

I conducted three electrical resistivity profiles of varying resolution along an interfluve (Fig. 5E) and one relatively high-resolution profile within a channel (Fig. 5D) across the topographic scarp at **F1-1**. The relatively shallow resistivity profiles across **F1-1**, which image to ~5 m depth

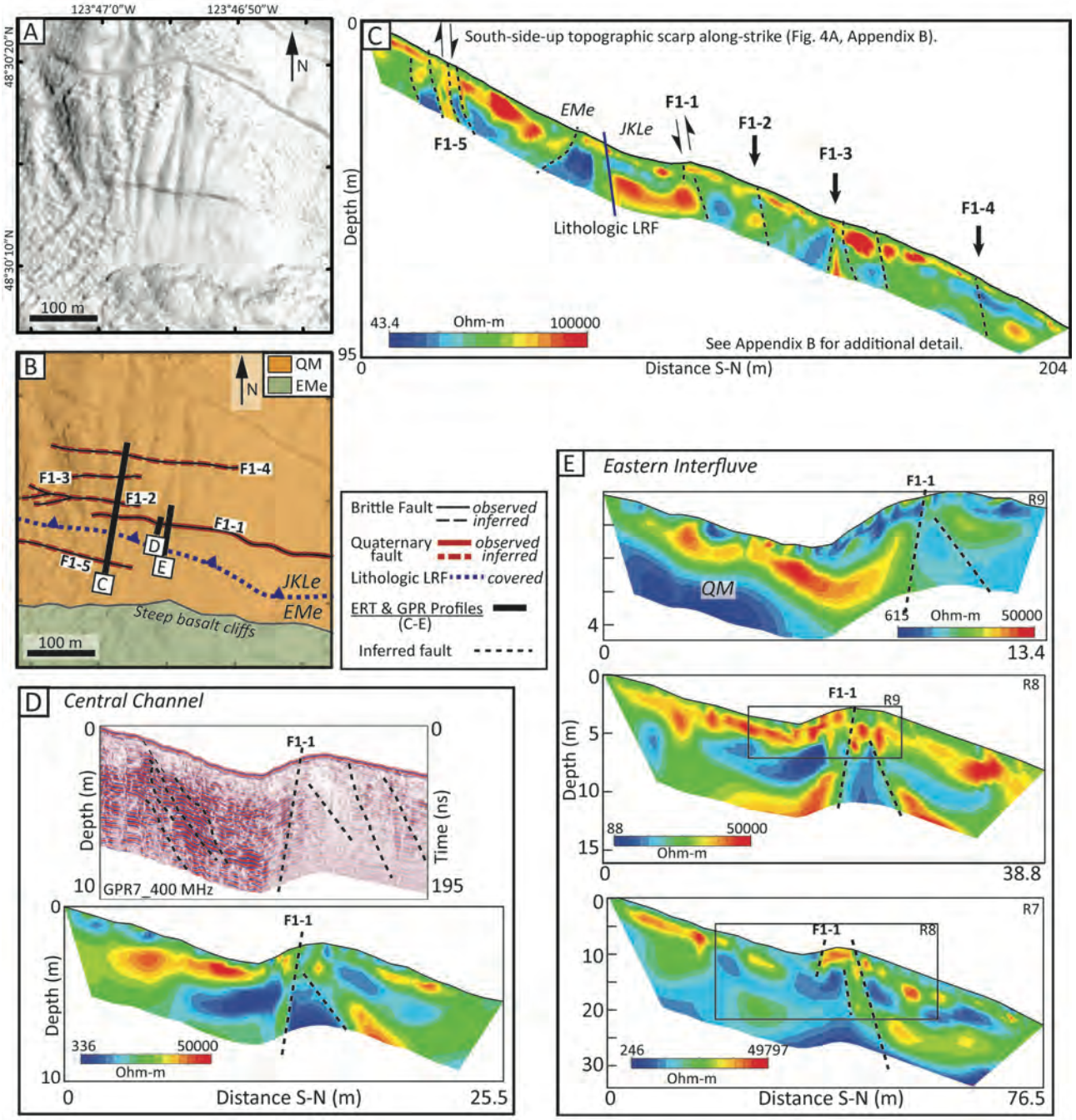

Figure 6.(A) LiDAR-derived hillshade image of Site 1 (James et al., 2010). (B) Surficial materials, lithologic contact, fault scarps, and geophysical survey lines overlain on hillshade image. (C) ERT along the western interfluve (Line C) from Fig. 5B, showing the lithologic contact and other inferred faults corresponding to those shown on Fig. 5B. (D) GPR and ERT of Line D, within a debris flow channel adjacent to a paleoseismic trench. Dashed lines indicate observed faults. (E) ERT from Line E, along an interfluve adjacent to a paleoseismic trench.

within the channel (Fig. 5D) and ~3 m depth along the interfluve (Fig. 5E,R9) reveal an ~2 – 3-m-wide moderately resistive zone dipping steeply to the south near the surface, consistent with the geometry of faulting observed in paleoseismic trenches. At a depth of a few metres, a second linear zone with a well-defined resistivity contrast dips more moderately (~55°) to the north, appearing to converge with the steeply south-dipping strand within ~2 m of the surface. Colocated GPR profiles (Fig. 5D, Appendix B) reveal a contrast in reflector strength across the steeply south-dipping fault, with the upthrown northern block lacking the strong reflectors imaged south of the fault. The deeper, north-dipping resistive anomaly is also visible in GPR imagery as a subtle contrast in reflector strength, and fine seams appear to truncate reflectors over a distributed zone (Appendix B).

Deeper (~8 m) resistivity tomography from the eastern interfluve (Fig. 5E, R8) more clearly illustrates the convergence of two steeply dipping opposing faults beneath the topographic scarp of **F1-1**. However, a lower resolution profile reaching to ~17 m depth (Fig. 5E, R7) images **F1-1** as a steeply north-dipping contrast separating relatively conductive material to the south from more resistive material to the north. This disparity may indicate that the dominant structure dips to the north at depth, or may be due to north-flowing groundwater pooling against the fault.

The topographic expression of **F1-1** becomes less prominent along strike, and geophysical imagery along an interfluve ~50 m to the west reveals a complex zone up to 200 m wide of subvertical and steeply north-dipping zones exhibiting sharp resistivity contrasts (Fig. 5C; Appendix B). A sharp subvertical resistivity contrast ~40 m to the south of **F1-1** is constrained by subcrop and float on the hillslope to coincide with the lithologic Leech River fault. Subvertical to steeply dipping resisitivity contrasts are imaged both north (**F1-2** – **F1-4**) and south (**F1-5**) of the lithologic fault, corresponding to subtle sub-metre to 5-m-high scarps identified from LiDAR imagery (Fig. 5B; Appendix B). The sense of offset is not readily apparent on the more subtle scarps to the north (**F1-2** – **F1-4**), and it is possible that the sharp linear contrasts in the northern portion of the profile are associated with compositional variations in the schist of the Leech River Complex, whose structural grain dips steeply to the north-northeast in this area (C. Regalla, personal communication, 2016). Significant south-side-up topography along strike of **F1-5**

(Appendix B) suggests that is the product of either north-side-down displacement, strike-slip displacement of raised topography, or, alternatively, colluvial processes at the southern margin of the Leech River valley.

Offset debris-flow channels across **F1-1** indicate almost pure north-side-up dip-slip motion of Quaternary deposits. Although strike-slip offset is not indicated by topography anywhere within Site 1, the overall steep geometry of the fault zone, intersecting fault planes imaged beneath **F1-1**, and the ~200 m wide zone of steeply north-dipping and subvertical resistivity contrasts beneath topographic slope breaks imply that the fault zone is a steeply dipping flower structure cutting Quaternary units and bedrock on both sides of the lithologic Leech River fault as identified from ERT and field observations.

4.2 Site 2

At Site 2, ~7 km along strike to the east from Site 1, basalt of the Metchosin Formation exhibits extensive brittle faulting exposed by a quarry (Site 2-A) and road cut (Site 2-B) within 30 – 100 m of ductilely deformed Leech River Complex (Fig. 6). The area is covered by flights of glaciofluvial and fluvial terraces that flank the banks of the Sooke and Leech Rivers near their confluence, providing an opportunity to investigate interactions between fault activity and Holocene sedimentation. I begin by discussing fluvial sedimentation and follow with a description of the exposed fault zones and potential tectonic disturbance of postglacial units. I use prominent bedrock scarps to define the strike of the fault zone in this area as ~294°, which is used as the Y axis to interpret fault geometry within a Riedel shear framework (Fig. 2; Swanson, 2006).

4.2.1 Glaciofluvial and fluvial terraces

The area surrounding the confluence of the Leech River, Old Wolf Creek, and the Sooke River has several sets of glaciofluvial and fluvial terraces formed predominantly through eastward flow down the Leech River valley and southward flow on the Sooke River following the Fraser glaciation (Fig. 6). I use LiDAR imagery to delineate six sets of terraces formed by southward flow on the Sooke River, ranging from 2 – 15 m above the modern stream. Terrace levels along the banks of the Leech River are generally higher, with four sets ranging from 9 – 19 m above modern

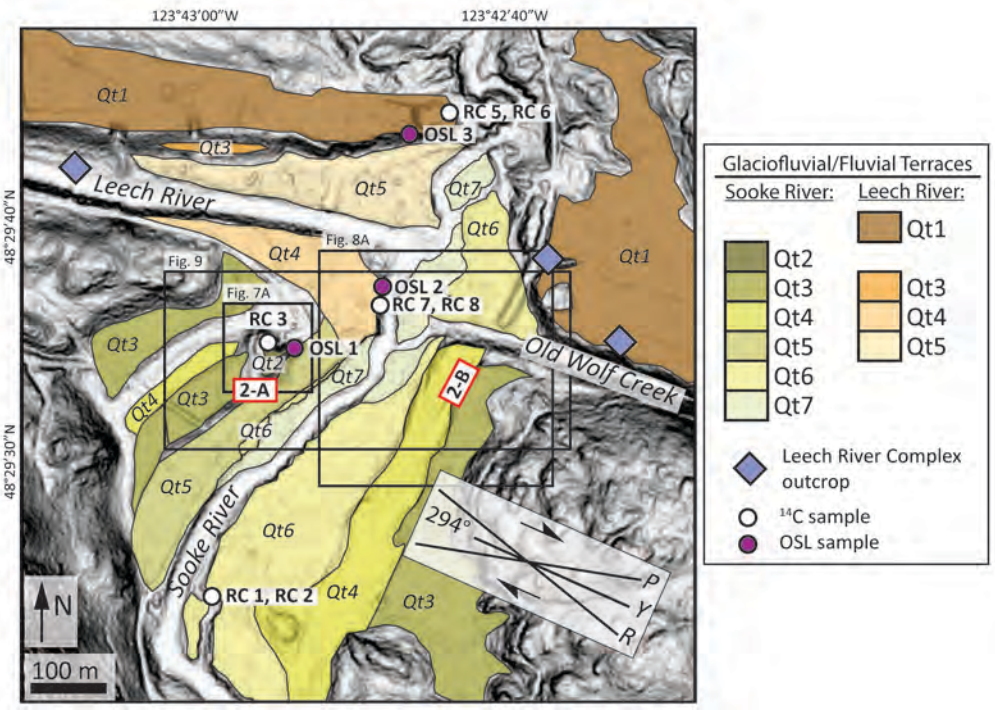

Figure 7. Site 2 area with sets of glaciofluvial and fluvial terraces surrounding the confluence of the Leech River, Sooke River, and Old Wolf Creek overlain on a DEM-derived slope image. Radiocarbon (RC) and luminescence (OSL) samples provide constraint on sedimentation dates. Outcrops of Leech River Complex along the Leech River and Old Wolf Creek imply that the lithologic Leech River fault lies within 30 – 200 m of the brittle fault zones observed in Metchosin Formation at Sites 2-A and 2-B (red boxes). Riedel shear framework is used to define the Y axis along main bedrock scarps, at a strike of ~294°. Areas of Figs. 7A, 8A, and 9 are outlined in black boxes.

stream levels. Together, the fill terraces are classified into seven sets, which are assumed to young downwards towards the modern stream, consistent with the limited chronology presented here (Tables 1, 2).

The surface of the highest terrace, *Qt1*, slopes gently to the east along the northern banks of the Leech River and Old Wolf Creek (Fig. 6). The deposits consist of thick (>10 m) gravel and sand layers exposed by quarries both west and east of the Sooke River. Small (sub-centimetre) fragments of charcoal collected from an ~4-cm-thick light grey ash layer beneath ~1.5 m of oxidized loamy sand, cobbles, and organics at the top of *Qt1,* north of the Leech River, returned radiocarbon ages of 305 ± 15 and 135 ± 15 BP (**RC 5**,**6**, Table 1, Appendix C). The elevation of *Qt1*,

Table 1 **Radiocarbon dates from charcoal in terrace deposits at Site 2, and woody material at Site 5.**

Sample	UCIAMS #	Site	Unit	Location		^{14}C age	Calibrated age	Comment
				Latitude (°N)	Longitude (°W)	(BP)[a]	(cal yr BP)[b]	
RC 1	189523	2	Sooke east Qt6	48.490	123.716	465 ± 15	501 - 527	Cm-scale charcoal fragment from within sand lens in silty-sandy inset channel, ~.7 m from surface, few modern rootlets
RC 2	189524	2	Sooke east Qt6	48.490	123.716	2110 ± 15	2008 - 2141	Sub-cm charcoal fragments within well-sorted dark orange-brown medium-grained sand below RC 1, ~0.9 m from surface
RC 3	189525	2-A	Sooke west Qt2	48.493	123.715	1955 ± 20	1832 - 1968	Mm-scale charcoal fragments from dark orange silty material above FZ3 below ~60 cm of poorly sorted colluvium
RC 4	189526	5-C	Colwood Delta bottomsets	48.427	123.476	12265 ± 30	14038 - 14324	Cm-scale water-logged woody material in lee of conglomerate intraclast in grey-blue cly/slt unit, ~2.5 m below surface
RC 5	170461	2	Leech north Qt1	48.496	123.712	305 ± 15	305 - 431	3 small flat charcoal fragments collected from light grey ash/coal layer 4 cm thick 1.3 m below surface
RC 6	170462	2	Leech north Qt1	48.496	123.712	135 ± 15	11 - 272	Charcoal (one piece broken into 2 fragments) from 1.3 m below surface, light grey ash/coal layer 4 cm thick
RC 7	170463	2	Leech south Qt4	48.493	123.713	6430 ± 20	7313 - 7423	Sub-cm charcoal fragments from within schistose sand matrix of pebble-cobble gravel, ~1 m below surface, below RC 8
RC 8	170464	2	Leech south Qt4	48.493	123.713	1560 ± 20	1401 - 1525	Sub-cm charcoal fragments from oxidized silty loam layer in 2x10m exposure west of Sooke River, ~0.5 m below surface, above RC 7

[a]Sample preparation backgrounds have been subtracted, based on measurements of ^{14}C-free wood.
All results have been corrected for isotopic fractionation according to the conventions of Stuiver and Polach (1977), with $d^{13}C$ values measured on prepared graphite using the AMS spectrometer. These can differ from $d^{13}C$ of the original material, if fractionation ocurred during sample graphitization or the AMS measurement, and are not shown.
[b]Range of calendar calibrated ^{14}C ages within 2σ of the mean.

~19 m above the modern Leech River, suggests a much older origin, and the dates are likely representative of a fire in the catchment area rather than the sediment deposition responsible for terrace formation. A luminescence sample (**OSL 3**, Table 2) from a sand lens within a nearby gravel exposure, also from *Qt1*, returned discordant quartz and feldspar dates of 4330 ± 2580, and 22,800 ± 3080 yrs BP respectively. The discordance of OSL and IRSL ages, and scatter of > 30% on samples **OSL 2** and **3** indicate that the grains were poorly bleached during deposition, making the calculated ages unreliable (Table 2). The age of *Qt1* is thereby constrained only by inferring that it is older than *Qt2,* which lies ~4 m below *Qt1* at a height of ~15 m above the Sooke River. A sample of oxidized silt deposited above a fault zone at Site 2-A, returned an OSL age of 11,700 ± 1,510 yr BP (**OSL 1**, Table 2). The relatively low scatter value (9%) of **OSL 1** suggests that the quartz grains were sufficiently bleached during deposition, and that the calculated age is reliable (Table 1).

Terrace set *Qt3*, ~11 m above modern stream levels, consists of a small inset terrace north of the Leech River, two more extensive surfaces on the outer flanks of the Sooke River valley, and sediments in lee of the bedrock knob of Site 2-A. The only exposure of *Qt3* sediments consists of partially vegetated poorly sorted cobbly gravel sloughing down the slope above a fault zone (**F2-6)** at Site 2-B (Fig. 8C), and no material was available for dating. A charcoal sample from *Qt4*, which lies ~9 m above the modern stream south of the Leech River, returned an age of 7313 – 7423 cal yr BP, (**RC 7**, Table 1), but may have a younger bias due to contamination from modern rootlets, since it was collected from within ~1 m of the modern surface (Appendix C). A second charcoal sample ~50 cm above **RC 7** in the same stratigraphic section returned an age of 1401 – 1525 cal yr BP (**RC 8**, Table 1, Appendix C), likely representing a pre-historic fire during Holocene soil development. *Qt4* surfaces are also present along the banks of the Sooke River, inwards to the valley from *Qt3*, but the deposits are not exposed. *Qt5* terrace surfaces also lack exposure, but occur north of the Leech River and west of the Sooke River, ~7 m above modern stream levels.

Terrace surfaces ~4 m above modern stream levels are classified as *Qt6*, and occur as narrow inset terraces on the west bank of the Sooke River, and more extensively to the east. Two charcoal samples from the side of a channel inset in the southern portion of eastern Sooke *Qt6* returned ages of 2008 – 2141 and 501 – 527 cal yr BP. (**RC 1**, **2**, Table 1, Appendix C). The older sample, **RC 2**, consists of sub-centimetre charcoal fragments ~.9 m below the surface within a well-sorted medium-grained dark orange-brown sand layer. The younger sample, **RC 1**, consists of

Table 2. Optically Stimulated Luminescence (OSL) ages from quartz and Infrared Stimulated Luminescence (IRSL) ages from feldspar grains in terrace deposits at Site 2.

Sample	Site	Unit	% Water content[a]	K (%)[b]	U (ppm)[b]	Th (ppm)[b]	Total Dose (Gy/ka)[c]	Equivalent Dose (Gy)	n[d]	Scatter[e]	Age (yrs)[f]
OSL 1	2-A	*Qt2* Sooke	4 (39)	1.08 ± 0.08	1.30 ± 0.23	5.61 ± 0.36	1.65± 0.08	19.3± 2.3	14(24)	9%	11,700 ± 1,510
							2.34 ± 0.11[g]	39.2 ± 4.1[g]	2 (10)	34%	16,780 ± 1,940[g]
OSL 2	2	*Qt 4* Leech	2 (26)	0.97 ± 0.04	1.05 ± 0.26	2.56 ± 0.16	1.37± 0.07	29.3± 3.5	7 (10)	36%	21,390 ± 2,810
							1.85 ± 0.10[g]	46.2 ± 4.7[g]	3 (10)	52%	24,860 ± 2,890[g]
OSL 3	2	*Qt1* Leech	21 (31)	1.01 ± 0.07	0.79 ± 0.24	3.35 ± 0.49	1.36 ± 0.12	5.9 ± 3.5	1 (8)	156%	4,330 ±2,580
							1.82 ± 0.16[g]	41.5 ± 4.2[g]	2 (10)	47%	22,800 ± 3,080[g]

[a]Field moisture, with figures in parentheses indicating the complete sample saturation %. Dose rates calculated using 55% of the saturated moisture (i.e. 16 (58) = 58 * 0.55 = 32).
[b]Analyses obtained using high-resolution gamma spectrometry (high purity Ge detector).
[c]Includes cosmic doses and attenuation with depth calculated using the methods of Prescott and Hutton (1994). Cosmic doses were between 0.15-0.20 Gy/ka.
[d]Number of replicated equivalent dose (DE) estimates used to calculate the equivalent dose. Figures in parentheses indicate total number of measurements included in calculating
the represented DE and age using the minimum age model (MAM); analyzed via single aliquot regeneration on quartz or K-feldspar grains.
[e]Defined as "over-dispersion" of the DE values. Values >30% are considered to be poorly bleached or mixed sediments.
[f]Dose rate and age for fine-grained 250-90 micron sized quartz. Exponential + linear fit used on DE, errors to one sigma.
[g]Dose rate and age for fine-grained 250-90 microns K-feldspar, post IR230C; no fade. Exponential + linear fit used on DE, errors to one sigma.

a single cm-scale charcoal fragment ~0.7 m from the ground surface within coarse-grained schistose sand. The lowest terrace level, *Qt7*, lies only ~2 m above the modern level of the Sooke River, and consists of vegetated gravel bars likely still geomorphically active.

4.2.2 Site 2-A

A quarry west of the Sooke River, at Site 2-A, exposes three 2 – 3-m-wide gouge-bearing fault zones overlain by wedge-shaped gravel deposits (FZ1 – 3, Fig. 7A). The fault zones consist of heavily fractured and moderately clay-altered basalt with numerous *en échelon* and conjugate fault planes of varying mineralogy, from thin (≤ 1 cm) quartz - epidote ± chlorite ± zeolite coating to centimetre-scale iron-oxide clay gouge-bearing seams. Slip-sense indicator measurements from slickenlines (n=45) are divisible into four kinematically consistent fault orientations (**F2-1 – F2-4**), that occur in six main strands. The geometry of the fault strands is consistent with an extensional step-over between two R shears of a right-lateral strike-slip fault zone (Figs. 7A, 7B).

Two subparallel fault strands (**F2-2**) are traced along strike between 1) fault zone 1 and a slickenlined block in the centre of the quarry, and 2) fault zones 2 and 3 (Fig. 7A). Slip-sense indicators from **F2-2** (n=17) consist of sparse (n=3) subvertical planes with shallowly plunging slickenlines indicating right-lateral motion and abundant *en échelon* northeast-dipping concave

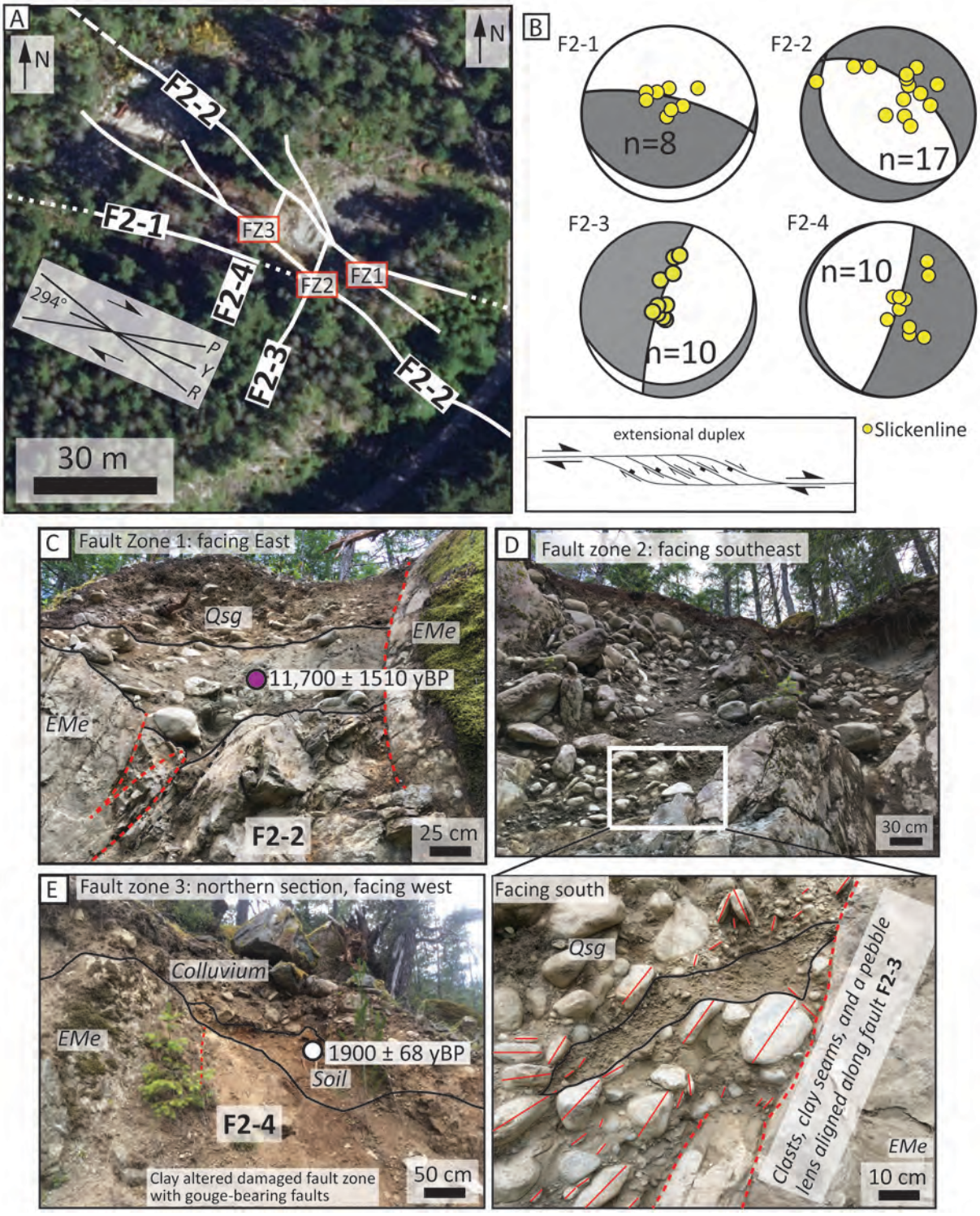

Figure 8. (A) Slope image of Site 2-A with locations of fault zones (FZ1 – 3) and map of fault strands (white lines: solid – observed; long dash – inferred; short dash – covered) within Riedel shear framework. (B) Fault plane solutions from strain inversion of kinematically consistent slip-sense

indicators. (C) Fault zone 1 and overlying sediment wedge against buttress unconformity, with OSL age. (D) Fault zone 2 and overlying glaciofluvial deposit with inset showing aligned sedimentary features. (E) Northern portion of Fault zone 3 beneath a charcoal-bearing (with radiocarbon sample) oxidized loamy sand buried by a wedge of colluvium. Dashed red lines indicate select slickenlined or gouge-bearing fault planes. Facing directions indicate the direction the photographer is facing.

planes with dip-slip normal motion (Figs. 7B, 7C). The subvertical strike-slip fault planes form the southern boundaries to fault zones 1 and 3, while the concave normal faults splay towards the northeast beneath coincident 1 – 4 m north-side-down steps in bedrock topography. Based on these observations, I interpret the kinematically consistent fault strands comprising subvertical strike-slip and *en échelon* normal faults (**F2-2**) as localized negative flower structures, exposed for ~15 m along strike. A best-fit fault plane solution from strain inversion reveals a moderately northeast-dipping (~309°/50° N) extensional fault with a minor component of right-lateral motion (Fig. 7B). Both the kinematic strain inversion of **F2-2** and its orientation ~14° clockwise relative to the Y axis (~294°) suggest that the two exposed strands of **F2-2** are R shears within a right-lateral strike-slip system.

Exposures of the southern strand of **F2-2**, in fault zones 2 and 3, comprise intersections of **F2-2** with high-angle conjugate faults of similar character (**F2-3, F2-4**) (Figs. 7B, 7D, 7E). The high-angle conjugate faults (**F2-3, F2-4**) are interpreted as R' shears forming an extensional step-over between the two strands of **F2-2** (Fig. 7A). Slip-sense indicator measurements from **F2-4** (n=10), on the west side of the quarry, consist of normal dip-slip and left-lateral oblique slip on steeply east-northeast-dipping planes, and strain inversion of kinematic axes produces a best-fit fault plane solution of a subvertical east-side-down normal fault (010°/80° E) (Fig. 7B). Kinematic axes of slip-sense indicator measurements (n=10) from **F2-3**, on the east side of the quarry, produce a best-fit fault plane solution of a subvertical extensional fault similar to that of **F2-4**, but dipping steeply to the west (~80°) and with a minor component of right-lateral motion (Fig. 7B).

Fault strand **F2-3** is observed crosscutting a quartz ± epidote ± chlorite slickenlined fault plane exposed along the south wall of the quarry, which is one of two subparallel strands of similar mineralogy (**F2-1,** Fig. 7A). Slickenline measurements (n=8) from these two fault strands

define a steeply north-northeast-dipping (291°/75°N) reverse fault with a minor right-lateral component (Fig. 7B). A lack of clay alteration and gouge implies that **F2-1** represents a relatively high temperature regime, and the truncation of the southern strand of **F2-1** by the thicker, gouge-bearing fault in the eastern wall (**F2-3**), indicates that **F2-1** predates the other exposed faults. The geometry and kinematics of the most recent faulting at this site (**F2-2 – 4**) are consistent with a dextral strike-slip system, with R shears oriented ~14° clockwise relative to the Y axis, two R' shears forming an extensional duplex between right-stepping R shears, and minor right-lateral components of fault plane solutions (Figs. 7A, 7B).

As mentioned above, fault zones 1 – 3 are overlain by wedge-shaped deposits, 2 – 8 m wide and up to 5 m thick, of various postglacial sediments. The sediments overlie smoothed bedrock surfaces with centimetre- to decimetre-scale relief across gouge-bearing fault seams locally (e.g. Fig. 7C). It is not clear whether the surface is offset by these fault seams, or whether the irregular unconformity is the result of differential weathering. The deposits abut moderately dipping to subvertical, often slickenlined planes, and taper towards the north above zones of imbricate north-dipping normal faults (**F2-2-4**). Several geomorphic and sedimentary features of the wedges suggests that the most recent, right-lateral fault system described above may have experienced activity since deglaciation and/or deposition of the sediments in the Holocene.

Above fault zone 1, 20 – 50 cm of poorly sorted subrounded heterolithic cobble-boulder gravel with silt-sand matrix fill is overlain by 10 – 50 cm of relatively massive light orange-brown silt, which returned an OSL age of 11,700 ± 1,510 yr BP (**OSL 1**, Table 2). The silt is overlain by ~50 cm of a poorly sorted clast-supported glaciofluvial gravel and thin (~30 cm) modern organic material and soil development in poorly sorted colluvium (Fig. 7C). Subvertical sedimentary-bedrock contacts such as seen here are known as buttress unconformities, and while they can be formed by glacial processes, they are a common feature of active fault strands and have been reported on active faults nearby (Sherrod et al., 2008; Montero et al., 2013; Personius et al., 2014). The slickenlines on the bounding bedrock plane supports a tectonic origin for this unconformity, which would suggest that the silt was deposited against a pre-existing (likely postglacial) tectonic scarp, and/or it has been displaced by the fault.

Above fault zone 2, a large (~8 x 5 m) clay-rich clast-supported cobble – boulder glaciofluvial gravel deposit fills irregular bedrock topography (Fig. 7D). Within ~50 cm of the plane of **F2-3** that bounds the deposit to the east, clay-rich seams with a weak along-plane foliation and several pebble – cobble clasts are aligned parallel to the adjacent fault plane (Fig. 7E)**.** A small (decimetre-scale) lens of well-sorted sandy pebble gravel also dips moderately to the north, mimicking the north-side-down bedrock topography and inferred slip sense of the fault zone it overlies (Fig. 7E). The alignment of sedimentary features may be the product of deposition on an irregularly shaped channel bed, or may suggest that postdepositional motion on **F2-3** rotated adjacent sediments into parallelism, a common feature of faulted gravels (McCalpin, 2009).

The sediments above fault zone 3, which consists of the intersection of **F2-2** and its conjugate (**F2-4**), comprise a thin (~50 cm) deposit of glaciofluvial gravel overlain by a wedge of bouldery colluvium that thickens progressively to the north up to ~3 m thick (Fig. 7E, Appendix C). Towards the northern limit of the sediment deposit, an ~15-cm-thick horizon of dark orange silty loam containing charcoal fragments radiocarbon dated to 1832 - 1968 cal yr BP (**RC 3**, Table 1), is buried beneath ~60 cm of bouldery colluvium with minor modern soil development (Fig. 7E, Appendix C). The position of the buried oxidized layer, interpreted as a paleosol, within the downdropped northern block of the fault zone suggests that the overlying wedge of colluvium may have been deposited coseismically off the free-face of a scarp (e.g. McCalpin, 2009).

Although there is some ambiguity as to the timing and nature of fault rupture at Site 2-A, subvertical buttress unconformities against slickenlined fault planes, parallel clast alignment and clay-rich seams, and burial of an oxidized charcoal-bearing loam beneath a wedge of colluvium are all suggestive of postglacial rupture of the right-lateral fault system described above.

4.2.3 Site 2-B

East of the Sooke River, at Site 2-B (Figs. 6, 8A), an ~100-m-wide zone of slickenlined fault planes of varying mineralogy and character is exposed in a road cut. Metre-scale gouge-bearing faults such as those at Site 2-A are absent here; fault planes instead consist of slickenlined surfaces with millimetre-scale coatings of quartz ± epidote ± chlorite, chlorite ± clay, or zeolite -

calcite ± iron-manganese oxide minerals. Kinematic axes from slip-sense indicators show a high degree of scatter, but overall are dominated by steeply north-northeast plunging P axes and striae (Fig. 8A). Strain inversion of all slip-sense indicator measurements (n=61, measured from 60 fault planes) produces a best-fit fault-plane solution of (094°/74°S) experiencing left-lateral transtension (Fig. 8A). However, the kinematic P axes of many measurements fall within the tensional quadrant of the fault-plane solution, indicating that they are inconsistent with the inversion (Fig. 8A, Marrett and Allmendinger, 1990).

The slickenlined fault planes at Site 2-B typically occur either isolated within relatively competent basalt or as metre-scale clusters of upward-splaying intersecting and *en échelon* planes. One such upward-splaying fault zone is represented by **F2-5**, which resembles an ~3-m-wide positive flower structure; strain inversion of slip-sense indicator measurements (n=8) suggests that this structure has accommodated right-lateral transpression along a fault dipping steeply to the north (266˚/78°N) (Figs. 8B, 9). Another notable feature is an ~8 m wide abcess in the steep basalt walls where cobbles of *Qt3* are exposed above a strongly foliated chlorite-clay altered basalt shear zone along the Y axis of the fault zone (294°/65°N) (**F2-6**, Figs. 8C, 9). The topographic expression of **F2-6** can be projected to the east into a north-side-up bedrock scarp, which is paralleled by a second, more prominent north-side-up bedrock scarp (**F2-7**) ~20 m to the north (Figs. 8A, 9).

The inability to fit a fault plane solution to the majority of kinematic axes may be indicative of inconsistent kinematics over time (Allmendinger et al., 1989; Marshall et al., 2000), and fault sets and zones typically predict either left-lateral transtension or right-lateral transpression (Appendix A). Unfortunately I did not observe sufficient crosscutting relationships to constrain the relative timing of kinematic regimes at this site. I instead undertook geophysical surveys across the fault zone on adjacent terraces in hopes of identifying fault strands intersecting the deposits.

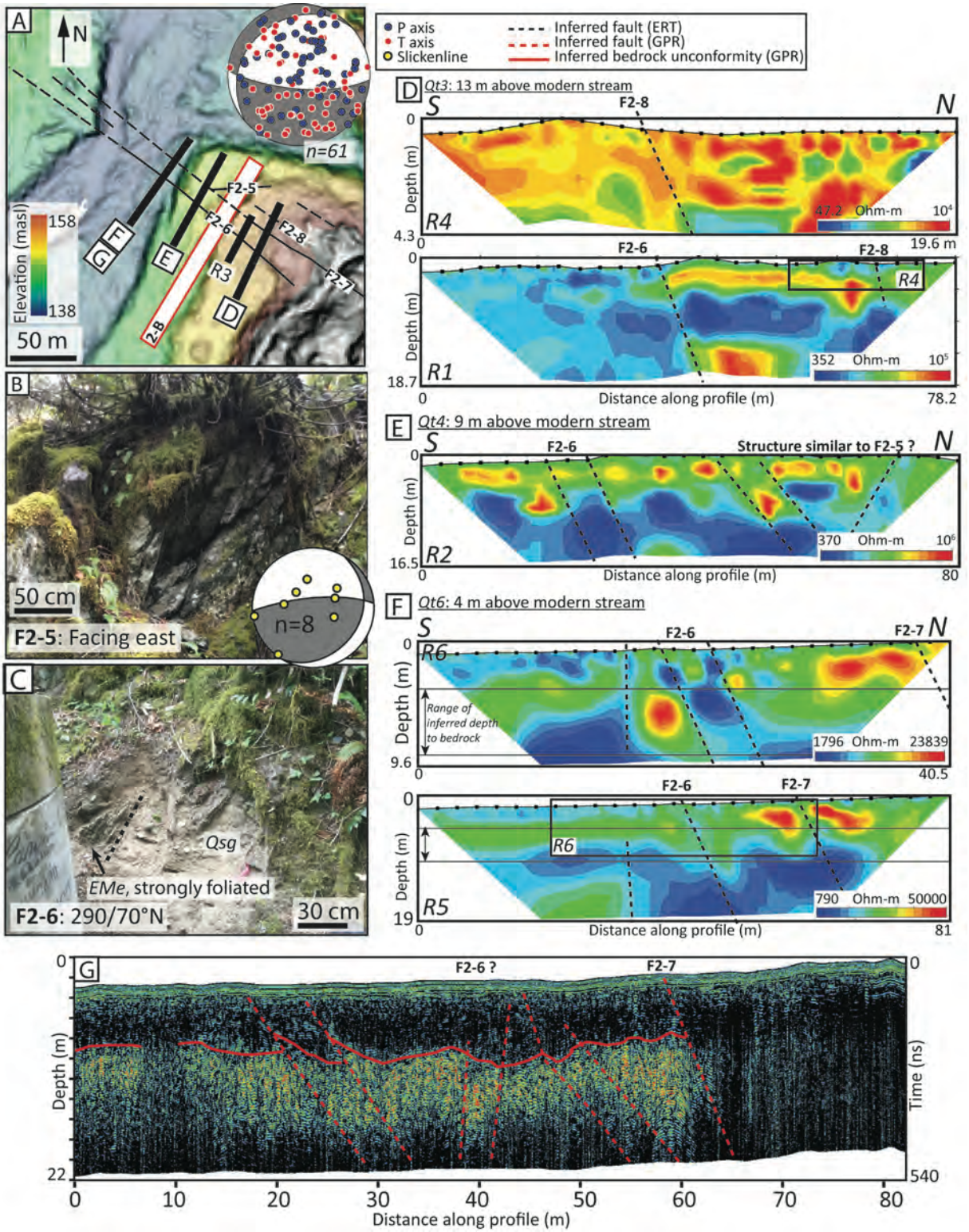
A
N
n=61
F2-5
F2-6
F2-8
F2-7
R3
G
F
E
D
2-8
Elevation (masl)
158
138
50 m
B
50 cm
F2-5: Facing east
n=8
C
Qsg
EMe, strongly foliated
F2-6: 290/70°N
30 cm
P axis
T axis
Slickenline
Inferred fault (ERT)
Inferred fault (GPR)
Inferred bedrock unconformity (GPR)
D Qt3: 13 m above modern stream
S
N
F2-8
Depth (m)
R4
47.2 Ohm-m
10⁴
4.3
19.6 m
F2-6
F2-8
R4
R1
352 Ohm-m
10⁵
18.7
Distance along profile (m)
78.2
E Qt4: 9 m above modern stream
F2-6
Structure similar to F2-5 ?
R2
370 Ohm-m
10⁶
16.5
80
F Qt6: 4 m above modern stream
F2-6
F2-7
R6
Range of inferred depth to bedrock
1796 Ohm-m
23839
9.6
40.5
R5
790 Ohm-m
50000
19
81
G
F2-6 ?
F2-7
Depth (m)
Time (ns)
22
540
0
10
20
30
40
50
60
70
80
Distance along profile (m)

Figure 9. (A) Selected elevation range draped over DEM-derived slope image, showing the location of geophysical profiles along strike from the fault zone exposed at Site 2-B and prominent north-side-up bedrock scarps (F2-6, -7). Stereonet shows kinematic axes and fault plane solution from strain inversion of all slickenline measurements at Site 2-B (n=61). (B) Outcrop photo of the intersecting slickenlined planes that comprise F2-5; Fault plane solution from strain inversion of slickenlines (shown in yellow). (C) Strongly foliated chlorite-clay altered Metchosin Igneous Complex of F2-6 beneath a sloughing cobbly slope that forms a recession in the otherwise bedrock-dominated road cut of Site 2-B. (D) ERT along the uppermost terrace (Qt3) centred on the projection of F2-6 (R1, bottom), showing a steeply north-dipping resistivity contrast that coincides with the north side up topography of F2-6. A higher resolution profile (R4, top) at the north end of R1 shows irregular resistive domains, with a second steeply north-dipping contrast extending downward from an east-southeast-trending lineament with south-side-up topography (F2-8, Appendix C). (E) ERT along the mid-level terrace (Qt4) centred on the projection of F2-7, showing a break-in-slope and irregular resistivity structure. (F) ERT along the lowermost terrace (Qt6) showing steeply north-dipping resistivity structure beneath a very minor break in slope. A higher resolution profile (R6) centred on the feature of interest shows relatively consistent structure, inferred to intersect postglacial deposits above the bedrock unconformity defined by GPR imagery (Fig. 8D). (G) GPR imagery along the lowermost terrace (Qt6). A sharp contrast at ~60 m separates a zone to the north that lacks coherent reflectors. A sub-horizontal interface that appears to exhibit offset is inferred to represent the bedrock-sediment interface.

4.2.4 Resistivity and GPR across terraces

I focus my study on terraces *Qt3*, *Qt4*, and *Qt6* east of the Sooke River, along strike from the exposed brittle fault zone at Site 2-B. I assume that this *Qt4* was deposited in the same time period as the matched terrace across the Sooke River (**RC 7**, 7313 – 7423 cal yr BP) and that the *Qt3* surface is older than this, but younger than the 11,700 ± 1,510 yr BP OSL age of *Qt2* above Site 2-A. Sediments from the youngest terrace, *Qt6*, produced disparate radiocarbon dates, the older being 2008 – 2141 cal yr BP (**RC 2**, Table 1).

Sparse outcropping of Metchosin Formation at the surface of *Qt3* indicates that the sediment cover is relatively thin and the road cut at 2-B, which cuts through the edge of *Qt3* indicates that depth to bedrock is highly spatially variable. Similarly, smoothed Metchosin Formation outcrops exposed on the lower side of *Qt4* come within 3 m of the terrace surface locally, but are not observed in the cobbly slopes along most of the riser. The fault zone exposed

in Metchosin Formation basalt at Site 2-B consists of several intersecting mesoscale planar fractures, which are expected to control fluid flow and affect the resistivity structure of the subsurface. The surfaces of *Qt6* and *Qt4* arch broadly upwards over the fault zone (Fig. 8A), potentially as a secondary feature of the surfaces. It's worth noting that in 1864, the discovery of placer gold hosted in hydrothermal quartz veins within the Leech River Complex prompted a gold rush, and a townsite west of the Sooke River accommodated up to 4000 people for a short time (Dunae, 2016). Although there is little evidence of settlement now, I consider it likely that the terrace surfaces were disturbed during placer mining operations in the area, potentially obliterating any tectonic scarps that may have existed.

Resistivity and GPR surveys along terraces *Qt3*, *Qt4*, and *Qt6* east of the Sooke River are centred on the projection of **F2-6,** which continues through the terraces as a minor break in slope (Figs. 8A, 9). The topography, ERT and GPR profiles presented here are insufficient to resolve the complexity of the fault zone observed at Site 2-B, and the resulting interpretation (Figs. 8A, 9) represents only a very simplified proposed geometry. Tomography from an ~80-m-long resistivity transect along *Qt3* (Fig. 8D, R1) reveals a steeply north-dipping contrast extending from the break in slope at the surface (**F2-6**) to ~15 m depth, separating relatively conductive materials to the south from resistive materials to the north. Conductive anomalies immediately south of the contrast are likely associated with the clay-rich shear zone (**F2-6**) and overlying sediments exposed in the ~8 m wide recess of bedrock at Site 2-B (Fig. 8C). It is difficult to locate precisely the projection of **F2-7** on this ERT profile, and there is no obvious associated resistivity contrast.

Interestingly, transect R3, which was collected only ~20 m west of R1 at a higher -resolution, exhibits quite different, complex structure (Appendix C), possibly as a result of intersecting fault strands in the Metchosin Igneous Complex. Some contrasts in resistivity structure may be the result of sediments infilling irregular bedrock topography, although with the exception of **F2-6** I would expect this to occur at most over the top 2—3 metres of the 9 m deep profile, since bedrock was observed within 20 cm of the surface at numerous places adjacent to the survey line. The lack of an identifiable anomaly associated with **F2-6** in transect R3 suggests that the fault strand may be discontinuous or slightly offset, exhibiting more complexity than

topography and geophysics profiles allow me to resolve. Nevertheless, the north-side-up topographic expression of **F2-6**, and the northward dip both imaged by R1 and measured in bedrock at Site 2-B, suggest that it may accommodate some component of thrust offset. .

Another zone of lateral contrasts in resistivity ~27 – 30 m north of **F2-6** corresponds to a subparallel subtle south-side-up break in slope (**F2-8**, Fig. 8A, Appendix C) . Higher resolution resistivity tomography traversing this break in slope (Fig. 8D, R4), shows a steeply north-dipping resistivity contrast extending towards the surface break as well as several complex disturbances of resistive domains. This complex resistivity structure is likely representative of the complex bedrock fault zone observed ~20 m to the west and it is unclear whether disturbances intersect the overlying sediments, which are likely relatively thin.

An ~80-m-long resistivity transect ~50 m west of R1, along *Qt4*, also reveals a steeply north-dipping contrast in resistive domains beneath the projection of **F2-6** (Fig. 8E, R2). The tomographic profile extends to a depth of ~15 m below the surface, and is characterized by an upper resistive layer above a more conductive base, with irregular resistive anomalies between 5 – 10 m depth. Inverted resistivity values measured beneath *Qt4* (R2) are unrealistically high, likely due to the high measured contact resistance of the dry upper gravels. These resistive anomalies may represent sedimentary infilling of irregular bedrock structure, which is supported by an increase in reflector strength in colocated GPR profiles (Appendix C) near the horizontal resistivity contrasts. One moderately resistive anomaly occurs at the base of the profile, just north of the downward projection of **F2-6** (Fig. 8E).

I consider the possibility that resistivity structure beneath terraces *Qt3* and *Qt4* could be the result of lateral heterogeneity in sedimentation above the Metchosin Igneous Complex. However, because field observations constrain sediment depth to as little as 20 cm in places, sedimentary properties are unlikely to account for anomalies in the lower portion of profiles, which reach to greater than 15 m depth. However, at Site 2-B, the bedrock-sediment interface is observed to lie ~ 8 m below the surface of *Qt3* at the fault zone **F2-6**, suggesting that sedimentary infilling of irregular bedrock structure may account for variability to at least this depth locally. The

inference, supported by bedrock observations, that the majority of the tomography images bedrock rather than sediments, and the fact that resistivity structure has similar geometry to bedrock faulting observed <20 m along strike, leads to my interpretation of resistivity anomalies as fault-related features.

Two resistivity profiles along the lower terrace, *Qt6*, image to depths of ~17 m (R5) and ~9 m (R6, Fig. 8F). Both profiles illustrate steeply north-dipping resistivity structure extending to the ground surface beneath the projection of **F2-6.** Similarly to the ERT profile on Qt4, profiles R5 and R6 are characterized by resistive upper layers (5 – 7 m thick) over a relatively conductive base. The higher resolution profile (R6) shows a steeply north-dipping 4—5-m-wide conductive anomaly beneath the projection of **F2-6**, a structure that is mimicked in R5. Profile R6 also images an ~1-m-wide, near-vertical conductive anomaly to the south of the north-dipping conductive anomaly (Fig. 8F). Three colocated GPR profiles on the lower terrace (Fig. 8G, Appendix C) consistently image a strong contrast in reflective domains 3 – 8 m below the surface, broadly consistent with the horizontal contrast in resistive domains, which I interpret as the bedrock-sediment interface. Alternatively, this interface could represent sedimentary structure or the water table. However, because the presence of water is generally associated with a decrease in reflection strength and limits the investigation depth due to attenuation effects (Neal, 2004), I consider the observed increase in reflection strength at this interface to be inconsistent with fluid saturation. The presence of scattered hyperbolae caused by dispersion around boulders are observed above the interface, while hyperbolae below are vertically aligned, as is more characteristic of bedrock radargrams (Appendix C, e.g. Reynolds, 2011)

Several steeply dipping discontinuities appear to offset reflectors below the inferred bedrock unconformity, some of which extend upwards possibly offsetting the inferred unconformity itself and the sediments above (Fig. 8G, Appendix C). These include irregularities near the centre of the profile (projection of **F2-6**), and possible *en échelon* thrust offsets of the interface between 20 – 30 m along profile (Fig. 8G). The northern ~20 m of the GPR profile has very weak and incoherent reflectors, similar to what was observed in the clay-rich upthrown northern block of **F1-1** (Fig. 5D). While GPR imagery beneath *Qt6* does exhibit some features, such

as discontinuities with apparent offset, that may be expected in a complex fault zone like that observed along strike at Site 2-B, the poor data quality of radargrams does not allow for a robust interpretation of structure.

However, superimposing the inferred bedrock depth onto colocated ERT profiles (Fig. 8F) suggests that the steeply north-dipping resistivity contrasts do indeed extend through the fluvial sediments of *Qt6*. Although lateral variation in resistivity near the surface of the terrace could easily be ascribed to variations in sedimentation, the continuity of resistivity structure from the base to the top of ERT profiles suggests that it is not attributable solely to sediment variations. Given the similarity of the resistivity structures with others imaged along strike (e.g. the steeply north-dipping conductive anomaly in R1) and observed in outcrop at Site 2-B, I interpret these structures as brittle fault strands that intersect the Holocene sediments of *Qt6*, and have therefore ruptured since its deposition. Assuming that the older radiocarbon age of 2008 – 2141 cal yr BP (**RC 2**, Table 1) reliably represents the sediments of Qt6, it places a constraint on the maximum age of rupture for this strand.

4.2.5 Site 2 Summary

The repetition of inferred subvertical and steeply north-dipping fault planes along geophysical profiles, the north-side-up topographic signature along strike to the east, and bedrock observations, lead to the interpretation that the most recent activity on the fault zone at Site 2-B is associated with a positive flower structure or compressional duplex and linkage zone (Fig. 9).

Fault strands from both Site 2-A and Site 2-B resemble sets of *en échelon* R shears, oriented slightly clockwise relative to the main strike of the fault zone, and to ductile deformation fabrics observed nearby (Fig. 9). The complexity of the fault zone, as observed in bedrock at Site 2-B, is not adequately resolved using ERT and GPR imagery, and the resulting interpretation is an oversimplification of the true fault geometry. I have delineated only fault strands that I consider have a reasonable probability of being through-going structures (Fig. 9). Other possibly notable structures at Site 2-B include the complex brittle fault zone (**F2-5**), which strikes 10-20° counterclockwise relative to the Y axis, possibly forming as a linkage between *en échelon* R shears.

Evidence for Quaternary activity in the Site 2 area includes buttress unconformities and a possible colluvial wedge at Site 2-A, upwardly warped terrace surfaces and geophysical contrasts extending through postglacial gravels along strike from brittle faulting at Site 2-B, and two metre-scale zones of near-vertical clast alignment that are observed within poorly sorted clay-rich glaciofluvial gravel between Sites 2-A and 2-B in exposed terrace sediments along the west bank of the Sooke River, within *Qt4* Leech and *Qt6* Sooke (Fig. 9). The geometry of recent faulting at Site 2 appears to be consistent with Riedel shear development within a dextral system, due to the clockwise orientation of *en échelon* R strands relative to the main fault trend. The north-side-up scarp imaged in resistivity tomography (**F2-7**) extends eastward in Metchosin basalt for ~3 km until it again intersects Quaternary deposits at Site 3.

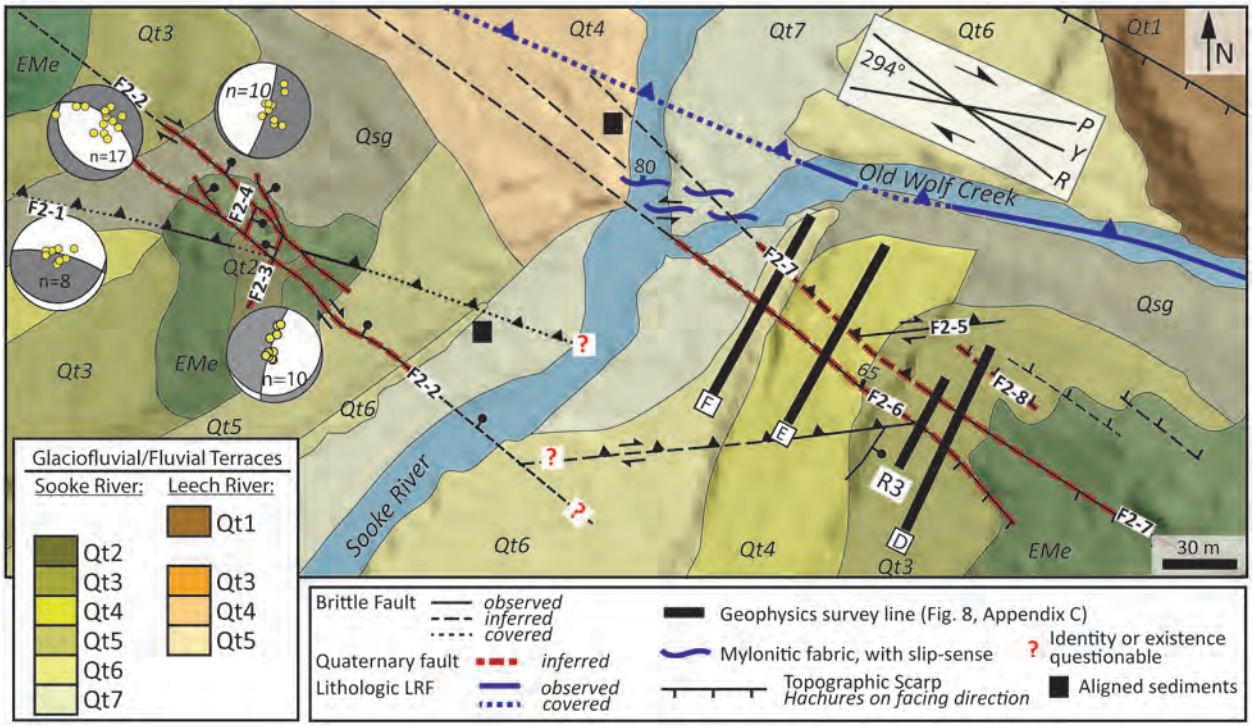

Figure 10. Site 2 schematic within a Riedel shear framework produced from fault mapping at Site 2-A, and outcrop observations, topography, and geophysical imagery at Site 2-B. Outcrop observations at Site 2-B indicate that the fault zone is very complex; ; geophysical profiles and topography do not allow for constraint on the fault zone complexity, and represent only a very simplified proposed geometry.

4.3 Site 3

At Site 3, topographic lineaments, geophysical imagery, and bedrock observations reveal a complex fault zone cutting through Metchosin Formation basalt for over 5 km along strike, with evidence for faults intersecting Quaternary deposits locally(Fig. 10A, Appendix D). The area is dominated by thick till deposits, visible in LiDAR imagery as smooth streamlined hillslopes and observed in the field as well-cemented clay-rich diamict up to 35 m thick. Brittle fault zones are exposed in Metchosin Formation bedrock at four locations along Jack Main West Road (Sites 3-A – D), a logging road that trends parallel to Old Wolf Creek. Relatively undeformed schist of the Leech River Complex is exposed in Old Wolf Creek, constraining the lithologic Leech River fault to lie within ~200 m of the brittle fault zone.

At the west end of Site 3, an ~4-m-high north-side-up scarp of brittly deformed Metchosin Formation (Fig. 10A; Morell et al., 2017) extends for ~ 3 km farther west to Site 2-B (**F2-7**). The scarp can be traced discontinuously ~500 m farther east, into the northern of two subparallel topographic lineaments (**F3-1**, **F3-2**) cutting a till-blanketed slope along an azimuth of ~292°, parallel to the Y axis of the fault zone (Fig. 10B, Appendix D).

Approximately 20 m south of **F3-1**, a linear depression ~8 m wide (**F3-2**) extends eastward to Site 3-A where it is exposed as a steeply north-dipping strongly foliated shear zone up to 8 m wide (280°/75°N, Fig. 10C). The shear zone exhibits a well-developed scaly fabric, with clay-rich fracture planes separating centimetre-scale lenses of strongly chlorite-altered basalt. The southern boundary of the shear zone abuts a steep plane of relatively competent basalt, while till overlies the northern portion of the shear zone, progressively thickening to the north and obscured by slumping (Fig. 10C). Slip-sense indicators on fractures within the scaly fabric are sparse (n=4), but consist of strike-slip and oblique slip slickenlines. A centimetre-scale clay seam (**F3-3**, 335°/58°E) crosscuts the scaly fabric of **F3-2** and continues upwards to the southeast into a slickenlined bedrock fault plane with a thrust/right-lateral sense of motion (Fig. 10C).

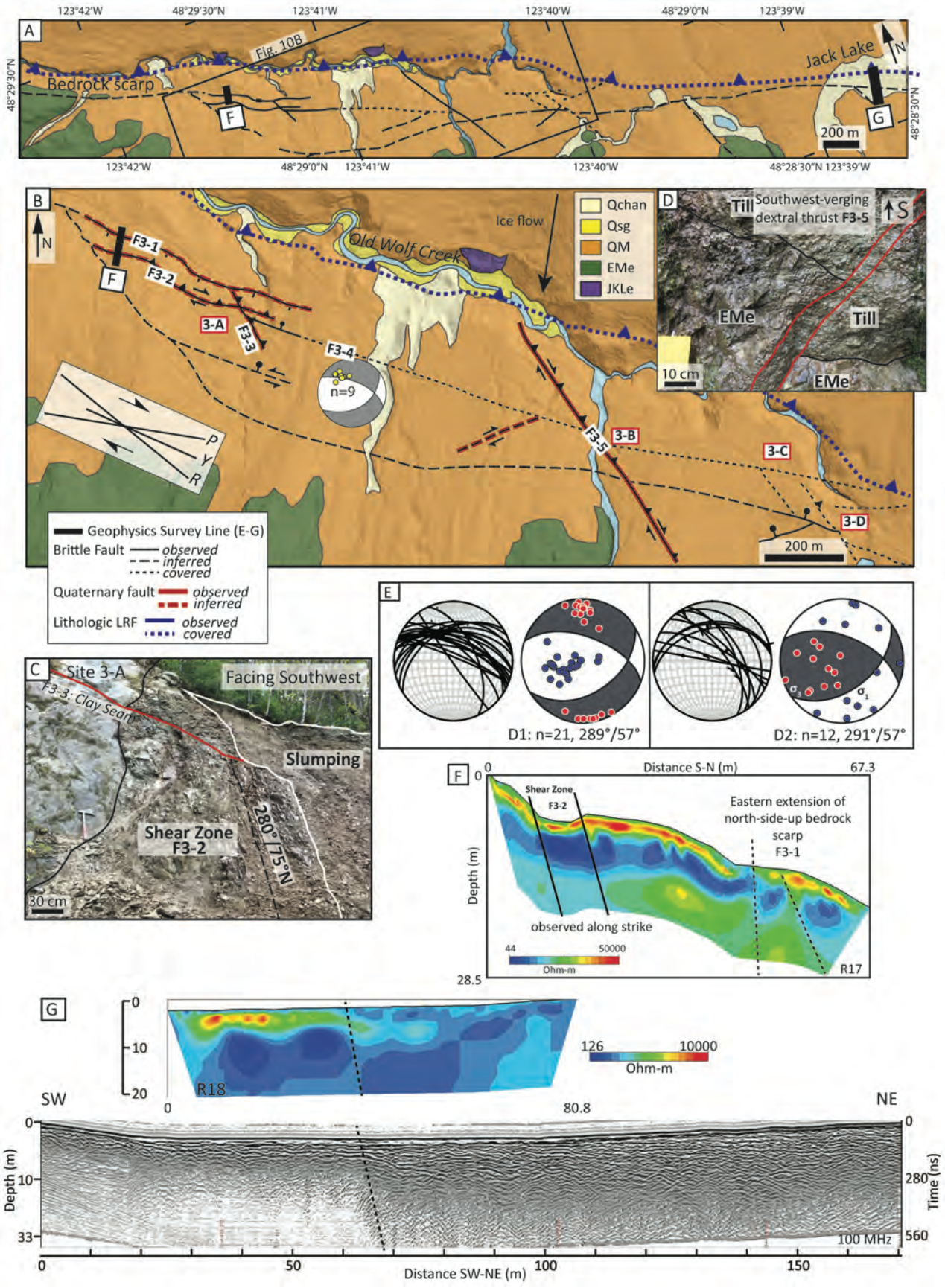
A
123°42'W
48°29'30"N
123°41'W
123°40'W
48°29'0"N
123°39'W
Fig. 10B
Bedrock scarp
Jack Lake
F
G
N
200 m
48°28'30"N
B
Qchan
Qsg
QM
EMe
JKLe
Ice flow
Old Wolf Creek
F3-1
F3-2
3-A
F3-3
F3-4
n=9
F3-5
3-B
3-C
3-D
P
Y
R
Geophysics Survey Line (E-G)
Brittle Fault observed inferred covered
Quaternary fault observed inferred
Lithologic LRF observed covered
D
Till
Southwest-verging dextral thrust F3-5
S
EMe
Till
10 cm
C
Site 3-A
Facing Southwest
F3-3: Clay Seam
Slumping
Shear Zone F3-2
280°/75°N
30 cm
E
D1: n=21, 289°/57°
D2: n=12, 291°/57°
F
Distance S-N (m)
0
67.3
Shear Zone F3-2
Eastern extension of north-side-up bedrock scarp F3-1
Depth (m)
observed along strike
44
50000
Ohm-m
28.5
R17
G
0
10
20
R18
126
10000
Ohm-m
SW
NE
80.8
Depth (m)
33
Time (ns)
280
560
100 MHz
Distance SW-NE (m)
50
100
150

Figure 11. (A) Surficial materials and fault strands in Site 3 area, location of geophysical surveys. (B) Fault strands and surficial materials, locations of bedrock fault exposure and inferred fault strand geometry (C) Shear Zone F3-2 at Site 3-A, with F3-3 crosscutting main shear fabric. (D) F3-4 at Site 3-B: Metchosin basalt within an ~8 m wide gouge-bearing fault zone possibly thrust over lodgement till. (E) Fault plane measurements with slickenlines, and strain inversion for slip-sense indicator measurements. Blue dots: kinematic P axes, Red dots: kinematic T axes, σ_1 and σ_3 are from stress inversion of regional crustal seismicity fault plane solutions. (F) Resistivity tomography along line F on Fig. 10A, B, showing F3-1 and F3-2. (G) Electrical resistivity tomography across Jack Lake (GPR profile located on Fig. 10A) and 100 MHz GPR across a parallel transect, from Bednarski (2016).

Also exposed in the quarry at Site 3-A, within ~100 m to the southeast of **F3-2**, are *en échelon* normal faults with a character and mineralogy distinct from that described above. These fault planes typically consist of slickenlined millimetre-scale quartz-epidote-chlorite coating, with clusters of millimetre-wide euhedral crystals of a pale blue soft asbestisform mineral locally, consistent with the metamorphic assemblages of accretionary fractures in the area (Timpa et al., 2005). Strain inversion of slip-sense indicators (n=9) from these faults at Site 3-A defines a left-lateral transtensional fault dipping steeply to the north-northeast (**F3-4:** 294°/61°N). This style of faulting is observed at all four bedrock fault exposures (Sites 3-A – D), as steeply north-northeast-dipping left-lateral and normal faults subparallel to the Y axis (~290°/70° N), moderately dipping normal left-lateral strands oriented between 20-40° counterclockwise from the Y axis, and sparse conjugate strands at high angles to the Y axis. Kinematic axes from slip-sense indicators on these fault planes (n=21) show high consistency, and indicate a left-lateral transtensional fault dipping moderately to the north-northeast (289°/57°N, Fig. 10F).

At Site 3-B, ~1 km along strike from Site 3-A, a clay-rich gouge-bearing fault zone up to 8 m wide (**F3-5**) has a dominant structural grain of ~320°/55° E , similar to the orientation of **F3-3** (Fig. 10B). At one location within the fault zone, the contact of Metchosin Formation basalt with the overlying lodgement till exhibits ~30 cm of apparent thrust offset (Fig. 10D), suggesting that this fault strand has ruptured since the Fraser glaciation. The Metchosin Formation within the fault zone is intensely clay altered and moderately foliated intermittently. The till consists of a well cemented, unstratified sandy diamict with abundant pebbles, which extend downwards for ~30

cm into the centimetre-scale gouge-bearing fault that offsets its basal contact (Fig. 10D). The entire fault zone is intensely clay altered, and forms an above-ground spring, making sedimentary structures difficult to distinguish. A weak shear fabric ~10 cm wide can be seen extending upwards into the till at a dip of 55 – 60° for ~50 cm before it becomes indistinguishable. The basal contact of the till is several metres higher on the northeast side of the fault zone than the southwest, suggesting that the directly observed offset may be one of several obscured by thick moss growth over the saturated fault zone. This could conceivably be the result of proglacial thrusting, where the lateral compression from an advancing glacier can produce thrust sheets. Proglacial thrust sheets most commonly occur at low angles, cutting till and other unconsolidated sediments, though they are also documented displacing bedrock (Lee and Phillips, 2013; Pedersen, 2014). Alternatively, pressure from overriding ice may have injected till downwards into the fractured bedrock, but this does not easily account for the displacement of the basal contact and emplacement of intensely clay altered basalt above the till. The upwardly thrust basalt is not a detached block, but continues downwards into the intensely altered fault zone for at least 2 m. If this is the result of glaciotectonic processes, it is unusually localized, as no similar evidence is observed nearby. The oblique angle to ice flow, offset of the sediment-bedrock unconformity, and continuation into a gouge-bearing fault within a Quaternary-active brittle fault zone (Morell et al., 2017) lead me to interpret **F3-5** as a tectonic fault that has ruptured since the deposition of the till, presumably during the Fraser glaciation.

Bedrock topography and sparse (n=3) slip-sense indicators from within the larger (8 m wide) fault zone (**F3-5**) indicate a southwest-verging thrust with some component of dextral motion. The clay-rich nature of this fault zone, and the field evidence for displacement of late Quaternary till, indicates that this fault represents the most recent kinematic regime. Exposed faulting to the east, at Sites 3-C and 3-D, lacks clay alteration and gouge, with mineralogy and character similar to that of the left-lateral transtensional fault exposed at Site 3-A (**F3-4**).

Fault plane mineralogy, evidence for Quaternary kinematics at Site 3-B, and crosscutting relationships at Site 3-A allow for slip-sense indicator measurements (n=33) from sites 3-A – D to be differentiated into a consistent older regime, D1 (n=21) and younger regime, D2 (n=12) (Fig.

10E). The older kinematic regime (D1) is one of sinistral transtension along a best-fit fault plane of 289°/57°N, and is exposed at all four sites (3-A – D). The younger kinematic regime (D2) has a nearly identical best-fit fault plane solution (291°/57°N) to the older regime, but reveals right-lateral oblique compression (Fig. 10E). Fault planes **F3-3** and **F3-5** are both included in this most recent kinematic regime, which is shown at Site 3-B to likely be Quaternary. Common fault plane orientations between the two kinematic regimes, multiple slickenline directions on a single fault plane, and a higher degree of scatter in the younger fault data imply that a reversal in slip sense occurred, prompting reactivation along pre-existing faults.

Geophysical profiles over till-covered transects further constrain Quaternary fault geometry. On a till-covered slope at the west side of Site 3, I collected electrical resistivity measurements and GPR data along an ~80 m transect over the two subparallel topographic scarps of **F3-1** and **F3-2**. Resistivity tomography (Fig. 10F) below **F3-1** reveals steeply dipping resistivity contrasts branching upward from an ~5-m-wide steeply south-dipping resistive anomaly beneath the north-side-up topographic scarp. Forty-five metres to the south, an ~10-m-wide steeply north-dipping conductive zone (**F3-2**) manifests in topography as an ~8 m wide depression. While topography of **F3-1** clearly indicates north-side-up offset of the north-facing slope, **F3-2** does not seem to be associated with significant dip-slip displacement of the surface, and the prominent topographic expression cutting the smooth till-covered slope may represent strike-slip components of Quaternary motion or differential weathering.

Inferred steeply north-dipping fault geometry, similar to that of **F3-2**, is also observed in ERT and GPR profiles along the southern boundary of Jack Lake, at the eastern extent of Site 3 (Fig. 10A). The area surrounding Jack Lake is covered by thick till overlying the fault zone for several kilometres, with no observed bedrock exposure or obvious topographic scarps. Nevertheless, geophysical imagery (Fig. 10G; Bednarski, 2016) reveals strong resistivity and reflector contrasts across a steeply north-dipping plane along strike from the linear southern boundary of Jack Lake reservoir. Bednarski (2016) interpreted this GPR imagery (Fig. 10G) as representing a bouldery gravel deposit that thickens to the north-northeast as it overlies a north-side-down bedrock lineament. The steep contrast in reflector strength observed in GPR imagery

does not extend through continuous reflectors in the upper 5 m of the radargram, suggesting that the sediments overly the lineament unconformably (Bednarski, 2016), despite a strong contrast in resistivity across the same area (Fig. 10G). Although this imagery does not provide compelling evidence for Quaternary motion, it does identify a bedrock fault strand with reasonable certainty.

4.4 Site 4

In the Site 4 area, ~2.5 km to the east along strike from Site 3, several subvertical scarps of Metchosin Formation basalt protrude through a 5-km-long till-blanketed ridge, which was interpreted by Morell et al. (2017) as a series of pressure ridges (Fig. 11A). The exposure of abundant thrust fault planes in bedrock along the southern edge of the ridge and within two steep-sided transversal gorges (Sites 4-C, D) supports the hypothesis that localized tectonic uplift has contributed to the topographic rise. Bedrock exposures constrain the lithologic Leech River fault to the northern edge of the ridge, and additional brittle faulting is observed in the Leech River Complex at two sites along the Goldstream River to the north (Sites 4-E,F, Fig. 11A).

Discrete steeply north-northeast-dipping thrust faults (**F4-1**,~280°/65°N) with a relatively minor component of sinistral motion are exposed in Metchosin Formation basalt at two sites along the southwest flank of the ridge (Sites 4-A,B), as well as in the eastern gorge (Site 4-C) where they are associated with conjugate west-verging thrust faults (Fig. 11A). At Site 4-A, **F4-1** is crosscut by a northeast-dipping sinistral oblique fault with sets of both subhorizontal and moderately plunging slickenlines (333°/65°E) (Appendices A, E). These bedrock fault planes are overlain by 15 – 20 m of glacial till, sand, and gravel, that do not exhibit clear signs of tectonic - deformation. However, an ERT profile centred on a subtle ridge subparallel to **F4-1** (Figs. 11A, 11B, Appendix E) reveals metre-scale subvertical conductive anomalies extending to within 5 m of the surface, potentially representing faults intersecting till. While the 15 – 20 m thick package of glacial sediments is observed within 40 m to the southeast of the conductive anomalies and less than 10 m from the south end of the tomography, it is of course possible that bedrock extends to the near-surface here and that till is represented only by the upper resistive layer (2 – 4 m thick) which does not exhibit strong resistivity contrasts (Fig. 11B). A second ERT profile on the north

side of the ridge (Fig. 11C) crosses two subtle parallel lineaments on an otherwise relatively smooth till-covered slope (Appendix E), and similarly reveals two metre-scale steeply north-dipping conductive anomalies that here extend to the ground surface.

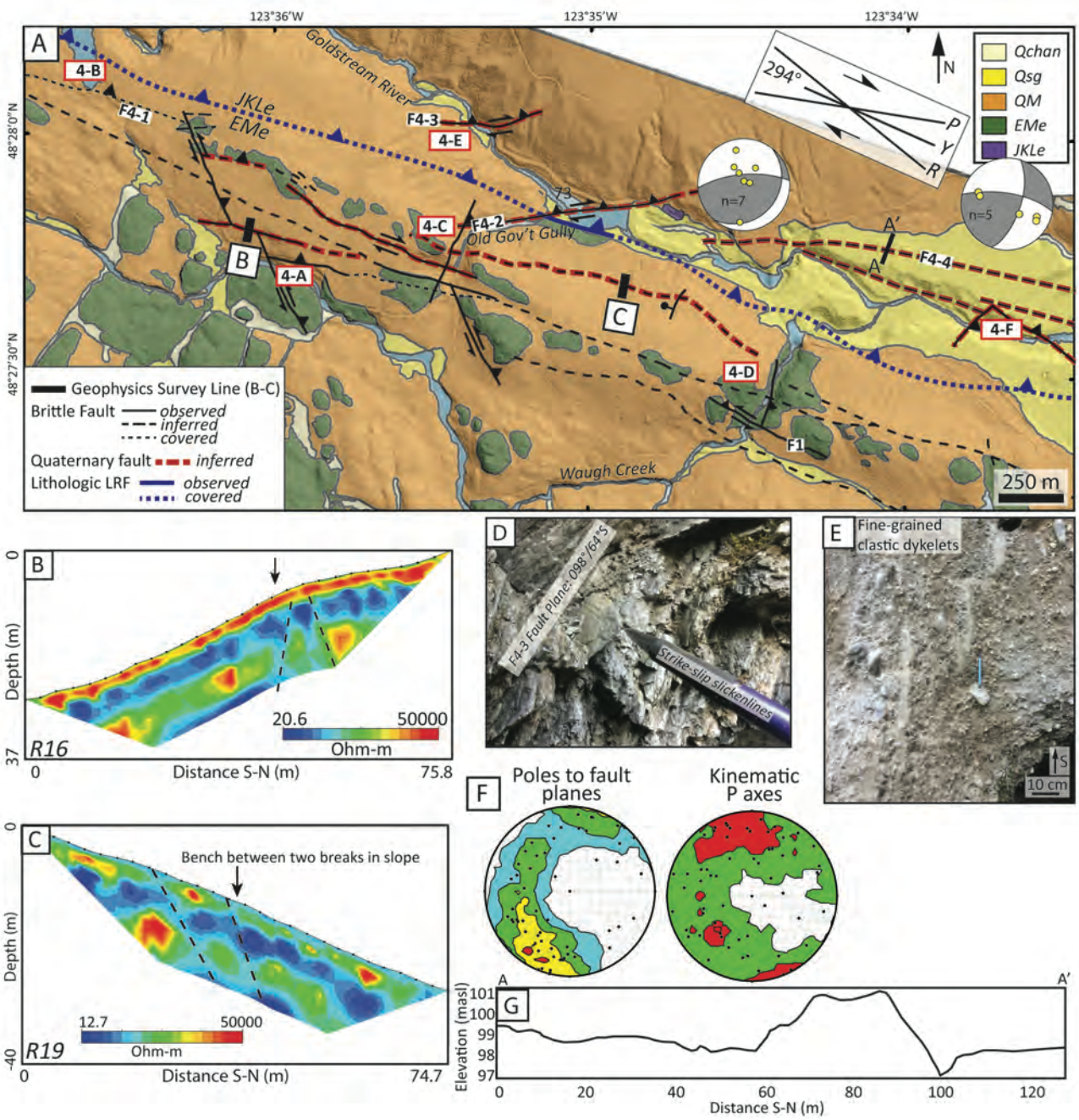

Figure 12. (A) Surficial material and fault strands in the Site 4 area, selected fault plane solutions, locations of detailed study sites and ERT surveys. (B) ERT of Line B, with arrow indicating break-in-slope delineated on Fig. 11A. (C) ERT of Line C, Fig. 11A. (D) Field photo of slickenlined gouge-bearing fault planes in Leech River Complex at Site 4-E. (E) Centimetre-scale fine-grained clastic dykes on the south bank of the Goldstream River, along strike from observed brittle faulting. (F) Poles to fault planes and associated P axes of all slip-sense-indicator measurements within Site 4; contour intervals represent two standard deviations. (G) LiDAR-derived topographic profile across linear ridge on the Late Pleistocene Colwood delta north of Goldstream River (location indicated on Fig. 11A).

The western gorge that transects the ridge at Site 4-C exposes > 300 m of distributed brittle faulting with many (n=40) slickenlined fault planes of varying mineralogy and character. At the north end of Site 4-C a metre-scale zone of upward-splaying slickenlined fault planes (n=7) resembles a right-lateral positive flower structure (**F4-2**), with a best-fit fault plane solution of 265°/73°N (Fig. 11A, Appendix E). This fault orientation can be extended along strike along the northern end of the western gorge and a small reservoir, consistent with the north-side-up displacement predicted from slip-sense indicators.

Five hundred metres north of Site 4-C, brittle faulting is observed within the Leech River Complex at two sites along the Goldstream River (Sites 4-E-F). At Site 4-E, friable, graphitic schist with pervasive centimetre-scale quartz ± pyrite veining has sparse lineations (n=3) along fractured cleavage planes that define a steeply south-southwest-dipping dextral transpressive fault (102°/63°S, **F4-3**, Figs. 11A, 11D).

Two km along strike to the east, localized sub-metre scale faulting is observed within metabasalt and pelitic schist along the north bank of the Goldstream River (Site 4-F) and within ~100 m along strike, centimetre-scale sand dykes cut through sand and gravel deltaic foreset beds, possibly indicating liquefaction (Fig. 11E). Kinematic axes from strain inversion of slickenlined fault planes within the Leech River Complex (n=5, from Sites 4-E, F) are consistent with regional crustal stress and imply a steeply north-northeast-dipping right-lateral fault (**F4-3**, Fig. 11A). Further suggestion of postglacial activity is observed ~250 m to the north, where two *en échelon* linear ridges parallel to the fault plane solution of **F4-3** protrude from the otherwise flat terrace surface north of the Goldstream River (Figs. 11A, 11G Appendix E). These linear ridges can be traced along

strike in topography to a small northward flowing fall in the Goldstream River, further implying continued south-side-up displacement along a surface-rupturing fault strand.

Fault planes within the Site 4 area are generally steeply (60° – 80°) dipping and predominantly oriented in three directions: 1) along the Y axis, at a strike of ~294°, 2) clockwise ~30° relative to the Y axis, and 3) striking north-northeast, near perpendicular to the Y axis (Fig. 11F). Slip-sense measurements indicate dominantly shallow north-northwest and south-southeast trending P axes, consistent with those of the younger (Quaternary) generation of faulting identified at Site 3 (Figs. 10E, 11F). However, there is a high degree of scatter in kinematic axes, and a second dominant orientation of P axes plunges moderately towards the southwest, possibly indicating inconsistency through time (Fig. 11F).

4.5 Site 5

Outwash deposits of the Colwood Delta extend east from Goldstream beneath the cities of Langford and Colwood, covering the easternmost terrestrial extent of the lithologic Leech River fault (Fig. 12A; MacLeod et al., 1977). A previous seismic reflection profile along Ocean Boulevard (Fig. 12A) revealed an ~500-m-wide zone of distributed north-side-up subvertical discontinuities through bedrock and pre-Wisconsinan Quaternary sediments, but did not find evidence of faulted latest Pleistocene deltaic sediments (Bednarski, 2016). Here I present topographic, geophysical, and sedimentary evidence that suggests there is faulting of the latest Pleistocene deltaic sediments west of Ocean Boulevard. Brittle faulting is also observed in Metchosin Formation basalt at two sites along the southwest margin of the Colwood Delta, suggesting a possible southeastward splaying of fault strands towards previously mapped active faults in the Juan de Fuca Strait (USGS, 2010).

I map a subtle lineament trending ~290° intermittently from a prominent north-side-up bedrock scarp near Colwood Creek Park (A-A', Fig. 12A) for ~4 km towards the apparent fault zone imaged by Bednarski (2016) along Ocean Boulevard (**F5-1**) (Appendix F). Resistivity and GPR profiles across the lineament on the frontal slope of the delta show steeply north-dipping contrasts in the vicinity of the southern edge of a channel (Fig. 12D). ERT imagery reveals several

steep to subvertical contrasts in resistive domains, and resistive anomalies at the surface, and at depth (~12 – 20 m) over a width of ~15 m. GPR imagery along a parallel transect is poorly resolved, but reveals a single sharp, steeply north-dipping contrast in reflector strengh that corresponds to a similar structure in the ERT (Fig. 12D). Although the resistivity anomalies coincide with a modern channel, the sharp contrasts in geophysical properties extend to at least 10 m depth (Fig. 12D, Appendix F), making it unlikely that the geophysical anomalies are controlled by modern surface processes. The zone of subvertical to steeply north-dipping structures is also consistent with that imaged by Bednarski (2016) in Quaternary sediments ~1 km to the east along strike.

An excavation less than 200 m to the southeast from the geophysical profiles, on the distal foresets/ bottomsets of the delta (Site 5-C) reveals extensive liquefaction and north-south compressional brittle faulting (Fig. 12C). Locally, silty diapirs and flame structures in sand beds indicate liquefaction possibly caused by soft-sediment deformation during depositional stages (Appendix F). However, within ~5 m of this, sand beds are offset in a more brittle fashion, less characteristic of syndepositional deformation (Fig. 12C). The most impressive feature is a grey silt bed, radiocarbon dated to 14,038 – 14,324 cal yr BP (**RC 4**, Table 2), that is thrust > 1 m over the coarse-grained oxidized sand above (Fig. 12C, Appendix F). The faulting dies out upwards in distributed silt veinlets and shear seams, and no topographic expression was observed. A series of three sub-decimetre brittle thrust features of a sand bed underlies an open anticline to the east (Fig. 12C). Slickenline measurements (n=4) share consistent P and T axes and produce a best-fit fault plane solution of 265°/62° N thrust fault with a minor sinistral component (Fig. 12A). While these faulted sediments may be associated with crustal tectonism, it is also likely that this site, on the lower slope of the delta, was subject to compressional deformation due to subaqueous landslides. The presence of numerous landslide scarps and slumps to the west of the site supports a sedimentary origin for the faults, and I find no evidence to conclusively classify them as tectonic. Nevertheless, the faulted sediments are situated above a brittle fault zone that has been shown along strike to have caused surface rupturing earthquakes since the Fraser glaciation, and a tectonic origin should not be ruled out.

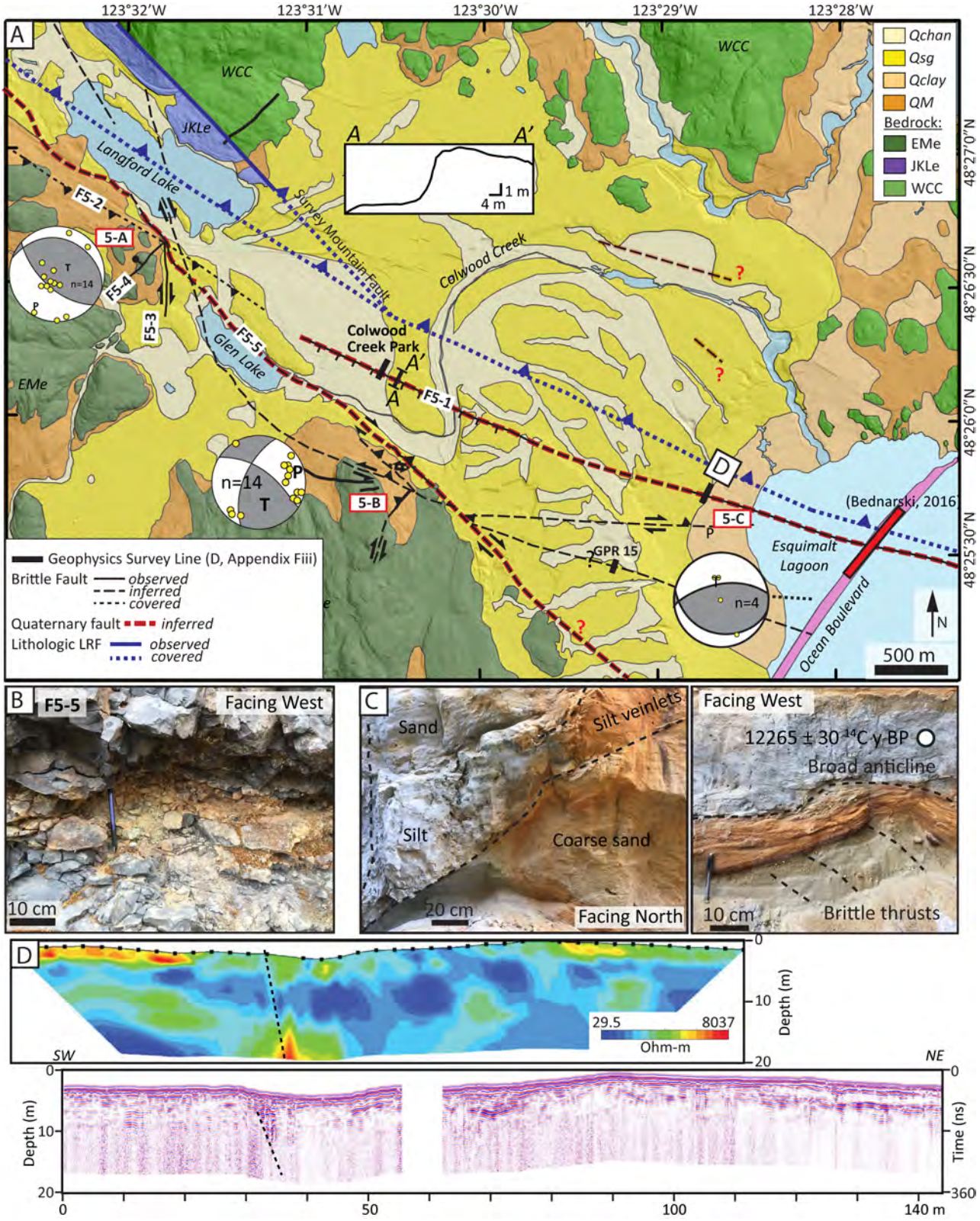
A
123°32'W
123°31'W
123°30'W
123°29'W
123°28'W
48°27'0"N
48°26'30"N
48°26'0"N
48°25'30"N
WCC
JKLe
Langford Lake
Sturvey Mountain Fault
Colwood Creek
Colwood Creek Park
Glen Lake
EMe
F5-1
F5-2
F5-3
F5-4
F5-5
5-A
5-B
5-C
n=14
n=4
GPR 15
Esquimalt Lagoon
Ocean Boulevard
(Bednarski, 2016)
Qchan
Qsg
Qclay
QM
Bedrock:
EMe
JKLe
WCC
1 m
4 m
500 m
N
Geophysics Survey Line (D, Appendix Fiii)
Brittle Fault observed
inferred
covered
Quaternary fault inferred
Lithologic LRF observed
covered
B
F5-5
Facing West
10 cm
C
Sand
Silt veinlets
Silt
Coarse sand
20 cm
Facing North
Facing West
12265 ± 30 ¹⁴C y BP
Broad anticline
10 cm
Brittle thrusts
D
SW
NE
29.5
8037
Ohm-m
Depth (m)
Time (ns)
0
50
100
140 m
360

Figure 13. **(A) Surficial materials, modified in part from Monahan & Levson (2000), lithologic contact (MacLeod et al., 1977), detailed field sites, and brittle fault strands in the Colwood Delta region. Stereonets represent best-fit fault plane solutions from slip-sense indicators of brittle faulting at Sites 5A – C. Red rectangle indicates width of apparent fault zone imaged in bedrock and pre-Wisconsinan glacial deposits by Bednarski (2016). (B) F5-5 at Site 5-B, shallow undulatory decimetre-scale gouge-bearing fault zone. (C) Faulted Holocene deltaic sediments from Site 5-C, showing both a metre-scale thrust and three brittle thrusts beneath a broad anticline. Radiocarbon sample of woody material was collected from the bed indicated, though not the exact location. (D) ERT from Thorlakson (2016) and GPR from Line D on Fig. 12A. Although the surveys are roughly colocated, they were collected one year apart, and discrepancies in along strike distance in the GPR profile, which was measured using a survey wheel, may account for differences in the topographic profile (derived from LiDAR DEM).**

Multiple generations of brittle faulting are observed in Metchosin Formation basalt outcrop at two sites along the southwest margin of the delta (Sites 5-A, B, Fig. 12A). At Site 5-A, south of Langford Lake, smoothed and striated quartz-epidote planes (n=8) define a steeply southwest-dipping thrust fault (**F5-2**, 122°/72° S) that undulates along the outcrop for ~20 m. Thin quartz-epidote ± chlorite ± hematite ± limonite ± calcite faults at high angles to the main fault (**F5-3**, n=3, 181°/77° W) are interpreted as right-lateral conjugates within a consistent, transpressional kinematic regime. Several steeply northwest-dipping chlorite-epidote altered decimetre-scale shear zones extend upward to apparent normal offset of the bedrock surface (**F5-4**, 220°/58° W), possibly representing relatively younger activity. These shear zones are crosscut by a gently undulating shallowly (10° - 20°) northeast-dipping fault containing ~20 cm of iron-oxide clay-bearing material, assumed because of its low angle to be a thrust fault (**F5-5**, Fig. 12A). A similar low-angle undulatory decimetre-scale fault zone (Fig. 12B) is observed ~2 km to the southeast at Site 5-B, also crosscutting several styles of earlier faulting. The two exposures of low-angle northeast-dipping faults of similar character occur along strike from one another, leading to the inference that this fault strand is semi-continuous between the two sites, and represents a relatively young regime of north-northeast directed compression, possibly forming the northern boundary of Glen Lake (Fig. 12A, Appendix F, Bednarski, 2016).

Slip-sense indicator measurements at Site 5-B (n=14) consistently show shallow northeast-southwest trending compressional axes, despite different mineralogy and characterization of fault

planes. Most slip-sense indicators comprise euhedral epidote crystal growth, on planes with quartz ± chlorite, leading to confident inference of slip sense and depth of activity. The consistency in kinematics of the sparse (n=3) planes with more clay-rich or thicker coating suggest that stress orientations have remained relatively constant over time. Minor counterclockwise orientation of P axes of more clay-rich fault planes such as **F5-5** are consistent with those from faulted deltaic sediments at Site 5-C.

5 Discussion

5.1 Late Quaternary activity on the Leech River fault zone

I present several lines of evidence that collectively suggest late Quaternary activity along the eastern half of the Leech River fault zone (Fig. 13A). Indicators of postglacial activity include direct observation of displaced glacial sediments at Sites 1 and 3, geophysical imagery of disturbed and offset Holocene sediments at Sites 2 and 5, topographic scarps and lineaments cutting Quaternary units, and sedimentary features such as buttress unconformities, aligned clasts, and clay-rich foliated seams. Offset Quaternary sediments are directly observed at Site 1, where paleoseismic trenching has confirmed 3 – 6 m of north-side-up displacement of schist, till, and colluvium along a subvertical fault (**F1-1**), and at Site 3, where the contact between Metchosin Formation basalt and the overlying lodgement till exhibits ~30 cm of apparent thrust offset on a moderately northeast-dipping gouge-bearing fault (**F3-5**). The prominent scarp of Metchosin Formation protruding ~4 m above a till-covered slope at the west side of Site 3, and the continuation of the topographic expression through a till-blanketed slope (**F3-1**), also suggests north-side-up displacement along a subvertical fault since the retreat of the Fraser glaciation (Morell et al., 2017).

At Site 2, evidence for Quaternary activity is less clear, but consists of steeply dipping contrasts in geophysical imagery along strike from observed brittle faulting, moderate to steep clast alignment in gravels along strike from observed faulting, and wedge-shaped deposits overlying gouge bearing fault zones at Site 2-A. For example, parallel clasts, foliated clay seams, and a pebble lens adjacent to a slickenlined fault plane in fault zone 2 implies that the sediments may have been rotated into alignment during motion on the fault, a diagnostic feature of faulted gravels (McCalpin, 2009).

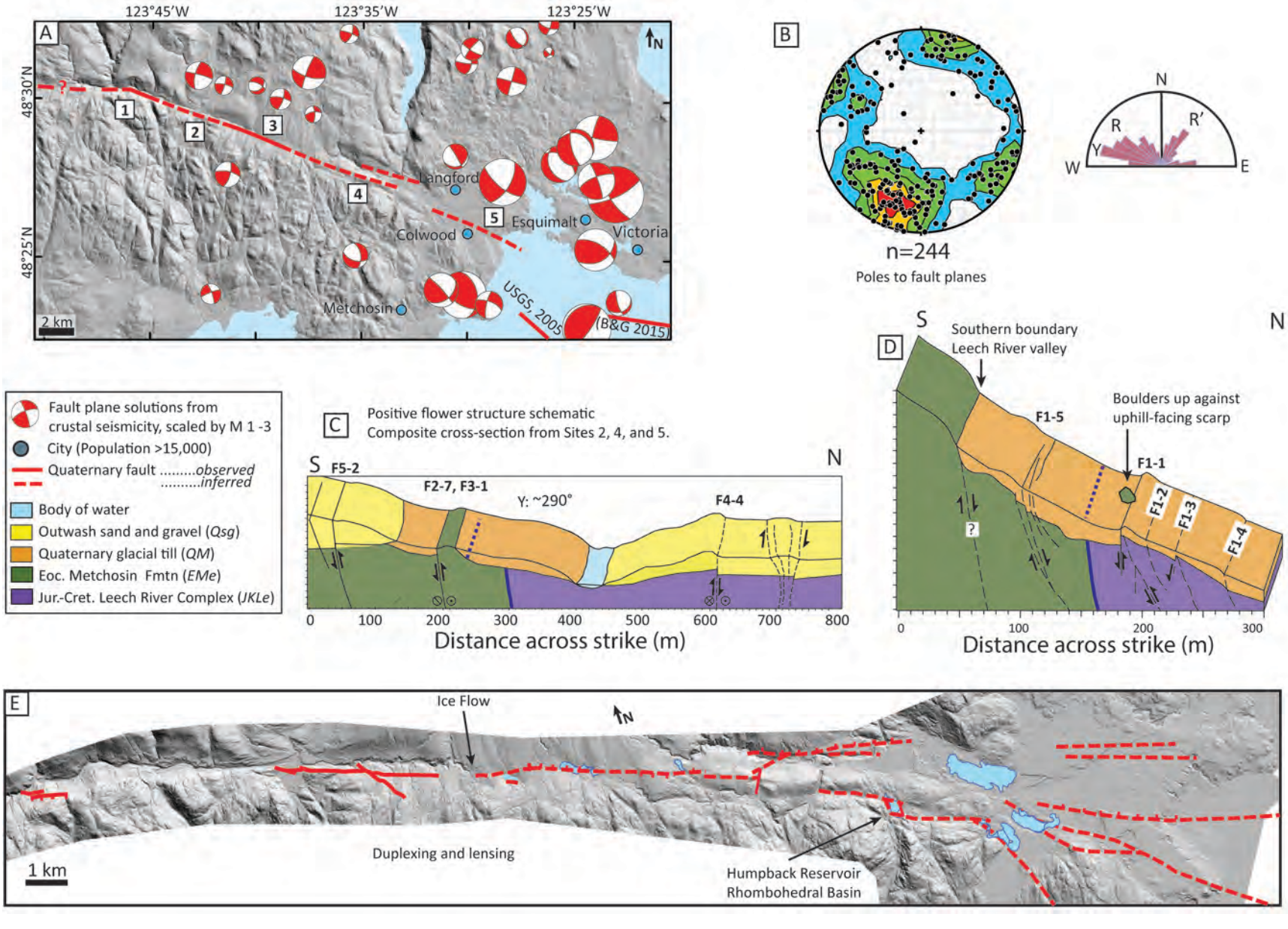
A
123°45'W
123°35'W
123°25'W
48°30'N
48°25'N
N
1
2
3
4
5
Langford
Esquimalt
Victoria
Colwood
Metchosin
USGS, 2005
(B&G 2015)
2 km
B
n=244
Poles to fault planes
N
R
R'
Y
W
E
Fault plane solutions from crustal seismicity, scaled by M 1 -3
City (Population >15,000)
Quaternary fault .....observed
.....inferred
Body of water
Outwash sand and gravel (Qsg)
Quaternary glacial till (QM)
Eoc. Metchosin Fmtn (EMe)
Jur.-Cret. Leech River Complex (JKLe)
C
Positive flower structure schematic
Composite cross-section from Sites 2, 4, and 5.
S
N
F5-2
F2-7, F3-1
Y: ~290°
F4-4
0
100
200
300
400
500
600
700
800
Distance across strike (m)
D
S
N
Southern boundary
Leech River valley
F1-5
Boulders up against
uphill-facing scarp
F1-1
F1-2
F1-3
F1-4
0
100
200
300
Distance across strike (m)
E
Ice Flow
N
Duplexing and lensing
1 km
Humpback Reservoir
Rhombohedral Basin

Figure 14. (A) Fault plane solutions of crustal earthquakes, observed and inferred Quaternary fault segments, and detailed field sites. (B) Poles to slickenlined fault planes, strike-distribution of fault planes. (C) Schematic cross-section across brittle fault zone from Sites 2, 4, and 5, where scarps suggest positive flower structure. (D) Negative flower structure schematic based on scarps and ERT from Site 1. (E) Quaternary strands and potentially tectonic geomorphic features (sag ponds, pull-apart basins) along the 25-km study area.

Another common feature of faulting in unconsolidated sediments is the deposition of coseismic colluvial wedges against the face of fault scarps (e.g. Marshall et al., 2000; Johnson et al., 2004b; Authemayou et al., 2012; Aron et al., 2014; Personius et al., 2014; Nelson et al., 2017). Though somewhat ambiguous, I propose that the burial of a loamy charcoal-bearing sand, interpreted as a paleosol, by a northward-tapering wedge of colluvium above the gouge-bearing western exposure of **F2-2** may also be the result of coseismic displacement. The colluvial deposit is perched near the top of the bedrock quarry, with no obvious source area for landslide or other colluvial deposits, and boulders assumed to be from the excavation of the quarry (Site 2-A) lie atop the vegetated surface of the colluvial wedge. Motion on **F2-2** and its conjugates postdating deposition of the sediment wedges is further supported by the consistency between north-side-down steps in bedrock topography above *en échelon* north-dipping normal faults. The observation that only Wedge 1, which overlies a fault strand parallel to the other two wedges, contains a boulder and silt deposit suggests that it may have a different geomorphic evolution than the other two wedges, despite their close proximity. Further, the vertical contact of the silt with the adjacent slickenlined plane of Metchosin Formation makes it seem unlikely that the bedrock scarp was preserved or formed through glaciation of the area.

Resistivity and GPR profiles along three adjacent glaciofluvial terraces east of the Sooke River (*Qt3, Qt4, Qt6*) reveal an ~40-m-wide complex inferred flower structure of subvertical and steeply north-dipping fault planes, consistent with along strike bedrock observations in the immediate footwall of the lithologic Leech River fault. Scattered outcrop on the terrace surface and the road cut at Site 2-B reveal that bedrock extends to within ~1 m of the surface of *Qt3* except for in the ~8-m-wide recess above **F2-6**. The thin sedimentary cover implies that the majority of resistivity structure beneath *Qt3* must be the result of structure in the Metchosin Igneous Complex, providing no evidence for relatively recent fault rupture. My interpretation of

the ERT profile along *Qt4* is similar – it is doubtful that the glaciofluvial sediments extend to the depth of the profile (~15 m), and bedrock is observed within ~3 m of the terrace surface in two locations on its western riser. Laterally discontinuous resistivity domains, particularly resistive anomalies between 5 – 10 m depth in the ERT profile (R2, Fig. 8E) may represent either bedrock structures, or sediment infilling of irregular bedrock topography regardless of whether or not faults have ruptured since deposition. However, resistivity profiles along both *Qt3* and *Qt4* do exhibit steeply north-dipping anomalies coincident with a north-side-up topographic lineament along strike from **F2-6**, which is observed to dip ~65° to the north-northeast.

On the lowest terrace, *Qt6*, which lies ~4 m above the modern Sooke River, resistivity tomography also shows steeply north-dipping anomalies extending downwards from the projection of **F2-6** to within 1 m of the terrace surface, implying that fault strands may intersect the glaciofluvial and fluvial sediments. In particular, high-resolution shallow resistivity tomography along *Qt6* (Fig. 8F) images subvertical resistivity anomalies extending to within 1 m of the ground surface, where colocated GPR imagery is used to infer the bedrock basement at a depth of ~3 – 8 m (Fig. 8G). Variations in sediment composition could also account for laterally variable resistivity structure in the ERT profiles across *Qt6*. It is the consistency of north-dipping resistivity structure, which extends from the surface to >9 m depth, with the observed north-dipping fault zone along strike at Site 2-B, that leads to the interpretation of the resistivity anomalies as fault-related features. Although there is little topographic evidence for recent activity across the terraces at Site 2, I speculate that flooding of the Sooke River could erode scarps relatively quickly in this environment, and settlement associated with placer mining operations may have also disturbed the surface. Conclusive evidence for late Quaternary fault activity at Site 2 is lacking, but its position between Sites 1 and 3, where evidence is more compelling, increases the likelihood that the somewhat ambigious sedimentary features of the terraces are related to the brittle fault zone they overly.

In contrast to the relatively smooth terraces at Site 2, three lineaments ~2 – 3 m high and up to 40 m wide trend parallel to the Y axis of the Leech River fault zone along the terrace north of the Goldstream River at Site 4 (Figs. 11A, 11G, Appendix E). These linear ridges exhibit an apparent

south-side-up offset of the terrace surface, and the Goldstream River drops down several metres as it flows to the north across the projection of the most prominent lineament, possibly due to a tectonically controlled knickpoint (e.g. Kirby and Whipple, 2012). The presence of brittle faulting in friable schist of the Leech River Complex ~2 km along strike to the west, and the consistency of kinematic indicators with regional seismicity (Fig. 13A), suggest that the active fault zone cuts through the Goldstream River valley. Minor centimetre-scale irregular dykelets or 'liquefaction tubes' (e.g. Nelson et al., 2017) of silt to fine sand cut through delta foreset beds nearby (Fig. 11E).

More extensive liquefaction and disturbance of sediments is observed within ~200 m south of the lithologic Leech River fault near the frontal slopes of the Colwood Delta, at Site 5-C. In addition to numerous flame structures and silty diapirs, silt and sand beds are offset by one metre-scale thrust fault and several (3 – 5) centimetre-scale brittle thrust offsets. These features may be the result of loading from mass failure off the delta slope, which is supported by an escarpment ~250 m to the northeast (Appendix F). However, the site also lies within 900 m along strike of the ~500-m-wide zone of subvertical discontinuities imaged by Bednarski (2016) extending through thick pre-Wisconsinan Quaternary sediments to within 3 – 4 m of the surface of Ocean Boulevard. Bednarski (2016) interpreted the lack of vertical discontinuities in the relatively low density upper layer as precluding postglacial rupture. However, Ocean Boulevard is capped by Holocene sands (Monahan et al., 2000), and the thickness of any postglacial outwash sediments is unclear. Nearby resistivity and GPR imagery (Fig. 12D, Appendix F) also bear some similarity to the structure imaged by Bednarski (2016), which is very similar to that observed in geophysical surveys at Site 2, resembling a flower structure with a minor component of north-side-up displacement in the immediate footwall of the lithologic Leech River fault.

Many of the features described above are not unique to recent tectonism, and may alternatively be attributed to sedimentary, colluvial, or glaciotectonic processes. For example, it is possible that the apparent thrust displacement of the lower contact of lodgement till at Site 3 (**F3-5**) could be the result of proglacial thrusting, where material, usually glacial till, is pushed forward with the advance of the glacier, generally resulting in ramp-flat décollement geometry (Pedersen, 2014). Alternatively, pressure from overriding ice may have caused till to be injected downwards

into a pre-existing bedrock fracture, but this cannot easily account for offset of the contact. Because the thrusting occurs at an oblique angle to the dominant ice-flow direction, bedrock underlying the thrusted sediments is also offset, and the dip of the fault (~55°) is relatively steep, I consider it most likely that this fault (**F3-5**) has been offset tectonically since deposition of the till.

Similarly, faulted and liquefied sediments at Sites 4 and 5 may be the result of sedimentary loading, but the proximity to observed bedrock faults suggests that they share an origin. However, when considered collectively, the geomorphic, geophysical, and sedimentary evidence illustrates an active strike-slip fault zone, which is further supported by the consistency between relatively young right-lateral kinematic indicators and fault plane solutions of crustal earthquakes to the north (Fig. 13A; Balfour et al., 2011) that have been associated with the Leech River fault zone (Li et al., *in review*). Particularly at Site 1, where paleoseismic trenching has revealed uphill-facing offset of Leech River Complex and overlying late Quaternary units, there is little doubt that coseismic displacement has occurred on the Leech River fault zone since the last glaciation (~15 ka).

Late Quaternary surface rupture along the eastern Leech River fault zone indicates a previously unrecognized shallow seismic source on southern Vancouver Island, within ~5 km of the city of Victoria, and cutting directly through the communities of Langford and Colwood (Fig. 13A). Morell et al. (2017) used magnitude-length scaling relationships to infer that the Leech River fault zone is capable of producing surface-rupturing earthquakes of at least $M_w = 6$, posing a significant seismic risk to surrounding communities and infrastructure. Given that the eastern fault appears to merge into an ~6 – 10-km-wide fault zone offshore associated with the Darrington-Devil's Mountain fault zone (Barrie and Greene, 2015), the continuous fault may be much longer, and thereby capable of producing even larger earthquakes. I also consider it likely that other crustal faults on southern Vancouver Island, including the western half of the Leech River fault, may experience Quaternary activity.

5.2 Fault zone geometry

The 25-km-long eastern Leech River fault zone consists of multiple *en échelon* and conjugate brittle fault strands 10s to 100s of metres long within complex zones that can be traced along strike for up to 5 km. The complexity, width, and steepness of the fault zone are indicative of a strike-slip or oblique-slip structure (Jensen et al., 2011; Barth et al., 2012), and the observed fault geometry can be described adequately using characteristic strike-slip patterns such as Riedel shear geometry, flower structure, and extensional/compressional step-overs (e.g. Davis et al., 2000; Swanson, 2006). The geometry and kinematics of relatively recent faulting vary along strike within the study area, possibly due to deviations and step-overs in the trend of the fault zone, which often cause localized extension and compression along strike-slip faults. Similarly, variations in the dip-direction of steep faults can cause associated scarps to display alternate facing directions along strike.

I consistently observe complex, subvertical to steeply dipping, wide (100 – 750 m) zones of brittle fault strands that I interpret as flower structure. Mesoscale fault geometry within the Metchosin Formation and overlying Quaternary units often consists of sets of subvertical and steeply north-dipping inferred fault planes, whereas the two instances of exposed faulting in the Leech River Complex (Sites 1, 4) include steeply south-dipping planes, consistent with their position on the north side of a flower structure. Resistivity and GPR imagery at Sites 2-B and 5 reveal an inferred positive, north-side-up flower structure in Metchosin Formation basalt, consistent with the prominent north-side-up scarp between Sites 2 and 3 (**F2-7**, **F3-1**, Fig. 13C). The south-side-up offset of the Leech River Complex and fluvial sediments inferred along the Goldstream River (Site 4) similarly implies some component of compression, consistent with the abundant compressional faulting in Metchosin Formation to the south, and the presence of the 5-km-long ridge at Site 4.

At Site 1, geophysical and topographic data potentially illustrate a negative flower structure, with faulting in the Metchosin Formation and overlying Quaternary deposits dipping steeply to the north and accommodating some component of north-side-down, extensional

displacement (**F1-5**, Fig. 13D, Appendix B), while the most prominent, north-side-up scarp (**F1-1**) is formed by a steeply south-dipping fault near the surface. However, there is some degree of uncertainty in the dip direction of **F1-1**, which dips steeply to the south at the surface but is imaged by ERT dipping northward at depth, making it difficult to assess whether the north-side-up offset truly does represent extension. Resistivity tomography also reveals at least three secondary north-dipping north-side-up faults in the Leech River Complex, which would indicate compression. It is also possible that north-side-down tectonic offset contributes to the high relief of the Metchosin Formation ice-marginal southern boundary of the Leech River valley. Although the width and steepness of the fault zone at Site 1 are characteristic of a strike-slip fault, only dip-slip motion is inferred from offset across the topographic scarps, making the kinematics of Quaternary faulting difficult to interpret. Another possibility is that these fault strands form as horsetail splays near the end of the recently ruptured fault zone (e.g. Swanson, 2006).

Most exposures of the brittle Leech River fault zone are observed in the Metchosin Formation, and dip steeply to the north towards the lithologic Leech River fault. In contrast, the two instances of faulting observed in the Leech River Complex, at Sites 1 and 4, contain steeply south-dipping planes. The opposing dips of fault planes towards the lithologic Leech River fault suggests that faulting may splay outwards from a single strike-slip fault at depth, possibly colocated with the lithologic Leech River fault. If this is the case, it would imply that the Leech River fault has a listric geometry, dipping moderately at depth and splaying upwards in steep to subvertical strands that manifest at the surface as flower structure. Compressional flower structure is a common feature of crustal faults regionally, and has been imaged by seismic reflection profiling in the Juan de Fuca Strait cutting Metchosin Formation and overlying sediments across extensions of both the Southern Whidbey Island fault (Johnson et al., 1996), and the Darrington-Devil's Mountain fault zone (Hayward et al., 2006).

5.3 Fault kinematics

Several kinematic, geomorphic, and geometric features of the eastern Leech River fault zone lead to its interpretation as an active right-lateral strike-slip fault, which is supported by

recorded right-lateral crustal seismicity that parallels the fault zone to the north (Fig. 13A, Balfour et al., 2011). Dominant fault plane orientations interpreted within a Riedel shear framework include: 1) steeply dipping to vertical along the main trend of the fault (Y: 290°), 2) oriented 10° – 30° clockwise relative to the main fault trend (R), and 3) at high angles to the main fault trend, as in conjugate shears (R') (Fig. 13B). The high proportion of faults oriented 10° – 30° clockwise from the main fault strike (Y axis) is consistent with the expected abundance of R shears in a right-lateral fault system. More specific kinematic data are provided at Site 3, where a consistent kinematic regime from slip-sense indicator measurements (n=11), including those from Quaternary fault planes, predicts right-lateral slip on a best-fit fault plane solution of 291°/57°N.

At Site 2-A, fault kinematics from slickenlined slip-sense indicators, the orientation of dominant fault strands (**F2-2**) 10 – 20° clockwise relative to the main fault strike, and localized extension between right-stepping *en échelon* strands, are all consistent with a right-lateral Riedel shear framework. Fault strands that are interpreted as through-going and relatively recent at Site 2-B (**F2-6, -7**) are also oriented slightly clockwise relative to the main strike of the fault zone, and are interpreted as R shears. The predominantly steeply north-dipping thrust offset of Holocene fluvial sediments inferred from electrical resistivity and GPR profiles may be attributable to compression between left-stepping right-lateral fault strands. The complex compressional fault zone striking ~10 – 20° counterclockwise from the main fault trend (Y) (**F2-5**), may act as a compressional P linkage within a right-lateral Riedel shear framework.

The dominant compressional faulting at Site 4 may also be the result of the left-stepping geometry of the fault strands within a right-lateral strike-slip system, from the northern flank of the Metchosin Formation ridge to the Leech River Complex along the Goldstream River. Kinematic axes from Site 4 indicate predominantly north-northwest – south-southeast-directed compression, consistent with both the younger generation of faulting at Site 3 and the regional stress field from fault plane solution inversion of recorded right-lateral crustal seismicity (Balfour et al., 2011).

The revelation that the Leech River fault zone has been active in the latest Quaternary calls for a reassessment of the geomorphology along its trace. For example, several lakes are aligned along the Leech River fault zone, some of which may be tectonically controlled either as sag ponds, a common feature in strike-slip fault zones, or structurally controlled basins. These include Jack Lake, on the east side of Site 3, as well as several lakes on the outwash plain of the Colwood Delta such as the Humpback Reservoir, Langford Lake, and Glen Lake, which have linear margins along strike of observed brittle fault strands. While many small lakes on the Colwood Delta are likely correctly identified as kettle lakes, the alignment of fault scarps along strike of Glen Lake's boundaries has led to the speculation that they may be tectonically controlled (Bednarski, 2016). Similarly, the Humpback Reservoir, which is bound by steep outcrops of Metchosin Formation, resembles a rhombohedral pull-apart basin in a right-handed step-over between two strands of a right-lateral strike-slip fault system (Fig. 13E).

Widely varying fault plane mineralogy, from euhedral epidote to oxidized clay gouge, suggests that the observed brittle fault zone has experienced slip at a range of depths. While ductile slip-sense indicators along the lithologic Leech River fault indicate left-lateral strike-slip motion, modern seismicity that has been associated with the Leech River fault zone (Li et al., *in review*) indicates right lateral motion. The presence of multiple clusters of kinematic axes from slip-sense indicator measurements from the brittle Leech River fault zone also implies that it has been active through different crustal stress fields, and has therefore experienced changes in kinematics. Cross cutting relationships between fault strands of inconsistent geometry further suggests changes in the stress field orientation and associated slip sense over the span of the fault's activity. For example, the brittle fault zone exposed at Site 2-B contains numerous faults with widely varying mineralogy and kinematics, inferred to represent multiple phases of deformation. Dominant kinematic axes reveal a system of left-lateral transtension, while upward-branching clay altered fault zones (**F2-5**) are compressional with minor dextral shear. Apparent thrust displacement revealed by geophysical imagery of adjacent Holocene terraces leads to the inference that the dextral compressional kinematic regime is relatively younger than the sinistral transtension.

Crosscutting relationships and directly observed Quaternary offset at Site 3 similarly allow for the determination of an older left-lateral transtensional and younger (Quaternary) right-lateral compressional kinematic regime. Despite the consistency of kinematic indicators from relatively young faulting with regional stress and right-lateral sense of slip, the fault strand geometry at Site 3 fits well within a left-lateral Riedel shear framework, with longer *en échelon* faults (**F3-1, -2**) linked by compressional faults (**F3-3**, **-4**) that are oriented clockwise relative to the main fault trend, as in P linkages between more continuous R strands of a left-lateral fault system. The crosscutting relationships and late activity on these clockwise-oriented strands could be the result of progression of the fault zone through time, rather than a change in kinematics (e.g. Swanson, 2006). However, components of right-lateral motion on northeast-dipping thrust faults and multiple slickenlines on fault surfaces supports the strain inversion result of a relatively poorly developed right-lateral fault system overprinting the well-developed left-lateral fault, from which it likely inherited its geometry. The shear zones exposed at Sites 2-B (**F2-6**) and 3-A (**F3-2**) exhibit well-developed scaly fabric, a texture that is generally observed at depth within large-scale, mature structures (Vannucchi et al., 2003; Bradbury et al., 2011; Kirkpatrick et al., 2014). Another indication that the contemporary right-lateral fault zone has some inherited geometry from an earlier left-lateral fault system is provided by left-lateral slip-sense indicators within ductile deformation exposed along the Leech River and Old Wolf Creek near Site 2.

The seismic cycle of the Cascadia megathrust may also contribute to apparently inconsistent kinematics along the Leech River fault zone, particularly with respect to the extensional faulting observed at Site 1. Paleoseismic studies have shown that many crustal earthquakes in western Washington occur during the interseismic cycle of the Cascadia megathrust, but that they likely also occur in response to megathrust rupture (Sherrod and Gomberg, 2014), which can cause crustal faults to rupture through either static stress changes or dynamic pulses (Loveless et al., 2010; Nissen et al., 2016). Extensional seismicity in the forearc during or immediately following megathrust rupture has been widely observed in both Japan (Kato et al., 2011) and Chile (Loveless et al., 2010; Aron et al., 2014). Graben-like structures have been observed along several crustal faults in western Washington (Dragovich and DeOme, 2006),

including in paleoseismic trenches across the Darrington-Devil's Mountain fault zone where Quaternary sediments exhibit north-side-up offset along steeply south-dipping fault planes similar to those excavated at Site 1 (Personius et al., 2014). Although coseismic and postseismic crustal faulting in the Cascadia forearc is not well documented, Personius et al. (2014) suggested that the apparent normal offset observed along the right-lateral Darrington-Devil's Mountain fault zone may be the result of coseismic stress drop that occurs during rupture of the megathrust.

Although the geometry, kinematics, and relative timing of fault activity are complex, I infer that the active right-lateral eastern Leech River fault zone overprints and exploits weaknesses of the ancient left-lateral brittle strike-slip fault that has been more commonly documented.

5.4 Regional Implications

The Leech River fault zone forms an extension of the active crustal fault network that accommodates permanent deformation in the northern Cascadia forearc. The density of crustal seismicity (Mulder, 1995) and active faults (Wells et al., 2017) around the flanks of the Olympic Mountains suggest that the continued uplift of the Olympic core (Brandon et al., 1998) affects the dynamics of forearc deformation.

I use fault kinematics and seismicity data to infer that the Leech River fault zone experiences right-lateral kinematics in the Holocene, which has also been documented on the east-west-trending Darrington-Devil's Mountain fault zone (Personius et al., 2014) and the Lake Creek–Boundary Creek fault (Nelson et al., 2017) north of the Olympic Mountains (Fig. 1). Quaternary faults south of the Olympic Mountains, such as the Saddle Mountain and Hood Canal faults experience predominantly left-lateral transpression (Blakely et al., 2009; Nelson et al., 2017). This reversal of slip-sense on crustal faults across the Olympic Mountains results in relative westward motion of the Olympic core (Nelson et al., 2017). In contrast, during accretion in the Eocene and early Miocene, it is thought that eastward arching of the Crescent-Siletz terrane was accommodated by left-lateral slip on the Leech River and other surrounding faults (Fairchild, 1979; Groome et al., 2003; Nelson et al., 2017), implying that the current mechanics of forearc

deformation in the upper crust surrounding the Olympic Mountains are fundamentally different than the mechanics that accommodated bending during accretionary deformation.

In the Miocene, the initiation of subduction east of the Crescent-Siletz terrane resulted in subduction into the concave margin formed by the Eocene eastward arching of the Crescent-Siletz terrane. The cause of the initial bending of the margin is unknown, but plate reconstructions and observed magmatism have been used to infer subduction of the active Farallon-Kula ridge near the latitude of the present-day Olympics at ~50 Ma (e.g. Cowan, 2003; McCrory and Wilson, 2013; Wells et al., 2014; Phillips et al., 2017). Crustal indentors are a common driver of progressive oroclines (Del Greco et al., 2016), and I speculate that the Farallon-Kula ridge, or the thick oceanic plateau of the Crescent-Siletz terrane may have acted as an indentor to initiate bending of the plate margin, which was accommodated in part by left-lateral slip on the Leech River fault.

Post-Miocene slip-sense reversal on the east-trending faults north of the Olympic Mountains is likely related to the transition from accretionary to forearc deformation processes and uplift of the Olympic Mountains, which began in the early Miocene, and has remained relatively constant since ~18 Ma (Brandon et al., 1998). Now, in absence of an indentor, the core of the Olympics experiences extrusion relative to surrounding crust, corresponding to right-lateral motion on Leech River Fault zone and surrounding crustal faults, due to ongoing bending that continues to be driven by margin-parallel compression.

6 Conclusions

This study was undertaken in order to elucidate the geometry, kinematics, and extent of Quaternary activity along the eastern Leech River fault zone, to offer constraint on the nature of forearc deformation north of the Olympic Mountains in southwest BC. In addition to characterizing the geomorphic and structural nature of the eastern Leech River fault zone, this thesis presents the following conclusions:

1. The eastern Leech River fault zone comprises a complex array of *en échelon* and conjugate mesoscale fault strands that ranges from 200 m – 3 km wide. Fault strand geometry exhibits many characteristics, such as extensional and compressional duplexes, step-overs, and flower structure, that are indicative of a strike-slip fault. Flower structure consisting of intersecting sets of subvertical and steeply north dipping fault planes is observed in outcrop and imaged by geophysical surveys along the 25 km length of the study area.
2. Brittle fault strands observed at the surface are not colocated with the lithologic terrane-bounding Leech River fault, but are observed in both Leech River Complex north of the lithologic fault contact, and Metchosin Formation to the south.
3. Postglacial seismic rupture is indicated by direct observation of offset late Quaternary deposits along the western 8 km of the study area, and by geophysical, topographic, and sedimentary evidence in Holocene deposits to the east.
4. Brittle fault strands extend east towards previously mapped active faults in the Juan de Fuca Strait, suggesting that the Leech River fault zone forms an extension of the crustal fault network in western Washington through merging with the Darrington-Devil's Mountain fault zone, and possibly the Southern Whidbey Island fault beneath the Colwood Delta or in the Juan de Fuca Strait.
5. Fault kinematics and strand geometry indicate right-lateral activity post-dating earlier left-lateral brittle activity and continuing into the late Quaternary. Right-lateral Quaternary activity on other left-lateral Eocene faults nearby, and right-lateral seismicity in the upper plate in the vicinity of the Leech River fault support this conclusion.

7 References

Advanced Geosciences Inc., 2007, Earth Imager 2D resistivity and IP inversion software instruction manual: Advanced Geosciences, Inc., 2121 Geoscience Dr., Austin, TX 78726, 127 p.

Alley, N.F., and Chatwin, S.C., 1979, Late Pleistocene history and geomorphology, southwestern Vancouver Island, British Columbia: Canadian Journal of Earth Sciences, v. 16, no. 9, p. 1645–1657.

Allmendinger, R.W., Gephard, J.W., and Marrett, R.A., 1989, Notes on fault slip analysis, *in* Geological Society of America short course on quantitative interpretation of joints and faults, Department of Geological Sciences, Cornell University, Ithaca, New York, p. 56.

Andronicos, C.L., Hollister, L.S., Davidson, C., and Chardon, D., 1999, Kinematics and tectonic significance of transpressive structures within the Coast Plutonic Complex, British Columbia: Journal of Structural Geology, v. 21, no. 2, p. 229–243, doi: 10.1016/S0191-8141(98)00117-5.

Aron, F., Cembrano, J., Astudillo, F., Allmendinger, R.W., and Arancibia, G., 2014, Constructing forearc architecture over megathrust seismic cycles: Geological snapshots from the Maule earthquake region, Chile: Bulletin of the Geological Society of America, v. 127, no. 3–4, p. 464–479, doi: 10.1130/B31125.1.

Authemayou, C., Brocard, G., Teyssier, C., Suski, B., Cosenza, B., Morán-Ical, S., González-Véliz, C.W., Aguilar-Hengstenberg, A.M., and Holliger, K., 2012, Quaternary seismo-tectonic activity of the Polochic Fault, Guatemala: Journal of Geophysical Research: Solid Earth, v. 117, no. 7, p. 1–21, doi: 10.1029/2012JB009444.

Balfour, N.J., Cassidy, J.F., Dosso, S.E., and Mazzotti, S., 2011, Mapping crustal stress and strain in southwest British Columbia: Journal of Geophysical Research, v. 116, no. B3, p. B03314, doi: 10.1029/2010JB008003.

Barrie, J. V, and Greene, H.G., 2015, Active faulting in the northern Juan de Fuca Strait : implications for Victoria, British Columbia: Geologic Survey of Canada Current Research 2015-6, p. 10, doi: doi: 10.4095/296564.

Barth, N.C., Toy, V.G., Langridge, R.M., and Norris, R.J., 2012, Scale dependence of oblique plate-boundary partitioning: New insights from LiDAR, central Alpine fault, New Zealand: Lithosphere, v. 4, no. 5, p. 435–448, doi: 10.1130/L201.1.

Beck, M.E., and Engebretson, D.C., 1982, Paleomagnetism of small basalt exposures in the west Puget Sound Area, Washington, and speculations on the accretionary origin of the Olympic Mountains: Journal of Geophysical Research, v. 87, no. B5, p. 3755–3760, doi: 10.1029/JB087iB05p03755.

Beck, M.E., Rojas, C., and Cembrano, J., 1993, On the nature of buttressing in margin-parallel stri ke-slip fault systems: Geology, v. 21, p. 755–758, doi: 10.1130/0091-7613(1993)021<0755:OTNOBI>2.3.CO;2.

Bednarski, J.M., 2016, Preliminary investigations of unconsolidated sediments overlying the Leech River fault zone, southern Vancouver Island, British Columbia: Geological Survey of Canada, p. 29.

Bellier, O., and Sebrier, M., 1995, Is the slip rate on the Great Sumatran Fault accommodated by fore-arc stretching ? Geophysical Research Letters, v. 22, no. 15, p. 1969–1972.

Blaise, B., Clague, J.J., and Mathewes, A.W., 1990, Time of maximum Late Wisconsin glaciation, west coast of Canada: Quaternary Research, v. 34, p. 282–295.

Blakely, R., Sherrod, B., Hughes, J., Anderson, M., Wells, R., and Weaver, C., 2009, Saddle Mountain fault deformation zone, Olympic Peninsula, Washington: Western boundary of the Seattle uplift: Geosphere, v. 5, no. 2, p. 105–125, doi: 10.1130/GES00196.1.

Blakely, R.J., Wells, R., Weaver, C.S., and Johnson, S.Y., 2002, Location, structure, and seismicity of the Seattle fault zone, Washington: Evidence from aeromagnetic anomalies, geologic mapping, and seismic-reflection data: Bulletin of the Geological Society of America, v. 114, no. 2, p. 169–177, doi: 10.1130/0016-7606(2002)114<0169:LSASOT>2.0.CO;2.

Bradbury, K.K., Evans, J.P., Chester, J.S., Chester, F.M., and Kirschner, D.L., 2011, Lithology and

internal structure of the San Andreas fault at depth based on characterization of Phase 3 whole-rock core in the San Andreas Fault Observatory at Depth (SAFOD) borehole: Earth and Planetary Science Letters, v. 310, p. 131–144, doi: 10.1016/j.epsl.2011.07.020.

Brandon, M.T., Roden-Tice, M.K., and Garver, J.I., 1998, Late Cenozoic exhumation of the Cascadia accretionary wedge in the Olympic Mountains, northwest Washington State: Geological Society of America Bulletin, v. 110, no. 8, p. 985–1009, doi: 10.1130/0016-7606(1998)110<0985:LCEOTC>2.3.CO;2.

Carbonel, D., Gutiérrez, F., Linares, R., Roqué, C., Zarroca, M., McCalpin, J., Guerrero, J., and Rodríguez, V., 2013, Differentiating between gravitational and tectonic faults by means of geomorphological mapping, trenching and geophysical surveys. The case of the Zenzano Fault (Iberian Chain, N Spain): Geomorphology, v. 189, p. 93–108, doi: 10.1016/j.geomorph.2013.01.020.

Carpentier, S.F.A., Green, A.G., Doetsch, J., Dorn, C., Kaiser, A.E., Campbell, F., Horstmeyer, H., and Finnemore, M., 2012, Recent deformation of Quaternary sediments as inferred from GPR images and shallow P-wave velocity tomograms: Northwest Canterbury Plains, New Zealand: Journal of Applied Geophysics, v. 81, p. 2–15, doi: 10.1016/j.jappgeo.2011.09.007.

Clague, J.J., and James, T.S., 2002, History and isostatic effects of the last ice sheet in southern British Columbia: Quaternary Science Reviews, v. 21, p. 71–87, doi: 10.1016/S0277-3791(01)00070-1.

Clowes, R.M., Brandon, M.T., Green, A.G., Yorath, C.J., Brown, A.S., Kanasewich, E.R., and Spencer, C.J., 1987, LITHOPROBE—southern Vancouver Island: Cenozoic subduction complex imaged by deep seismic reflections: Reply: Canadian Journal of Earth Sciences, v. 24, p. 31–51, doi: 10.1139/e88-019.

Colpron, M., Nelson, J.A.L., and Murphy, D.C., 2007, Northern Cordilleran terranes and their interactions through time: GSA Today, v. 17, no. 4, p. 4–10, doi: 10.1130/GSAT01704-5A.1.

Cowan, D.S., 2003, Revisiting the Baranof-Leech River hypothesis for early Tertiary coastwise

transport of the Chugach-Prince William terrane: Earth and Planetary Science Letters, doi: 10.1016/S0012-821X(03)00300-5.

Davis, G.H., Bump, A.P., García, P.E., and Ahlgren, S.G., 2000, Conjugate Riedel deformation band shear zones: Journal of Structural Geology, v. 22, no. 2, p. 169–190, doi: 10.1016/S0191-8141(99)00140-6.

Doblas, M., 1998, Slickenside kinematic indicators: Tectonophysics, v. 295, no. 1–2, p. 187–197, doi: 10.1016/S0040-1951(98)00120-6.

Dragovich, J.D., and DeOme, A.J., 2006, Geologic map of the Skagit and Snohomish counties , Washington , with a discussion of the evidence for Holocene activity on the Darrington – Devils Mountain fault zone.:

Dunae, P.A., 2016, The gold will speak for itself : Peter Leech and Leechtown / The history of Leechtown Part I : The VIEE and the discovery of gold on the Sooke and Leech rivers / Those island people / Vancouver Island scoundrels , eccentrics and originals : Tales from the: BC Studies, v. Vancouver, no. 189, p. 160–164.

English, J.M., and Johnston, S.T., 2005, Collisional orogenesis in the northern Canadian Cordillera: Implications for Cordilleran crustal structure, ophiolite emplacement, continental growth, and the terrane hypothesis: Earth and Planetary Science Letters, v. 232, no. 3–4, p. 333–344, doi: 10.1016/j.epsl.2005.01.025.

Ercoli, M., Pauselli, C., Frigeri, A., Forte, E., and Federico, C., 2013, “Geophysical paleoseismology” through high resolution GPR data: A case of shallow faulting imaging in Central Italy: Journal of Applied Geophysics, v. 90, p. 27–40, doi: 10.1016/j.jappgeo.2012.12.001.

Fairchild, L.H., and Cowan, D.S., 1982, Structure, petrology, and tectonic history of the Leech River complex northwest of Victoria, Vancouver Island: Canadian Journal of Earth Sciences, v. 19, p. 1817–1835, doi: 10.1139/e82-161.

Del Greco, K., Johnston, S.T., Gutiérrez-Alonso, G., Shaw, J., and Fernández Lonzano, J., 2016,

Interference folding and orocline implications: A structural study of the Ponga Unit, Cantabrian orocline, northern Spain: Lithosphere , , no. 6, p. 1–12, doi: 10.1130/L576.1.

Groome, W.G., Thorkelson, D.J., Friedman, R.M., Mortensen, J.K., Massey, N.W.D., Marshall, D.D., and Layer, P.W., 2003, Magmatic and tectonic history of the Leech River Complex, Vancouver Island, British Columbia: Evidence for ridge-trench intersection and accretion of the Crescent Terrane: Geological Society of America, v. Special Pa, p. 327–353, doi: 10.1130/0-8137-2371-X.327.

Haugerud, R.A., Harding, D.J., Johnson, S.Y., Harless, J.L., Weaver, C.S., and Sherrod, B.L., 2003, High-resolution lidar topography of the Puget Lowland, Washington - A bonanza for earth science: GSA Today, v. 13, no. 6, p. 4–10, doi: 10.1130/1052-5173(2003)13<0004:HLTOTP>2.0.CO;2.

Hayward, N., Nedimovic, M.R., Cleary, M., and Calvert, A.J., 2006, Structural variation along the Devil's Mountain fault zone, northwestern Washington: Canadian Journal of Earth Sciences, v. 43, no. 4, p. 433–446, doi: 10.1139/E06-002.

James, T., Gowan, E.J., Hutchinson, I., Clague, J.J., Barrie, J.V., and Conway, K.W., 2009, Sea-level change and paleogeographic reconstructions, southern Vancouver Island, British Columbia, Canada: Quaternary Science Reviews, v. 28, no. 13–14, p. 1200–1216, doi: 10.1016/j.quascirev.2008.12.022.

Jensen, E., Cembrano, J., Faulkner, D., Veloso, E., and Arancibia, G., 2011, Development of a self-similar strike-slip duplex system in the Atacama Fault system, Chile: Journal of Structural Geology, v. 33, no. 11, p. 1611–1626, doi: 10.1016/j.jsg.2011.09.002.

Johnson, S.Y., 1984, Evidence for a margin-truncating transcurrent fault (pre-late Eocene) in western Washington.: Geology, v. 12, no. 9, p. 538–541, doi: 10.1130/0091-7613(1984)12<538:EFAMTF>2.0.CO;2.

Johnson, S.Y., Blakely, R.J., Stephenson, W.J., Dadisman, S. V., and Fisher, M.A., 2004a, Active shortening of the Cascadia forearc and implications for seismic hazards of the Puget Lowland:

Tectonics, v. 23, no. 1, p. 1–27, doi: 10.1029/2003TC001507.

Johnson, S.Y., Dadisman, S. V., Childs, J.R., and Stanley, W.D., 1999, Active tectonics of the Seattle fault and central Puget Sound, Washington—Implications for earthquake hazards: Geological Society of America Bulletin, v. 111, no. 7, p. 1042–1053, doi: 10.1130/0016-7606(1999)111<1042:ATOTSF>2.3.CO;2.

Johnson, S.Y., Nelson, A.R., Personius, S.F., Wells, R., Kelsey, H.M., Sherrod, B.L., Okumura, K., Iii, R.K., Witter, R.C., Bradley, L., and Harding, D.J., 2004b, Evidence for Late Holocene earthquakes on the Utsalady Point Fault , northern Puget Lowland , Washington: Seismological Society of America, v. 94, no. 6, p. 2299–2316, doi: 10.1785/0120040050.

Johnson, S.Y., Potter, C.J., Armentrout, J.M., Miller, J.J., Finn, C., and Weaver, C.S., 1996, The Southern Whidbey Island fault: An active structure in the Puget Lowland, Washington: Bulletin of the Geological Society of America, v. 108, no. 3, p. 334–354, doi: 10.1130/0016-7606(1996)108<0334:TSWIFA>2.3.CO;2.

Johnston, S.T., 2008, The Cordilleran ribbon continent of North America: Annual Review of Earth and Planetary Sciences, v. 36, no. 1, p. 495–530, doi: 10.1146/annurev.earth.36.031207.124331.

Kato, A., Sakai, S., and Obara, K., 2011, A normal-faulting seismic sequence triggered by the 2011 off the Pacific coast of Tohoku Earthquake: Wholesale stress regime changes in the upper plate: Earth, Planets and Space, v. 63, no. 7, p. 745–748, doi: 10.5047/eps.2011.06.014.

Kelsey, H.M., Sherrod, B.L., Nelson, A.R., and Brocher, T.M., 2008, Earthquakes generated from bedding plane-parallel reverse faults above an active wedge thrust, Seattle fault zone: Bulletin of the Geological Society of America, v. 120, no. 11–12, p. 1581–1597, doi: 10.1130/B26282.1.

Kirby, E., and Whipple, K.X., 2012, Expression of active tectonics in erosional landscapes: Journal of Structural Geology, v. 44, p. 54–75, doi: 10.1016/j.jsg.2012.07.009.

Kirkpatrick, J.D., Rowe, C.D., Ujiie, K., Moore, J.C., Regalla, C., Remitti, F., Toy, V., Wolfson-Schwehr, M., Kameda, J., Bose, S., and Chester, F.M., 2014, Structure and lithology of the Japan Trench subduction plate boundary fault: Tectonics, v. 34, p. 53–69, doi: 10.1002/2014TC003695.

Lange, D., Cembrano, J., Rietbrock, A., Haberland, C., Dahm, T., and Bataille, K., 2008, First seismic record for intra-arc strike-slip tectonics along the Liquiñe-Ofqui fault zone at the obliquely convergent plate margin of the southern Andes: Tectonophysics, v. 455, no. 1–4, p. 14–24, doi: 10.1016/j.tecto.2008.04.014.

Lee, J.R., and Phillips, E., 2013, Glacitectonics - a key approach to examining ice dynamics, substrate rheology and ice-bed coupling: Proceedings of the Geologists' Association, v. 124, no. 5, p. 731–737, doi: 10.1016/j.pgeola.2013.07.006.

Leonard, L.J., Hyndman, R.D., and Mazzotti, S., 2004, Coseismic subsidence in the 1700 great Cascadia earthquake: Coastal estimates versus elastic dislocation models: Bulletin of the Geological Society of America, v. 116, no. 5/6, p. 655–670, doi: 10.1130/B25369.1.

Li, G., Liu, Y., Regalla, C., and Morell, K., *in review*, Seismicity relocation and fault structure near the Leech River Fault zone, southern Vancouver Island: Journal of Geophysical Research - Solid Earth.

Loveless, J.P., Allmendinger, R.W., Pritchard, M.E., and González, G., 2010, Normal and reverse faulting driven by the subduction zone earthquake cycle in the northern Chilean fore arc: Tectonics, v. 29, no. 2, p. 1–16, doi: 10.1029/2009TC002465.

MacLeod, N.S., Tiffin, D.L., Snavely Jr., P.D., and Currie, R.G., 1977, Geologic interpretation of magnetic and gravity anomalies in the Strait of Juan de Fuca, U.S.–Canada: Canadian Journal of Earth Sciences, v. 14, p. 223–238, doi: 10.1139/e77-024.

Marrett, R., and Allmendinger, R.W., 1990, Kinematic analysis of fault-slip data: Journal of Structural Geology, v. 12, no. 8, p. 973–986, doi: 10.1016/0191-8141(90)90093-E.

Marshall, J.S., Fisher, D.M., and Gardner, T.W., 2000, Central Costa Rica deformed belt: Kinematics of diffuse faulting across the western Panama block: Tectonics, v. 19, no. 3, p. 468–492, doi: 10.1029/1999TC001136.

Mazzotti, S., Dragert, H., Henton, J.A., Schmidt, M., Hyndman, R.D., James, T.S., Lu, Y., and Craymer, M., 2003, Current tectonics of northern Cascadia from a decade of GPS measurements: Journal of Geophysical Research, v. 108, no. B12, doi: 10.1029/2003JB002653.

Mazzotti, S., Dragert, H., Hyndman, R.D., Miller, M.M., and Henton, J. a., 2002, GPS deformation in a region of high crustal seismicity: N. Cascadia forearc: Earth and Planetary Science Letters, v. 198, no. 1–2, p. 41–48, doi: 10.1016/S0012-821X(02)00520-4.

McCaffrey, R., 1992, Oblique plate convergence, slip vectors, and forearc deformation: Journal of Geophysical Research, v. 97, no. B6, p. 8905, doi: 10.1029/92JB00483.

McCaffrey, R., King, R.W., Payne, S.J., and Lancaster, M., 2013, Active tectonics of northwestern U.S. inferred from GPS-derived surface velocities: Journal of Geophysical Research: Solid Earth, v. 118, no. 2, p. 709–723, doi: 10.1029/2012JB009473.

McCaffrey, R., Qamar, A.I., King, R.W., Wells, R., Khazaradze, G., Williams, C.A., Stevens, C.W., Vollick, J.J., and Zwick, P.C., 2007, Fault locking, block rotation and crustal deformation in the Pacific Northwest: Geophysical Journal International, v. 169, p. 1315–1340, doi: 10.1111/j.1365-246X.2007.03371.x.

McCalpin, J.P., 2009, Paleoseismology:

McClymont, A.F., Green, A.G., Kaiser, A., Horstmeyer, H., and Langridge, R., 2010, Shallow fault segmentation of the Alpine fault zone, New Zealand revealed from 2- and 3-D GPR surveying: Journal of Applied Geophysics, v. 70, no. 4, p. 343–354, doi: 10.1016/j.jappgeo.2009.08.003.

McCrory, P.A., and Wilson, D.S., 2013, A kinematic model for the formation of the Siletz-Crescent forearc terrane by capture of coherent fragments of the Farallon and Resurrection plates:

Tectonics, v. 32, no. 3, p. 718–736, doi: 10.1002/tect.20045.

Monahan, P., Levson, V., Henderson, P., and Sy, A., 2000, Relative liquefaction and amplification of ground motion hazard maps of Greater Victoria.:

Monger, J.W.H., Price, R.A., and Tempelman-Kluit, D.J., 1982, Tectonic accretion and the origin of the two major metamorphic and plutonic welts in the Canadian Cordillera.: Geology, v. 10, no. 2, p. 70–75, doi: 10.1130/0091-7613(1982)10<70:TAATOO>2.0.CO;2.

Montero, W.P., Lewis, J.C., Marshall, J.S., Kruse, S., and Wetmore, P., 2013, Neotectonic faulting and forearc sliver motion along the Atirro–Río Sucio fault system, Costa Rica, Central America: Geological Society of America Bulletin, v. 125, no. 5–6, p. 857–876, doi: 10.1130/B30471.1.

Morell, K.D., Regalla, C., Leonard, L.J., Amos, C., and Levson, V., 2017, Quaternary rupture of a crustal fault beneath Victoria, British Columbia, Canada: GSA Today, v. 27, no. 3–4, p. 4–10, doi: 10.1130/GSATG291A.1.

Mosher, D.C., and Hewitt, A.T., 2004, Late Quaternary deglaciation and sea-level history of eastern Juan de Fuca Strait, Cascadia: Quaternary International, v. 121, no. 1, p. 23–39, doi: 10.1016/j.quaint.2004.01.021.

Muller, J.E., 1977, Evolution of the Pacific Margin, Vancouver Island, and adjacent regions: Canadian Journal of Earth Sciences, v. 14, no. 9, p. 2062–2085, doi: 10.1139/e77-176.

Nelson, A.R., Personius, S.F., Wells, R.E., Bradley, L.A., Buck, J., Schermer, E.R., and Reitman, N., 2017, Holocene earthquakes of magnitude 7 during westward escape of the Olympic Mountains, Washington: Bulletin of the Seismological Society of America, v. 107, no. 5, p. 2394–2415, doi: 10.1785/0120160323.

Nissen, E., Elliott, J.R., Sloan, R.A., Craig, T.J., Funning, G.J., Hutko, A., Parsons, B.E., and Wright, T.J., 2016, Limitations of rupture forecasting exposed by instantaneously triggered earthquake doublet: Nature Geoscience, v. 9, no. 4, p. 330–336, doi: 10.1038/ngeo2653.

Pedersen, S.A.S., 2014, Architecture of glaciotectonic complexes: Geosciences, v. 4, p. 269–296, doi: 10.3390/geosciences4040269.

Personius, S.F., Briggs, R.W., Nelson, A.R., Schermer, E.R., Maharrey, J.Z., Sherrod, B.L., Spaulding, S. a, Bradley, L., Street, H., Vernon, M., and Trench, W., 2014, Holocene earthquakes and right-lateral slip on the left-lateral Darrington – Devils Mountain fault zone , northern Puget Sound , Washington: Geosphere, v. 10, no. 6, p. 1482–1500, doi: 10.1130/GES01067.1.

Petit, J.P., 1987, Criteria for the sense of movement on fault surfaces in brittle rocks: Journal of Structural Geology, v. 9, no. 5, p. 597–608.

Phillips, B.A., Kerr, A.C., Mullen, E.K., and Weis, D., 2017, Oceanic mafic magmatism in the Siletz terrane, NW North America: Fragments of an Eocene oceanic plateau? Lithos, v. 274–275, p. 291–303, doi: 10.1016/j.lithos.2017.01.005.

Reynolds, J.M., 2011, An Introduction to Applied and Environmental Geophysics.: Wiley-Blackwell, West Sussex, UK.

Sherrod, B.L., Blakely, R.J., Weaver, C.S., Kelsey, H.M., Barnett, E., Liberty, L., Meagher, K.L., and Pape, K., 2008, Finding concealed active faults: Extending the southern Whidbey Island fault across the Puget Lowland, Washington: Journal of Geophysical Research, v. 113, no. B5, p. B05313, doi: 10.1029/2007JB005060.

Sherrod, B.L., Brocher, T.M., Weaver, C.S., Bucknam, R.C., Kelsey, H.M., and Haugerud, R., 2004, Holocene fault scarps near Tacoma, Washington, USA: Geology, v. 321, no. 9, p. 9–12, doi: 10.1130/G19914.1.

Sherrod, B., and Gomberg, J., 2014, Crustal earthquake triggering by pre-historic great earthquakes on subduction zone thrusts: Journal of Geophysical Research: Solid Earth, , no. 119, p. 1273–1294, doi: 10.1002/2013JB010597.Received.

Shugar, D.H., Walker, I.J., Lian, O.B., Eamer, J.B.R., Neudorf, C., McLaren, D., and Fedje, D., 2014, Post-glacial sea-level change along the Pacific coast of North America: Quaternary Science

Reviews, v. 97, p. 170–192, doi: 10.1016/j.quascirev.2014.05.022.

Sperner, B., and Zweigel, P., 2010, Tectonophysics A plea for more caution in fault – slip analysis: Tectonophysics, v. 482, no. 1–4, p. 29–41, doi: 10.1016/j.tecto.2009.07.019.

Suski, B., Brocard, G., Authemayou, C., Muralles, B.C., Teyssier, C., and Holliger, K., 2010, Localization and characterization of an active fault in an urbanized area in central Guatemala by means of geoelectrical imaging: Tectonophysics, v. 480, no. 1–4, p. 88–98, doi: 10.1016/j.tecto.2009.09.028.

Swanson, M.T., 2006, Late Paleozoic strike-slip faults and related vein arrays of Cape Elizabeth, Maine: Journal of Structural Geology, v. 28, no. 3, p. 456–473, doi: 10.1016/j.jsg.2005.12.009.

Timpa, S., Gillis, K.M., and Canil, D., 2005, Accretion-related metamorphism of the Metchosin Igneous Complex, southern Vancouver Island, British Columbia: Canadian Journal of Earth Sciences, v. 42, no. 8, p. 1467–1479, doi: 10.1139/e05-043.

Trehu, A.M., Asudeh, I., Brocher, T.M., Luetgert, J.H., Mooney, W.D., Nabelek, J.L., and Nakamura, Y., 1994, Crustal architecture of the cascadia forearc: Science, v. 266, no. 5183, p. 237–243, doi: 10.1126/science.266.5183.237.

Vannucchi, P., Maltman, A., Bettelli, G., and Clennell, B., 2003, On the nature of scaly fabric and scaly clay: Journal of Structural Geology, v. 25, no. 5, p. 673–688, doi: 10.1016/S0191-8141(02)00066-4.

Wang, K., 1996, Simplified analysis of horizontal stresses in a buttressed forearc sliver at an oblique subduction zone: Geophysical Research Letters, v. 23, no. 16, p. 2021–2024.

Wang, K., 2000, Stress-strain “paradox”, plate coupling, and forearc seismicity at the Cascadia and Nankai subduction zones: Tectonophysics, v. 319, no. 4, p. 321–338, doi: 10.1016/S0040-1951(99)00301-7.

Wells, R., Blakely, R.J., Wech, A.G., and Mccrory, P.A., 2017, Cascadia subduction tremor muted by crustal faults: v. 45, no. 6, p. 4–7, doi: 10.1130/G38835.1.

Wells, R., Bukry, D., Friedman, R., Pyle, D., Duncan, R., Haeussler, P., and Wooden, J., 2014, Geologic history of Siletzia, a large igneous province in the Oregon and Washington Coast Range: Correlation to the geomagnetic polarity time scale and implications for a long-lived Yellowstone hotspot: Geosphere, v. 10, no. 4, p. 692–719, doi: 10.1130/GES01018.1.

Wells, R., and Heller, P.L., 1988, The relative contribution of accretion, shear, and extension to Cenozoic tectonic rotation in the Pacific Northwest: Geological Society of America Bulletin, v. 100, p. 325–338.

Wells, R., and Simpson, R.W., 2001, Northward migration of the Cascadia forearc in the northwestern U.S. and implications for subduction deformation: Earth Planets Space, v. 53, p. 275–283.

ID	Strike	Dip	Striae trend	Striae plunge	Slip sense	T trend	T plunge	P trend	P plunge	Latitude	Longitude	Date	Quality*	Slip sense criteria**	Notes***	Age sense?****
1	300	80	30	80	TL	210	55	30	35	48.49329419	-123.714775	23-6-2016	B	Dominant jointing - R shears	Gently undulating smoothed ep-chl plane	Old
2	308	88	38	88	TL	218	47	38	43	48.49329419	-123.714775	23-6-2016	B	Dominant jointing - R shears	Planar chl-Ca-bt sub-mm coating	Old
3	274	74	314.3088	66.0944	TR	207.85	57.2832	349.82	26.8427	48.49329419	-123.714775	23-6-2016	B	R shears	chl coating	Old
4	278	68	338.4289	65.0835	TR	208.34	64.9824	358.87	22.1111	48.49329419	-123.714775	23-6-2016	B	R shears	chl coating v smooth undulating	Old
5	30	82	54.47573	71.26212	NL	105.41	34.8352	318.83	50.1781	48.49329419	-123.714775	23-6-2016	B	Crescentic Ts, R dip direction	Hem-ep-chl-white ppt coating, very smooth face	Old
6	348	45	355.1071	7.053045	NL	317.32	35.932	208.12	24.4045	48.49329419	-123.714775	20-7-2016			slickenlines in chl coating, truncates thrust in back wall of quarry	Young
7	325	48	26.45624	44.29299	NL	41.002	1.18298	306.51	75.226	48.49329419	-123.714775	20-7-2016	C		slickenlines in chl coating	Young
8	300	56	75.91528	45.88693	NR	50.843	6.44623	154.59	64.5671	48.49329419	-123.714775	20-7-2016	B		sparse chl-wt ppt v smooth face, hem-ep.	Young
9	318	50	55.7508	49.74086	NR	51.546	4.88146	193.26	83.7907	48.49329419	-123.714775	20-7-2016	B		dk FeOx smoothed slickenlined surface with thick wt ca-zeo-chalky coating.	Young?
10	314	34	31.99275	33.41488	NL	216.81	11.3508	9.9799	77.3223	48.49329419	-123.714775	20-7-2016	B		dk FeOx smoothed slickenlined surface with thick wt ca-zeo-chalky coating.	Medium?
11	292	48	27.96598	47.84522	NR	24.831	2.92656	159.32	85.8275	48.49329419	-123.714775	20-7-2016	B		dk FeOx smoothed slickenlined surface with thick wt ca-zeo-chalky coating.	Young?
12	322	48	52	48	NR	52	3	232	87	48.49329419	-123.714775	20-7-2016	B		dk FeOx smoothed slickenlined surface with thick wt ca-zeo-chalky coating.	Young?
13	291	89	21	89	NR	21	44	201	46	48.49329419	-123.714775	20-7-2016	B		South bounding of FZ, congruent with bedrock topography	Young
14	124	90	304	40	TL	356.55	27.034	251.45	27.034	48.49329419	-123.714775	20-7-2016	B		South bounding of FZ	Young
15	348	45	355.1071	7.053045	TR	317.32	35.932	208.12	24.4045	48.49329419	-123.714775	20-7-2016	B		mm-scale qtz-chl-ca coating	Young?
16	324	75	108.5834	65.18578	NR	69.794	27.3103	208.67	55.5717	48.49329419	-123.714775	28-9-2016	D		mm-scale qtz-chl-ca coating, crystal growth	Young?
17	300	80	87.05419	72.03614	NR	42.657	33.3566	192.42	52.6953	48.49329419	-123.714775	28-9-2016	B		m-scale chl-cly alt well-striated surface within fracture/damage zone	?
18	38	88	39.15431	29.97985	NL	87.58	19.1875	349.41	22.2108	48.49329419	-123.714775	28-9-2016	B		Xstal growth, undulating discontinuous planes within FZ - rotation of same plane around near-vert anticline	Old
19	25	80	88.25979	78.83105	NL	110.7	34.8149	301.13	54.7362	48.49329419	-123.714775	28-9-2016	A		Thin chl-ox-ca coating, semi-cont, sparse xstal growth	Old
20	274	45	58.73561	30	NR	214.36	8.42106	110.32	58.6003	48.49329419	-123.714775	28-9-2016	B		ca coating, semi-continuous	Young?
21	290	55	37.0883	53.77546	NR	27.151	9.48843	165.67	77.424	48.49329419	-123.714775	28-9-2016	D		through-going chl-cly alt frac gouge, south bound to wedge 5	Young
22	298	90	298	0	TR	253	0	343	0	48.49329419	-123.714775	28-9-2016	C		mm-scale ca-chl-FeOx slicked coating	Old
23	19	63	137.7752	59.83021	NR	119.3	16.8761	260.76	68.8029	48.49329419	-123.714775	28-9-2016	B		Discontinuous planar surface weak striae in ca-cly coating	?
24	12	88	178.0542	81.75539	NR	109.67	42.4636	273.79	46.4253	48.49329419	-123.714775	28-9-2016	C		v subtle straie on clay surfaces locally, merges with 26	Young?
25	44	82	50.66084	39.53371	TR	354.38	33.2646	98.645	20.5905	48.49329419	-123.714775	28-9-2016	B		cm-clast rich gouge, sticky/sandy, 2-10cm BX	Young?
26	28	65	129.6959	64.53646	NR	121.76	19.8514	287.82	69.5954	48.49329419	-123.714775	28-9-2016	B		cm-BX mm-gouge	Young?
27	20	88	26.93928	73.87873	NL	95.059	40.8911	305.93	44.7471	48.49329419	-123.714775	28-9-2016	X		Ca-chl slicks, merges upwards from 27	Young?
28	30	48	127.4492	47.75842	TL	251.3	85.2948	123.54	2.88528	48.49329419	-123.714775	28-9-2016	B		back wall of quarry smooth/glassy qtz-ep	Old
29	310	67	5.559088	62.7653	TR	245.48	64.824	28.723	20.6359	48.49329419	-123.714775	28-9-2016	B		back wall of quarry smooth/glassy qtz-ep	Old
30	298	75	323.9553	58.5243	TR	240.48	51.8204	6.543	24.8378	48.49329419	-123.714775	28-9-2016	B		striae on smooth epidote - implies motion after ep formation in	Old
31	267	60	43.76042	49.87631	TL	129.12	63.4118	16.751	10.7859	48.49329419	-123.714775	28-9-2016	C		chl-cly gougy NE bound of Wedge 2	Old
32	194	85	6.904812	54.68982	NR	312.25	31.0239	72.192	39.6914	48.49329419	-123.714775	3-10-2016	C	R dips		Old
33	200	86	335.0699	84.34544	NR	293.74	40.8697	105.7	48.8502	48.49329419	-123.714775	3-10-2016	B			Old
34	168	85	199.8049	80.57464	NL	250.67	39.4892	86.696	49.3928	48.49329419	-123.714775	3-10-2016	C	en echelon R planes		Old
35	194	82	7.339162	39.53371	NR	319.35	20.5905	63.622	33.2646	48.49329419	-123.714775	3-10-2016	B			Medium?
36	295	68	45.56454	66.65863	NR	31.119	22.6034	190.95	66.0817	48.49329419	-123.714775	3-10-2016				Old
37	200	78	290	78	NL	290	33	110	57	48.49329419	-123.714775	3-10-2016	C		subtle secondary striae same plane as above	Medium?
38	200	78	10.10385	38.95731	NR	324.57	17.3118	67.789	36.2708	48.49329419	-123.714775	3-10-2016	D			Young?
39	193	81	258.9152	80.15784	NL	279.51	35.8796	107.79	53.8345	48.49329419	-123.714775	3-10-2016	C		grungy FP in west wedges	Young

40	292	46	327.729	31.16136	NL	172.32	7.19838	274.45	58.9914	48.49329419	-123.714775	3-10-2016	C		Young?
41	192	86	213.5842	79.23724	NL	272.75	40.1914	112.59	48.0727	48.49329419	-123.714775	3-10-2016	C		Young?
42	300	50	342.5518	38.86642	NL	186.07	0.6191	277.34	63.9269	48.49329419	-123.714775	3-10-2016	D		Young?
43	24	85	42.01813	74.20677	TR	309.84	47.9057	100.53	38.2275	48.49329419	-123.714775	3-10-2016	C		Medium?
44	218	66	344.931	60.88299	NR	320.65	19.2774	98.867	64.8711	48.49329419	-123.714775	3-10-2016		possibly primary striae, ovp by striae above on undulatory plane	Old
45	210	76	263.9132	72.85363	NL	291.82	30.3058	133.34	57.8593	48.49329419	-123.714775	3-10-2016	C	Qtz crystal growth	East side of Site 3 quarry, 1x3m FP, euhedral quartz growth	?
46	280	55	332.1802	48.44614	NL	353.15	7.09825	244.03	69.1847	48.48628927	-123.687623	23-9-2016	A	Gouge in lee of accretionary qtz risers, chloritic lunate fractures in a chain indicate S side down	subtle chl ovp of qtz min growth	?
47	280	90	280	45	TR	225.26	30	334.74	30	48.48628927	-123.687623	23-9-2016	B	incongruent reg fracture steps 2-3cm long	Smoothed chl- basalt 3x3m FP minor lt orange gougey material lower on outcrop	?
48	289	85	307.0181	74.20675	TR	214.84	47.9057	5.5279	38.2275	48.48628927	-123.687623	23-9-2016	B	smooth striated qtz-ep plane	Irwin Rd.	Old
49	45	20	53	2.899831	TR	33.399	44.4459	250.94	38.9536	48.44629	-123.548747	17-9-2015	A	Concave dipping RM	Cm-scale mod striae on chl-cly alt surface mm-wide coating, cm-wide friable gouge, truncated by 52	Old
50	273	55	11.67258	54.68982	TL	163.62	79.2972	6.5865	9.87179	48.46200874	-123.597295	28-9-2015	A	Concave dipping RM	Cm-scale mod striae on chl-cly alt surface mm-wide coating, cm-wide friable gouge, truncated by 52	Old
51	288	60	18	60	TL	198	75	18	15	48.46200874	-123.597295	28-9-2015	A		White ppt min., frac, same plane 53-54	Young
52	332	65	90.64693	62.01606	TL	217.54	67.4085	71.685	19.0016	48.46200874	-123.597295	28-9-2015	B	RM planes dipping	same plane 52-54	Young
53	334	65	145.2553	18.05776	TL	193.03	31.1997	285.8	4.56847	48.46200874	-123.597295	28-9-2015	C		same plane as above secondary striae	Young?
54	334	65	82.39444	63.82977	TL	228.08	68.9801	69.997	19.6202	48.46200874	-123.597295	28-9-2015	B			?
55	306	58	37	57.99608	TL	214.33	76.9935	36.385	12.9985	48.49304793	-123.71132	6-10-2016	C			?
56	131	80	237.794	79.56408	NR	223.59	34.9333	37.309	54.9048	48.49304793	-123.71132	6-10-2016	B			?
57	301	50	31	50	NR	31	5	211	85	48.49304793	-123.71132	6-10-2016	B		qtz-ep-chl-cly-feox mm coating	Old + FeOx
58	283	31	13	31	NR	193	14	13	76	48.49304793	-123.71132	6-10-2016	A			?
59	298	42	28	42	NR	208	3	28	87	48.49304793	-123.71132	6-10-2016	B		R shear of 58	?
60	266	66	356	66	NL	356	21	176	69	48.49304793	-123.71132	6-10-2016	B			?
61	106	87	136.888	84.17101	NL	191.26	41.7932	21.261	47.7704	48.49304793	-123.71132	6-10-2016	B			?
62	271	84	74.97649	69.15474	TL	160.11	47.2849	18.38	35.9381	48.49304793	-123.71132	6-10-2016	A			?
63	109	88	120.1956	79.80399	NL	189.46	42.1646	29.201	46.1055	48.49304793	-123.71132	6-10-2016	B			?
64	160	80	329.4515	46.07453	TL	31.514	39.2035	281.53	22.7369	48.49304793	-123.71132	6-10-2016	D			?
65	103	64	190.7198	63.98211	NL	192.25	18.9941	15.17	70.983	48.49304793	-123.71132	6-10-2016	B			?
66	300	58	300	0	NL	160.3	22.0064	259.7	22.0064	48.49304793	-123.71132	6-10-2016	D			?
67	212	70	355.7413	58.39165	NR	320.68	21.1225	88.133	57.5706	48.49304793	-123.71132	6-10-2016	A			?
68	267	71	273.7579	18.86784	TR	225.4	27.3149	135.36	0.08839	48.49304793	-123.71132	6-10-2016	B			?
69	26	78	38.56897	45.67368	NL	84.892	21.0283	335.54	40.7576	48.49304793	-123.71132	6-10-2016	D			?
70	251	53	251	0	NL	109.61	25.1853	212.39	25.1853	48.49304793	-123.71132	6-10-2016	D			?
71	21	85	31.58678	64.53645	TR	315.74	44.4307	89.542	35.225	48.49304793	-123.71132	6-10-2016	A			?
72	256	84	65.73784	59.46074	TL	137.05	43.0731	10.741	32.351	48.49304793	-123.71132	6-10-2016	D			?
73	222	55	347.1608	49.42054	TL	79.49	70.4981	327.5	7.55461	48.49304793	-123.71132	6-10-2016	B			?
74	261	81	261	0	TR	216.35	6.35082	125.65	6.35082	48.49304793	-123.71132	6-10-2016	D	R shears	Chl-musc coating, cm-scale grooves	?
75	281	73	311.9406	59.26283	TR	223.3	54.5391	351.22	23.6429	48.49304793	-123.71132	6-10-2016	B			?
76	94	78	115.3567	59.72926	NL	162	27.6248	34.577	49.2628	48.49304793	-123.71132	6-10-2016	B			?
77	269	60	48.10661	48.59038	TL	129.89	62.1144	20.052	10.1821	48.49304793	-123.71132	6-10-2016	B			?
78	260	54	260	0	TR	221.03	24.5588	118.97	24.5588	48.49304793	-123.71132	6-10-2016	D			?
79	216	62	216	0	TR	174.56	19.3882	77.443	19.3882	48.49304793	-123.71132	6-10-2016	B			?
80	33	80	59.76231	68.61543	NL	107.18	32.3872	324.64	51.3718	48.49304793	-123.71132	6-10-2016	B			?
81	303	77	325.9318	59.35227	NL	11.187	26.697	244.18	50.1211	48.49304793	-123.71132	6-10-2016	B		thin qtz-ca-chl coating	?
82	221	80	17.74224	65.93703	NR	329.1	31.525	106.55	50.2145	48.49304793	-123.71132	6-10-2016	B		Resistivity surveys	Young
83	309	65	309	0	NL	171.19	17.3877	266.81	17.3877	48.49304793	-123.71132	6-10-2016	B			Young
84	285	65	285	0	NL	147.19	17.3877	242.81	17.3877	48.49304793	-123.71132	6-10-2016	C			?
85	334	67	106.9692	59.88175	TL	212.28	62.6143	78.875	19.594	48.49304793	-123.71132	12-10-2016	A			?
86	106	88	111.7875	70.89889	NL	178.5	40.0531	34.618	43.8564	48.49304793	-123.71132	12-10-2016	A		qtz-ep crystal growth, primary to 87	Old
87	109	88	284.7198	64.92525	NR	221.29	38.0092	355.41	41.6934	48.49304793	-123.71132	12-10-2016	A		qtz-ep sparse ca	?
88	218	75	342.2656	72.03615	NR	316.1	29.3158	114.28	58.8315	48.49304793	-123.71132	12-10-2016	C		v smooth minor chl, minor wt ppt on faces	?
89	314	71	125.3676	23.55276	NR	83.921	3.00045	175.72	30.8483	48.49304793	-123.71132	12-10-2016	C			?
90	234	71	359.3414	67.11466	NR	334.1	24.9126	124.3	61.8431	48.49304793	-123.71132	12-10-2016	D			?
91	91	70	114.6422	47.77299	NL	154.02	16.3652	43.572	49.9469	48.49304793	-123.71132	12-10-2016	C			?
92	142	82	305.3819	63.82977	NR	252.73	32.426	25.938	47.141	48.49304793	-123.71132	12-10-2016	C			?
93	295	58	341.124	49.07926	NL	6.0231	9.18322	255.38	65.369	48.49304793	-123.71132	12-10-2016	X			?
94	264	60	51.38194	43.0344	TL	121.48	56.7315	20.041	7.41197	48.49304793	-123.71132	12-10-2016	B			?
95	328	85	142.0701	49.74086	NR	89.162	28.5539	203.33	36.9589	48.49304793	-123.71132	12-10-2016	D		white clay precipitate	Young?
96	328	50	10.5518	38.86642	TR	305.34	63.9269	214.07	0.6191	48.49304793	-123.71132	12-10-2016	B			?
97	180	85	350.2933	62.57518	TL	63.699	43.5722	292.92	34.4725	48.49304793	-123.71132	12-10-2016	X			?
98	273	80	277.6293	24.59477	TR	227.84	24.6506	322.42	9.87554	48.49304793	-123.71132	12-10-2016	C			?
99	289	68	39.56454	66.65863	TL	184.95	66.0817	25.119	22.6034	48.49304793	-123.71132	12-10-2016	C			?
100	5	68	59.42456	63.58442	TR	299.6	63.9179	83.647	21.6165	48.49304793	-123.71132	12-10-2016	B		v. smooth, v. little coating	?
101	197	67	323.2738	62.23258	NR	299.01	20.4501	80.168	64.4181	48.49304793	-123.71132	12-10-2016	B			?

102	22	48	132.4361	46.14292	NR	121.86	2.10477	223.21	79.4266	48.49304793	-123.71132	12-10-2016	B		qtz-ep-ca, patchy chl (primary tourmaline/euhedral epidote?)	?
103	19	52	129.5556	50.15801	NR	118.21	6.17631	238.91	78.0324	48.49304793	-123.71132	12-10-2016	B			?
104	33	70	84.92375	65.18578	NL	111.48	23.5768	326.01	62.0879	48.49304793	-123.71132	12-10-2016	B			?
105	359	45	103.0019	44.13603	NR	276.05	0.43523	182.54	82.9335	48.49304793	-123.71132	12-10-2016	B			?
106	67	73	89.66298	51.56916	TR	15.666	49.5221	131.37	20.315	48.49304793	-123.71132	12-10-2016	B			?
107	76	60	122.9969	51.71008	NL	148.24	11.6214	31.668	65.3059	48.49304793	-123.71132	12-10-2016	B			?
108	290	85	91.98187	74.20677	NR	33.472	38.2275	184.16	47.9057	48.49304793	-123.71132	12-10-2016	B			Old
109	34	87	39.39368	60.85866	NL	99.099	35.4924	330.97	40.89	48.49304793	-123.71132	12-10-2016	C		108 secondary striae, weak	Young
110	34	87	124	87	NR	124	42	304	48	48.49304793	-123.71132	12-10-2016	X		qtz-ep, milky qtz in risers	?
111	209	67	257.6122	60.49984	TR	149.57	63.0905	284.84	19.8248	48.49304793	-123.71132	12-10-2016	X		sub-cm ca fill, hem coating	?
112	30	57	80.73487	50.01063	TR	350.01	67.9532	103.07	9.01202	48.49304793	-123.71132	12-10-2016	B			?
113	74	82	93.00706	66.65863	NL	145.5	33.4238	7.5075	48.387	48.49304793	-123.71132	12-10-2016	B		irregular chl-cly coating	?
114	31	85	89.98101	84.17101	TR	304.29	49.914	118.23	39.9278	48.49304793	-123.71132	12-10-2016	C		qtz crystals, qtz-ca-hem-Feox	Young?
115	215	79	262.2589	75.17549	NL	296.55	33.2743	137.34	54.9342	48.49304793	-123.71132	12-10-2016	B			?
116	230	70	241.1702	28.02432	TR	188.41	35.035	282.06	5.18586	48.49230742	-123.710317	260-2016	B	Fibrous crystals - incongruous risers indicate thrust - reversal?	euhedral crystal growth blue bladed mineral very smooth qtz-ep+-FeOx+chl+bt+ca surface undulating plane	Old
117	287	62	326.1162	49.87629	NL	355.81	12.0477	243.39	60.7691	48.4814951	-123.667477	20-10-2016	A	qtz-ep comp banding	primary striae, same as plane 119 - qtz-ep striae present locally qtz-ep with chl-hem-bt striae	?
118	314	63	54.90777	62.57518	TL	212.76	71.5607	47.712	17.8556	48.4814951	-123.667477	20-10-2016	D	R shears	More pervasive than 118, same plane , Ca-FeOx coating	?
119	314	63	339.9589	40.66543	TR	274.66	51.4256	14.855	8.03395	48.4814951	-123.667477	20-10-2016	B	Fibrous crystals	euhedral chrysotile growth	Old
120	265	50	328.1841	46.76511	NL	342.35	3.4768	238.4	75.8557	48.4814951	-123.667477	20-10-2016	A	incongruous T steps	same plane as 120?	?
121	256	46	22.2597	39.86168	NR	184.74	2.17703	88.47	70.8055	48.4814951	-123.667477	20-10-2016	B	R shears	Weak grooves within 2 m wide scaley fabric	?
122	144	88	320.5408	59.9396	TL	26.71	39.5445	259.9	35.9672	48.4831133	-123.675232	20-10-2016	B	R shears	~40 m W of main FZ OC folicated OC with potentially striated surfaces (weak grooves). Pervasive mod bt+-lim, sparse malachite, kyanite?	?
123	298	71	113.0144	14.16518	NR	251.17	3.27736	159.72	23.7817	48.48628927	-123.687623	21-10-2016	B	en echelon R shears	E side of quarry, ~2 m2 exposed en echelon weakly undulatory strongly grooved surfaces with qtz-chl-hem in striae	?
124	298	58	318.3576	29.10558	NL	172.58	1.7626	264.41	45.944	48.48628927	-123.687623	21-10-2016	B		similar to 124 in sequence	?
125	303	50	331.3408	29.49872	NL	179.99	6.10421	278.27	53.3889	48.48628927	-123.687623	21-10-2016	B		similar to 124 in sequence	?
126	294	58	316.4905	31.47393	NL	170.14	0.31637	260.49	48.0645	48.48628927	-123.687623	21-10-2016	B		similar to 124 in sequence	?
127	290	62	329.1162	49.87629	NL	358.81	12.0477	246.39	60.7691	48.48628927	-123.687623	21-10-2016	B	R shears	1m west of 1.5x6m FP, more weathered qtz-ep with chl-hem-bt striae	?
128	279	50	353.6602	48.97354	NL	1.9248	4.52686	241.55	81.1021	48.48628927	-123.687623	21-10-2016	B	R shears	potentially sheared till above gougy FZ in slumped block. (east side of quarry, with 128.)	?
129	294	66	324.1515	48.44619	NL	359.29	13.9778	248.66	54.7615	48.48628927	-123.687623	21-10-2016	B		discont striae on undulating discontinuous planes.	?
130	310	71	328.0336	41.95776	NL	8.9765	14.037	264.67	44.6658	48.48628927	-123.687623	21-10-2016	B	R shears ~130	within main FZ	?
131	293	80	302.8511	44.13603	NL	350.45	21.6919	242.36	37.9659	48.48628927	-123.687623	21-10-2016	B	2ndary frac direction, same plane		?
132	335	58	343.0815	12.67914	NL	200.57	12.68	298.65	31.9996	48.48628927	-123.687623	21-10-2016	B			?
133	335	58	122.7262	40.51468	TL	189.52	56.5198	92.139	4.85632	48.48628927	-123.687623	21-10-2016	B		gougey in main FZ, crosscuts other fractures	Young
134	320	25	329.0795	4.208557	TR	304.93	43.8481	170.5	36.0835	48.48628927	-123.687623	21-10-2016	A	R dips on OC scale, crescentic Ts	localized qtz-hem slicks, qtz-hem slicks, r dips, t fracs	?
135	284	90	104	65	TL	171.09	39.8557	36.91	39.8557	48.46809047	-123.609634	30-9-2016	B	R, T		?
136	284	68	14	68	TL	194	67	14	23	48.46809047	-123.609634	30-9-2016	B	fibrous mineral growth	euhedral qtz-ep-tourm crystal growth	Old
137	312	41	113.4267	15.47651	TL	152.91	46.2486	265.49	20.1802	48.42809121	-123.502356	26-9-2016	A	fibrous mineral growth	euhedral qtz-ep-tourm crystal growth	Old
138	301	37	69.04038	30.68835	TL	112.9	67.7598	233.5	11.7614	48.42809121	-123.502356	26-9-2016	A	regular tension gashes	with regular	?
139	64	87	65.59399	27.95826	TR	16.191	21.6243	113.21	17.1278	48.42809121	-123.502356	26-9-2016	B			?
140	216	59	220.1401	6.851396	TR	177.58	26.6501	79.167	16.2502	48.42809121	-123.502356	26-9-2016				?
141	330	70	330	0	NL	193.22	13.9955	286.78	13.9955	48.42809121	-123.502356	26-9-2016				?
142	102	85	102.8804	9.961558	NL	147.76	3.47954	57.109	10.5999	48.42809121	-123.502356	26-9-2016				?
143	204	80	207.6164	19.6835	NL	252.02	6.62571	159.44	21.1591	48.42809121	-123.502356	26-9-2016				?
144	94	64	105.553	22.32419	NL	324.1	2.37175	55.787	35.3499	48.42809121	-123.502356	26-9-2016	B			?

145	122	59	230.899	57.58045	TL	5.6093	73.9639	219.25	13.4569	48.44397413	-123.528848	13-10-2016	B			?
146	159	70	254.8298	69.90432	TL	65.659	64.9452	250.56	24.9744	48.44397413	-123.528848	13-10-2016	B		Upper Goldstream by campsite	?
147	284	88	285.6774	39.97072	TR	232.1	28.6149	337.14	25.44	48.46121362	-123.556911	13-10-2016	B			?
148	220	58	310	58	NL	310	13	130	77	48.44397413	-123.528848	13-10-2016	B			?
149	42	60	132	60	TL	312	75	132	15	48.45976305	-123.559217	13-10-2016	C			?
150	201	75	18.38702	9.655936	NR	155.25	3.69291	64.082	17.5547	48.44397413	-123.528848	13-10-2016	C			?
151	165	84	166.0559	9.944661	TR	120.25	11.3048	210.8	2.76286	48.44397413	-123.528848	13-10-2016	B			?
152	120	75	187.8983	73.87011	TR	38.392	59.574	205.12	29.7528	48.44397413	-123.528848	13-10-2016	X			?
153	108	62	198	62	TR	18	73	198	17	48.44397413	-123.528848	13-10-2016	X			?
154	128	79	159.9686	69.84014	TR	58.095	53.0069	203.9	31.9287	48.44397413	-123.528848	13-10-2016	X			?
155	110	75	218.6768	74.20678	TL	12.983	59.7035	204.07	29.8282	48.44397413	-123.528848	13-10-2016	X			?
156	338	68	347.9086	23.06934	NL	28.141	0.69841	297.69	32.8174	48.46339	-123.591	8-10-2016	B			?
157	17	55	185.208	16.27014	TL	230.54	37.1345	329.78	11.9743	48.46339	-123.591	8-10-2016	C			?
158	306	54	36	54	TL	216	81	36	9	48.46339	-123.591	8-10-2016	C			?
159	290	86	20	86	TL	200	49	20	41	48.46339	-123.591	8-10-2016	X		chl coating	?
160	276	70	338.7268	67.73125	TR	202.07	63.6647	358.25	24.3635	48.46339	-123.591	8-10-2016	D			?
161	140	88	151.1956	79.80399	TR	60.201	46.1055	220.46	42.1646	48.46339	-123.591	14-10-2016				?
162	284	85	77.69751	78.83105	TL	183.2	49.0553	23.117	39.2042	48.46339	-123.591	14-10-2016	A			?
163	225	55	332.0883	53.77546	TL	100.67	77.424	322.15	9.48843	48.46339	-123.591	14-10-2016	B			?
164	178	70	178	0	TR	134.78	13.9955	41.219	13.9955	48.44397413	-123.528848	13-10-2016	B			?
165	266	66	356	66	TR	176	69	356	21	48.46341	-123.59038	8-10-2016	X			?
166	107	80	247.7529	74.4266	NR	207.21	33.9424	2.6879	53.5075	48.46341	-123.59038	14-10-2016	B			?
167	166	75	190.1461	56.77406	TR	109.98	50.7615	233.21	24.1102	48.46341	-123.59038	14-10-2016	B			?
168	292	89	100.7186	84.90124	NR	26.897	43.7861	196.93	45.7785	48.46341	-123.59038	14-10-2016	A			?
169	52	62	85.84086	46.32498	NL	117.65	10.3384	11.013	57.5003	48.46341	-123.59038	14-10-2016	D			?
170	272	63	310.1792	50.50088	TR	227.12	60.0714	340.73	12.9798	48.46341	-123.59038	14-10-2016	B			?
171	282	85	326.8908	82.93343	TR	197.47	49.7617	7.3991	39.7998	48.44397413	-123.528848	13-10-2016	B			?
172	275	68	292.4496	36.58269	TR	233.14	43.3387	331.74	9.00591	48.46742539	-123.590156	8-10-2016	X			?
173	98	64	114.4722	30.17211	TR	59.746	41.7105	152.07	2.60305	48.46742539	-123.590156	8-10-2016	D			?
174	105	63	120.8378	28.1747	TR	67.513	40.9112	158.15	0.73621	48.46742539	-123.590156	8-10-2016	D			?
175	134	65	216.931	64.83214	TR	50.168	69.8534	221.74	19.9465	48.44397413	-123.528848	13-10-2016	A			?
176	298	68	28	68	TL	208	67	28	23	48.46293	-123.591	30-9-2016	C			?
177	72	70	228.3578	47.77299	NR	188.98	16.3652	299.43	49.9469	48.46293	-123.591	30-9-2016	B			?
178	57	45	198.8567	31.70074	NR	355.5	7.37874	252.19	60.6419	48.46293	-123.591	30-9-2016	D		through-going fault	?
179	47	48	213.3124	14.72444	NR	1.0318	17.0629	255.69	40.7585	48.462935	-123.5917	30-9-2016	A			?
180	130	40	290.3426	15.76273	NR	83.158	20.462	329.39	47.2029	48.462935	-123.5917	30-9-2016	A			?
181	96	80	107.6921	48.97354	TR	43.04	41.0133	156.1	24.2462	48.462935	-123.5917	30-9-2016	C			?
182	73	55	241.208	16.27014	NR	25.785	11.9743	286.54	37.1345	48.462935	-123.5917	30-9-2016	C		smooth ca coating direction .. modern?	?
183	82	65	248.2878	26.94622	NR	209.77	1.23723	300.75	38.2624	48.462935	-123.5917	30-9-2016	X		dm-scale	?
184	18	82	45.44741	73.04331	NL	95.041	35.3069	304.83	50.7847	48.494	-123.718	3-10-2016	D	R dips	Sub-m rough plane with very little coating, weak cm-scale groove	?
185	262	41	352	41	TR	352	86	172	4	48.494	-123.718	3-10-2016	C	R dips	v. little coating, chl-wt ppt	?
186	186	70	276	70	TR	96	65	276	25	48.494	-123.718	3-10-2016	B	R dips	v. little coating	?
187	264	50	354	50	TR	174	85	354	5	48.42697704	-123.476297	60-2016	A		delta sediments cm-scale	Young
188	260	50	350	50	TR	170	85	350	5	48.42697704	-123.476297	60-2016	B		delta sediments cm-scale	Young
189	148	70	155.096	18.74724	TR	106.8	27.9762	16.353	0.83569	48.42697704	-123.476297	60-2016	D		delta, m-scale	?
190	268	89	358	89	TR	178	46	358	44	48.42697704	-123.476297	60-2016	D		delta sediments cm-scale	?
191	203	70	339.7808	62.00912	NR	308.17	22.4915	84.05	60.0241	48.4622	-123.5791	15-10-2016	D			?
192	216	60	306	60	NL	306	15	126	75	48.4622	-123.5791	15-10-2016	X			?
193	292	66	89.15975	41.08285	TL	153.79	48.7884	51.939	10.1991	48.42746493	-123.50295	26-9-2016	B			?
194	288	55	78.16243	35.39626	TL	138.32	54.6028	48	0.22897	48.42746493	-123.50295	26-9-2016	A			?
195	308	30	60.79588	28.02432	TL	85.464	70.8397	232.59	16.2686	48.42746493	-123.50295	26-9-2016	A			Old + FeOx
196	300	10	50.28356	9.391286	NR	227.29	35.5196	54.463	54.267	48.42746493	-123.50295	26-9-2016		crystal growth	aligned crystal growth with calcite, pale pink min overprint, FeOx	Old
197	212	50	225.1678	15.18892	TR	181.83	39.7757	78.374	15.62	48.42746493	-123.50295	26-9-2016				?
198	148	55	161.6835	18.66705	NL	16.577	10.3265	115.12	39.1906	48.46313859	-123.58941	29-9-2016	B	crystal growth	Xstal growth, squished	?
199	148	55	161.6835	18.66705	NL	16.577	10.3265	115.12	39.1906	48.46313859	-123.58941	29-9-2016	C		secondary striation into euhedral crystals, same plane as above	?
200	318	60			L											?
201	28	58	197.0831	16.86092	TL	243.36	35.4369	340.39	9.76535	48.46313859	-123.58941	29-9-2016	B		broad striae appear to ovp qtz growth	?
202	28	58	43.73588	23.46161	TR	353.83	41.0132	259.17	5.34692	48.46313859	-123.58941	29-9-2016			qtz crystal growth, same plane as above(primary?)	?
203	278	70	8	70	NR	8	25	188	65	48.46313859	-123.58941	29-9-2016	B	R shears dip	Conjugate to 204, FeOx lim coated plain, poorly developed grooves.	?
204	332	60	351.2953	29.78401	NL	206.6	0.13241	296.74	44.8131	48.46313859	-123.58941	29-9-2016	B		Conjugate to 203, FeOx lim coated plain, poorly developed grooves.	?

205	136	70	226	70	NL	226	25	46	65	48.46313859	-123.58941	29-9-2016	B		Sub-parallel broken planes with v smooth grooves	Young?
206	306	50	322.6854	18.88952	TR	277.39	43.1132	174.87	13.038	48.46313859	-123.58941	29-9-2016	B		v smooth subtle chl slicks, ~ 7m exposed	?
207	30	45	191.7511	17.38772	TL	234.25	45.3415	342.02	16.7796	48.46313859	-123.58941	29-9-2016	C		qtz crystal growth, T fractures (primary, smoothed by secondary?	?
208	30	45	191.7511	17.38772	NR	342.02	16.7796	234.25	45.3415	48.46313859	-123.58941	29-9-2016	C		R planes dipping, smoothing qtz crystal growth	?
209	235	70	260.2087	49.48424	NL	299.21	17.2005	186.56	51.2063	48.46313859	-123.58941	29-9-2016	A		huge block, potentially gravitational	?
210	106	80	241.4385	75.89397	TL	3.9549	53.9567	204.54	34.2633	48.46313859	-123.58941	29-9-2016	A	R, crescentic Ts	R planes dip	?
211	328	55	142.2249	8.177733	NR	284.99	17.758	184.15	30.4085	48.46313859	-123.58941	29-9-2016	B		Smooth q tz-ep-chl plane, discontinuous, sub-m	?
212	330	38	339.5086	7.354224	TR	305.21	40.3699	188.55	27.82	48.46313859	-123.58941	29-9-2016	X			?
213	330	60	330	0	NL	190.89	20.7048	289.11	20.7048	48.46313859	-123.58941	29-9-2016			Grooves on smooth qtz-ep-chl plane	?
214	343	60	53.5746	58.52505	TR	277.93	73.0624	65.715	14.4489	48.46313859	-123.58941	29-9-2016	A	crescentic divets		?
215	282	71	320.8622	61.24319	NL	355.28	22.9351	222.2	58.2237	48.4819	-123.6678	20-10-2016	B	crescentic divets	Undulating smooth plane with smooth qtz-chl-ca-hem coating	?
216	292	85	302.5868	64.53645	NL	0.5419	35.225	226.74	44.4307	48.4819	-123.6678	20-10-2016	C	fibrous mineral growth	Undulating smooth plane, intersects 214 euhedral chrysotile	?
217	262	35	333.8868	33.64409	NL	161.26	10.8051	302.06	76.1649	48.4819	-123.6678	20-10-2016	A	very subtle crescentic T chain fabric	growth m-scale fault plane	Old
218	262	35	73.78112	5.716165	NR	225.99	30.5839	105.65	40.5157	48.4819	-123.6678	20-10-2016	X	crescentic fractures		?
219	327	50	357.0609	30.83608	TR	302.67	54.7827	205.15	5.28259	48.4819	-123.6678	20-10-2016	B	crescentic Ts	dm-scale	?
220	238	47	8.249806	39.29926	NR	168.72	1.97049	73.719	68.4514	48.4819	-123.6678	20-10-2016	B	R shears		?
221	245	42	328.2856	41.80399	NL	151.46	3.10331	284.24	85.436	48.4819	-123.6678	20-10-2016	B	R shears	undulatory well-grooved planes with smooth qtz-ep-FeOx coating	?
222	280	48	338.8761	43.55352	NL	354.64	0.80631	261.86	73.8148	48.4819	-123.6678	20-10-2016	B	Crescentic T, serrated	smooth qtz-ep-FeOX	?
223	293	68	338.8251	60.60632	NL	8.031	20.5603	233.74	61.7592	48.4819	-123.6678	20-10-2016	C	en echelon qtz-ep grooves	dm-scale S-side up scarp along rd with gully - potentially natural	Young?
224	265	38	352.4626	37.97274	TR	343.52	82.8764	173.58	7.01531	48.4819	-123.6678	20-10-2016	C		qtz-ep	?
225	300	57	76.66997	46.57793	TL	156.28	63.9873	50.886	7.38066	48.45774039	-123.573424	21-10-2016	A			?
226	308	35	78.52368	28.02432	TL	118.36	65.7078	242.74	14.2999	48.45774039	-123.573424	21-10-2016	A			?
227	308	35	31.9037	34.84748	TR	18.228	79.503	214.41	10.0898	48.45774039	-123.573424	21-10-2016	B			?
228	12	60	102	60	TL	282	75	102	15	48.45774039	-123.573424	21-10-2016	X		very indistinct grooves	?
229	4	45	30.341	23.92746	TR	343.79	51.8864	237.64	12.3106	48.45774039	-123.573424	21-10-2016	X			?
230	315	20	45	20	TL	45	65	225	25	48.42812088	-123.502473	26-9-2016	C			?
231	44	88	222.8457	29.97985	TL	272.59	22.2108	174.42	19.1875	48.4297383	-123.4	6-4-2017	A			?
232	255	62	0	61.16871	NR	350.29	16.7077	148.34	72.068	48.49304793	-123.71132	6-10-2016	B			?
233	100	71	183.8778	70.89889	NL	188.43	25.974	13.221	63.9468	48.50386763	-123.782583	11-08-2016	A			Young
234	116	71	188.1082	70.10855	NL	201.29	25.7668	35.544	63.5253	48.50386763	-123.782583	11-08-2016	A			Young
235	105	72	146.9064	64.05856	NL	180.33	24.6675	41.295	58.69	48.50386763	-123.782583	11-08-2016	A			Young
236	105	66	220.5432	63.73554	NR	203.27	20.2734	354.64	67.1777	48.50386763	-123.782583	11-08-2016	B			Young
237	110	85	200	85	NL	200	40	20	50	48.50386763	-123.782583	11-08-2016	A			Young
238	130	64	186.8107	59.76602	NL	208.21	17.5146	70.001	67.0578	48.50386763	-123.782583	11-08-2016	A			Young
239	145	74	145	0	NL	8.8685	11.2392	101.13	11.2392	48.50386763	-123.782583	11-08-2016	D			Young
240	210	80	211.7538	9.846552	NL	75.864	0.10688	165.89	14.1056	48.44397413	-123.528848	6-4-2017	B		thrusting, crosscutting 215/216, feox-carb similar to main fault 242	?
241	258	45	308.7685	37.76125	TR	247.27	68.9094	147.25	3.84096	48.4819	-123.6678	13-4-2017	B			Young?
242	322	72	113.8428	55.45079	TL	195.81	53.217	74.307	21.3395	48.4831133	-123.675232	12-4-2017	A			?
243	320	12	50	12	TL	50	57	230	33	48.42812088	-123.502473	18-4-2017	B		dm-scale gougy plane along bedrock	Young
244	226	85	228.3273	24.89837	TR	179.37	21.0589	274.74	13.6547	48.462935	-123.5917	30-9-2016	B		dm-scale gougy plane along bedrock, crosscuts other fault generations	Young

* A-D, X: Uncertainties are of slip-sense (not orientation of slickenlines), and are therefore bidirectional. A and B are quite good, usually comprising euhedral crystal growth, crystallization or gouge in lee of asperities, or pervasive R shears

** R, T, R', RM, RT, refer to secondary fractures of Petit (1987) and Doblas (1998)

***Abbreviations: alt: altered; bt:biotite; BX: breccia; ca:calcite; chl: chlorite; cly: clay; dk: cark; ep: epidote; FeOx: iron oxide; FP: fault plane; frac: fracture; FZ: fault zone; hem: hematite lt: light; mod: moderate; musc: muscovite; OC: outcrop; ovp: overprint; ppt: precipitate; qtz: quartz; wt: white; Xstal: crystal; zeo: zeolite

**** Relative sense of age, based on cross-cutting relationships, mineralogy, clay content and gouge, interactions with topography.

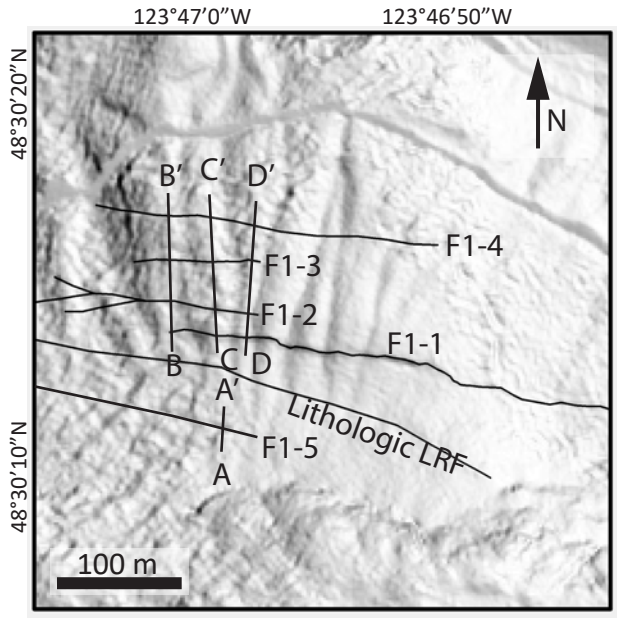
123°47'0"W
123°46'50"W
48°30'20"N
48°30'10"N
N
B′
C′
D′
F1-4
F1-3
F1-2
F1-1
B
C
D
A′
A
F1-5
Lithologic LRF
100 m

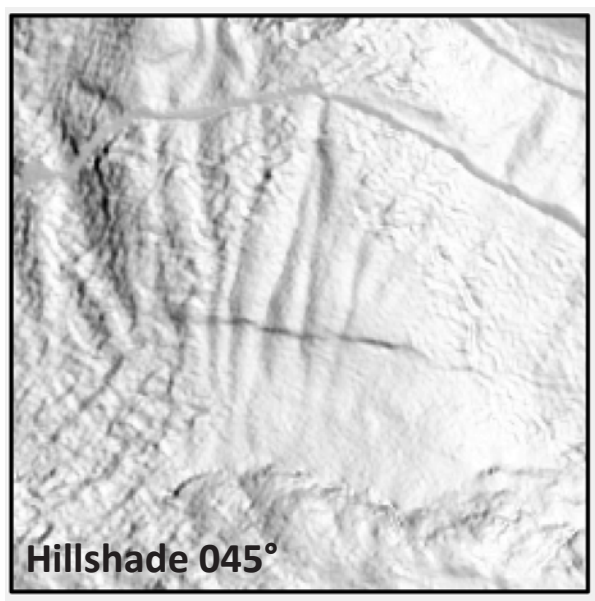
Hillshade 045°

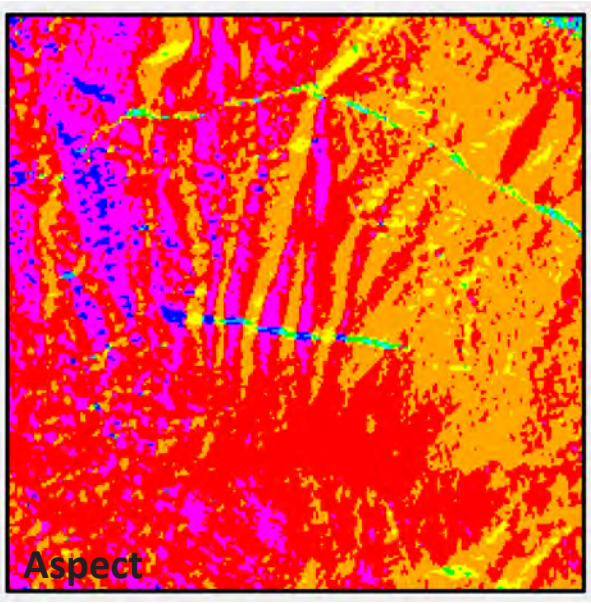
Aspect

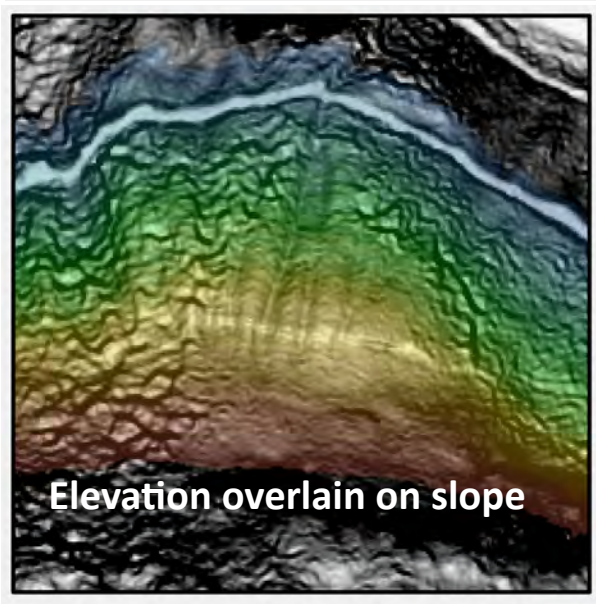
Elevation overlain on slope

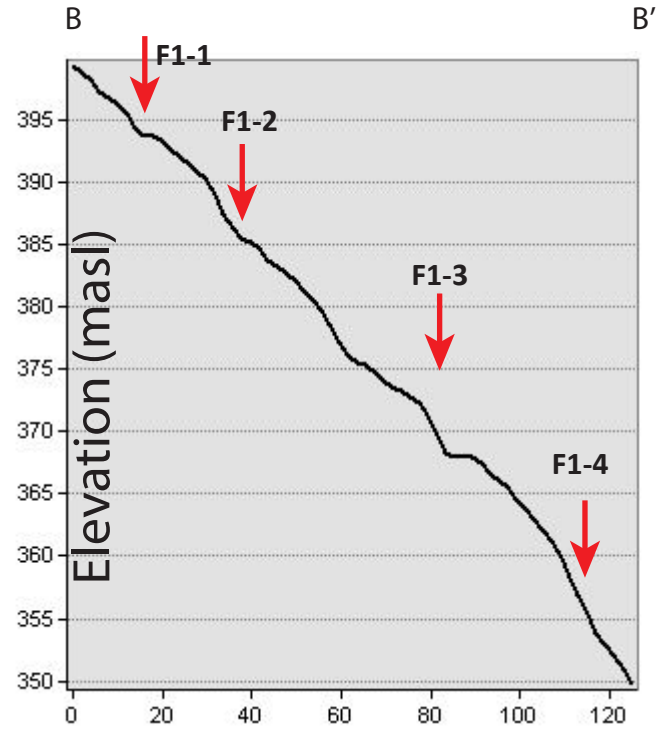
B
B′
F1-1
F1-2
F1-3
F1-4
Elevation (masl)
395
390
385
380
375
370
365
360
355
350
0
20
40
60
80
100
120

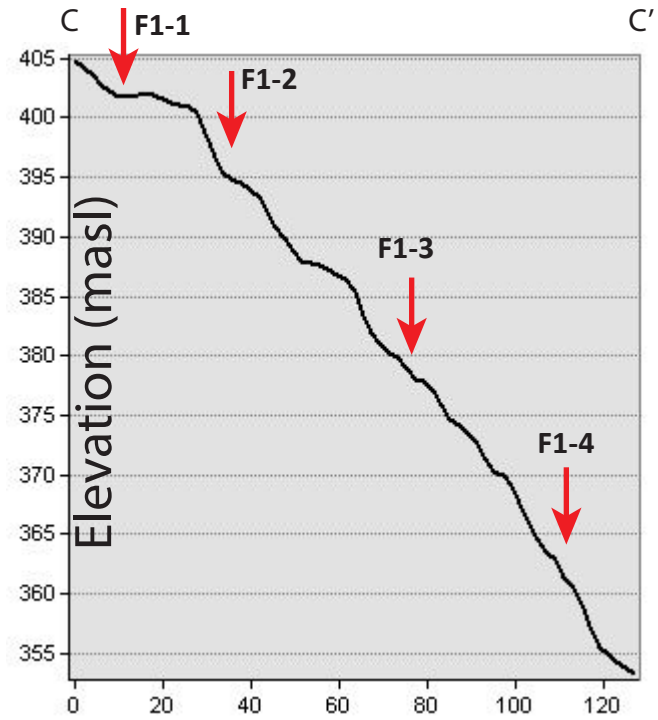
C
C′
F1-1
F1-2
F1-3
F1-4
Elevation (masl)
405
400
395
390
385
380
375
370
365
360
355
0
20
40
60
80
100
120

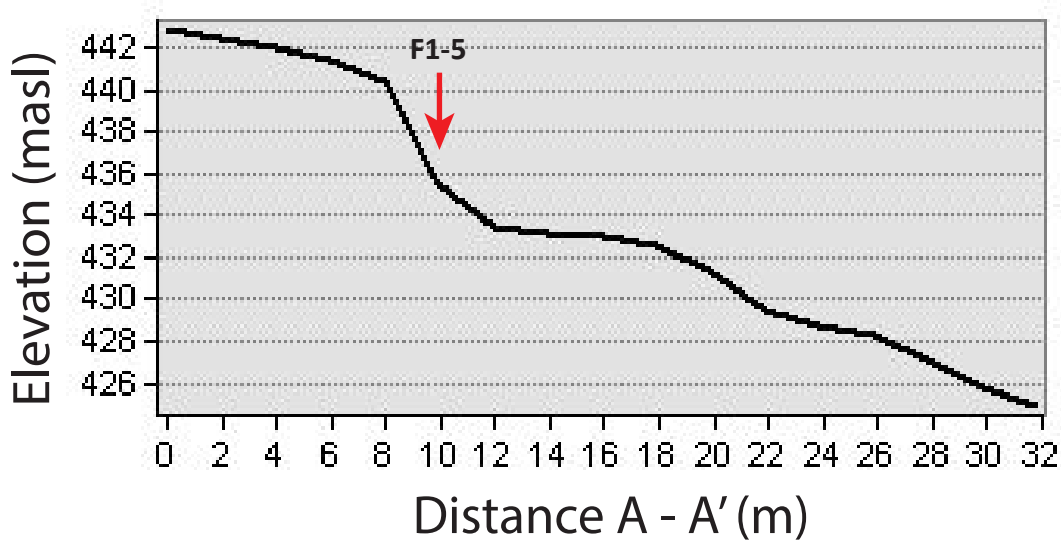
F1-5
Elevation (masl)
442
440
438
436
434
432
430
428
426
0
2
4
6
8
10
12
14
16
18
20
22
24
26
28
30
32
Distance A - A′ (m)

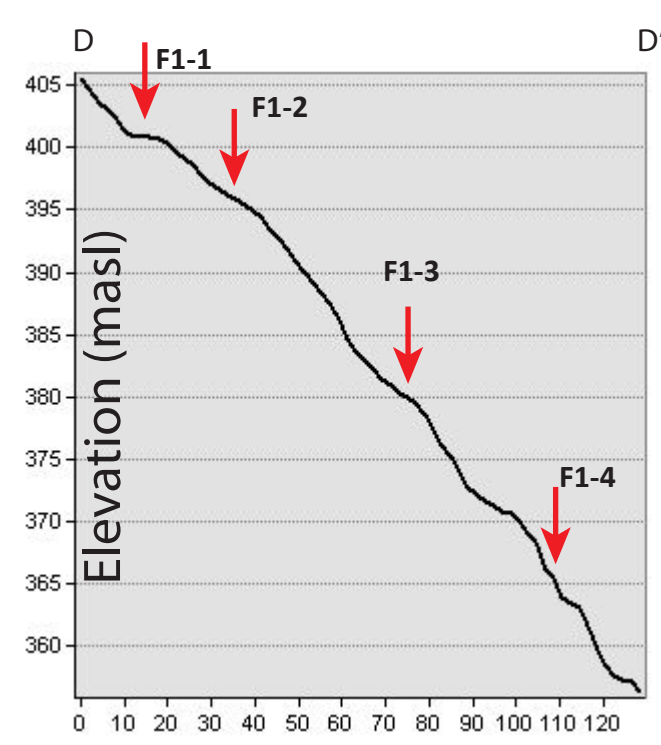
D
D′
F1-1
F1-2
F1-3
F1-4
Elevation (masl)
405
400
395
390
385
380
375
370
365
360
0
10
20
30
40
50
60
70
80
90
100
110
120

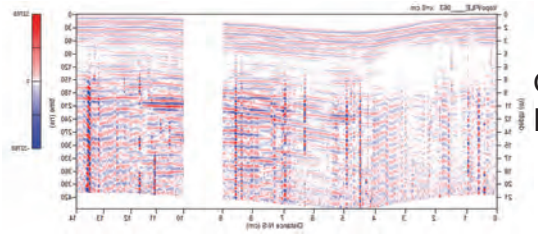

GPR9: 100 MHz, same line as GPR6

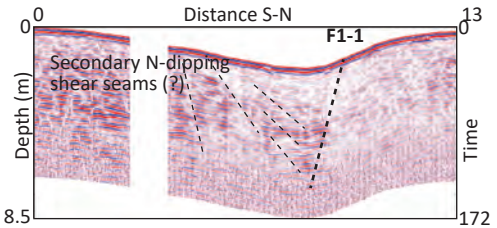

GPR 6: 400 MHz along line Fig. 4E (~3 m west of Trench 1, interfluve)

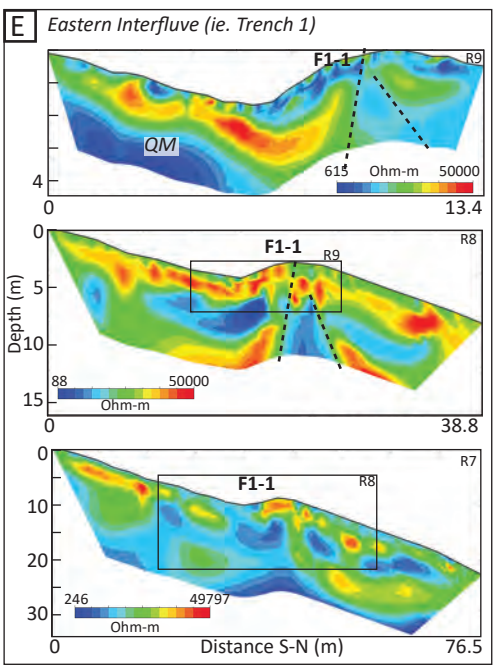

GPR7_400MHz

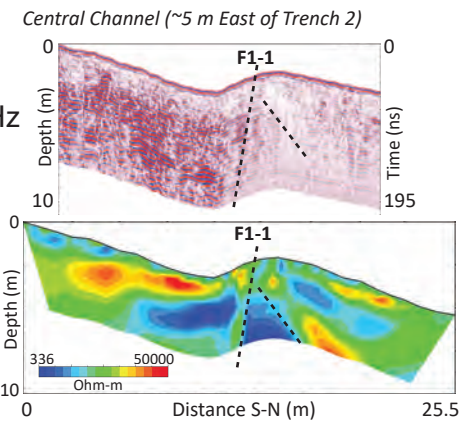

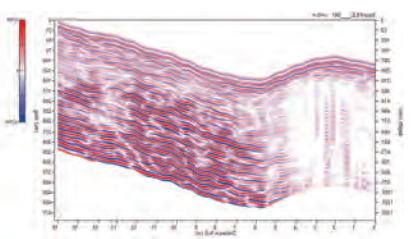

GPR8_100MHz (same line as GPR7)

100 MHz GPR:

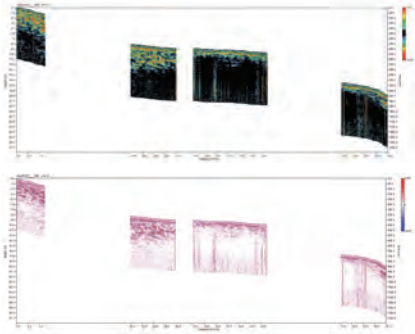

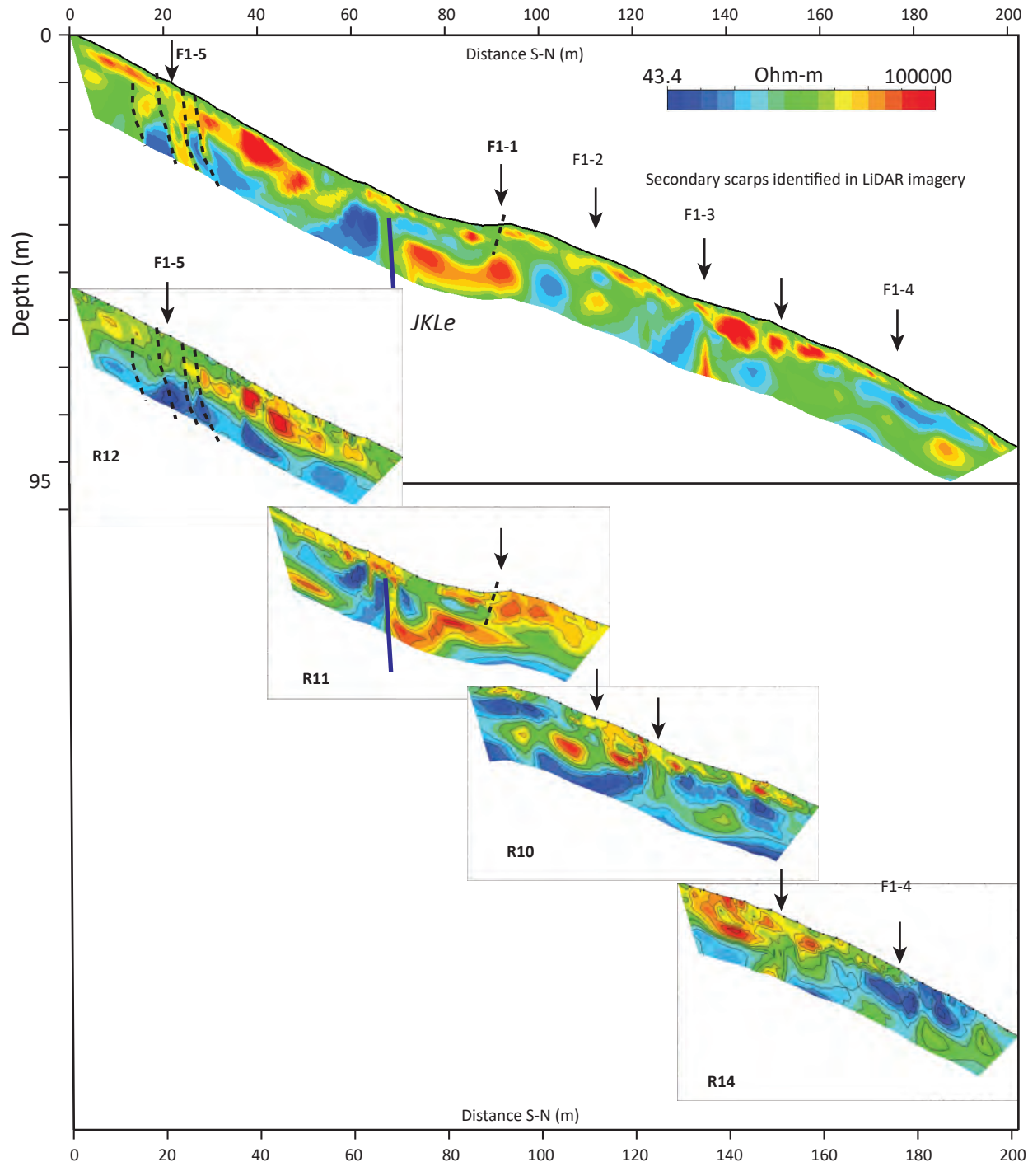
0
20
40
60
80
100
120
140
160
180
200
Distance S-N (m)
Depth (m)
0
95
F1-5
43.4
Ohm-m
100000
F1-1
F1-2
F1-3
F1-4
Secondary scarps identified in LiDAR imagery
JKLe
R12
R11
R10
R14

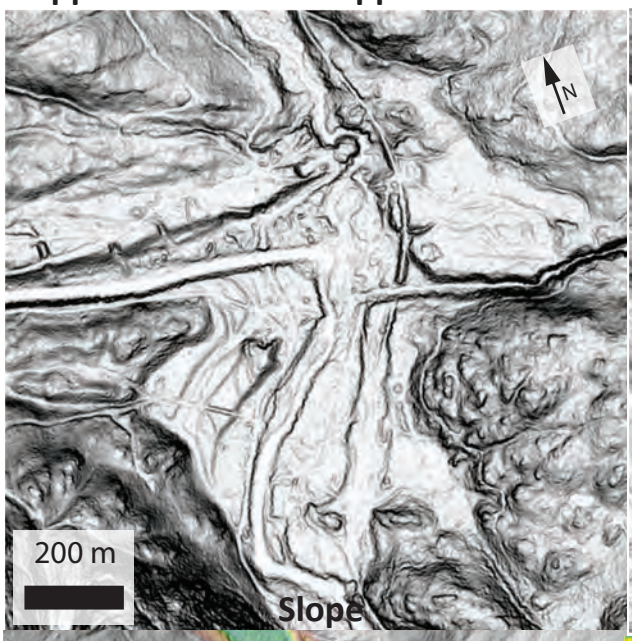

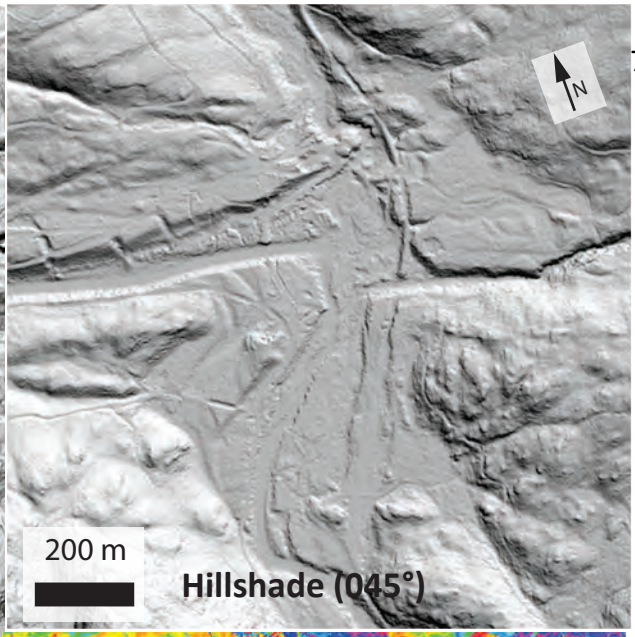

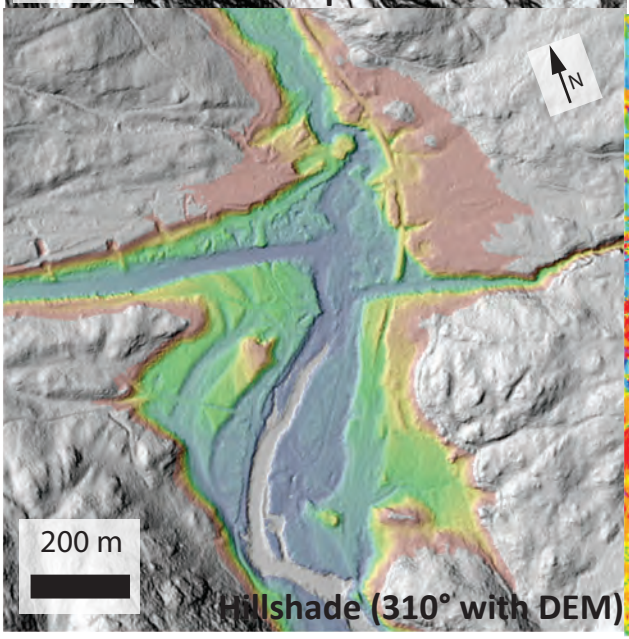

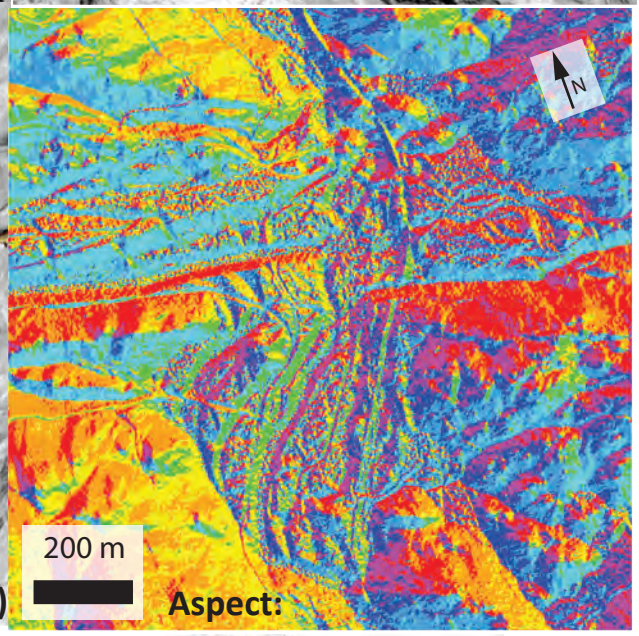

Elevation (masl)

138.4077172 - 139.0019995
139.0019996 - 139.5962818
139.5962819 - 140.1905641
140.1905642 - 140.7848463
140.7848464 - 141.3791286
141.3791287 - 141.9734109
141.973411 - 142.5676932
142.5676933 - 143.1619754
143.1619755 - 143.7562577
143.7562578 - 144.35054
144.3505401 - 144.9448223
144.9448224 - 145.5391046
145.5391047 - 146.1333868
146.1333869 - 146.7276691
146.7276692 - 147.3219514
147.3219515 - 147.9162337
147.9162338 - 148.5105159
148.510516 - 149.1047982
149.1047983 - 149.6990805
149.6990806 - 150.2933628
150.2933629 - 150.887645
150.8876451 - 151.4819273
151.4819274 - 152.0762096
152.0762097 - 152.6704919
152.670492 - 153.2647741
153.2647742 - 153.8590564
153.8590565 - 154.4533387
154.4533388 - 155.047621
155.0476211 - 155.6419033
155.6419034 - 156.2361855
156.2361856 - 156.8304678
156.8304679 - 157.4247501

Flat (-1)
North (0-22.5)
Northeast (22.5-67.5)
East (67.5-112.5)
Southeast (112.5-157.5)
South (157.5-202.5)
Southwest (202.5-247.5)
West (247.5-292.5)
Northwest (292.5-337.5)
North (337.5-360)

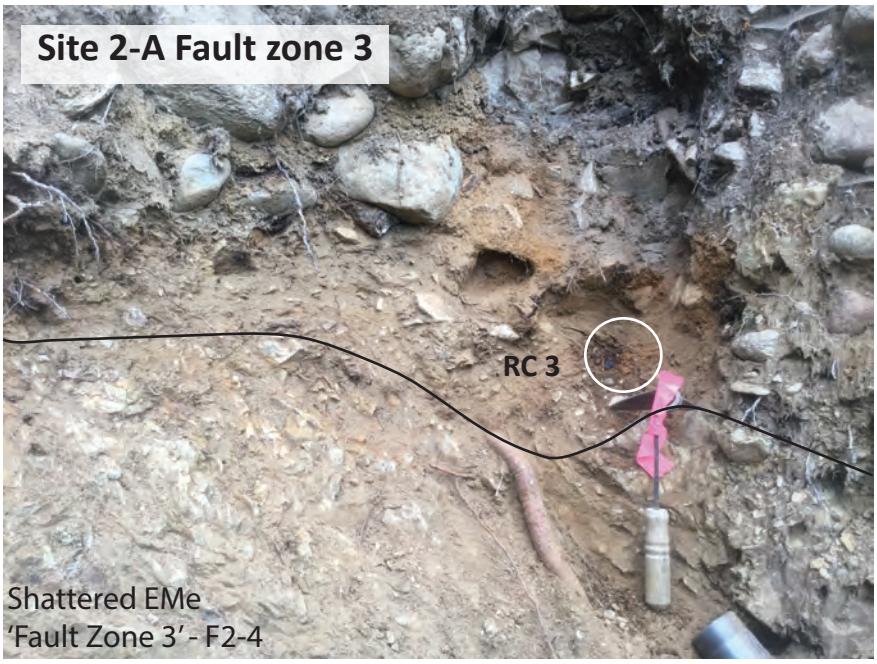

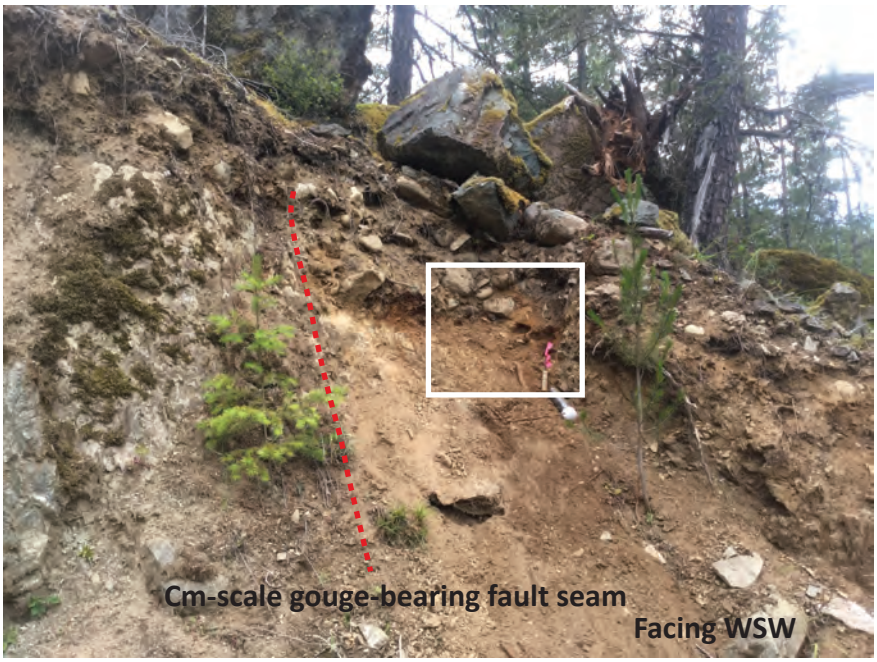

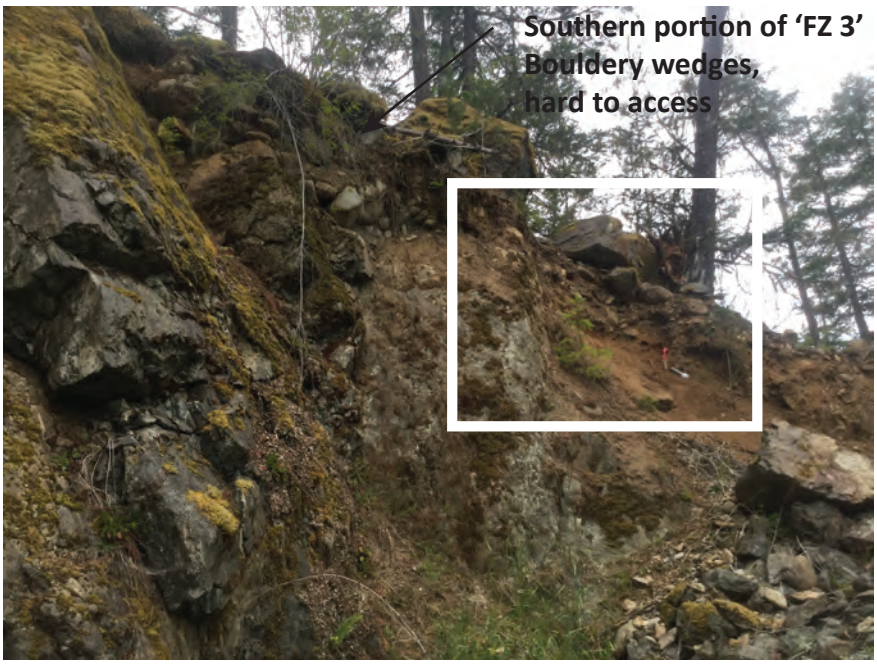

Inset terrace on Sooke West



Southern zone of steeply aligned clasts on the west bank of the Sooke River (facing west, see Fig. 9)

Southern portion of 'FZ 3' Bouldery wedges against steeply north-dipping (?) planes - hard to access. Buttress unconformities (facing southwest).



Quarry Wedge #1 (1/1)

150° July 20 '16

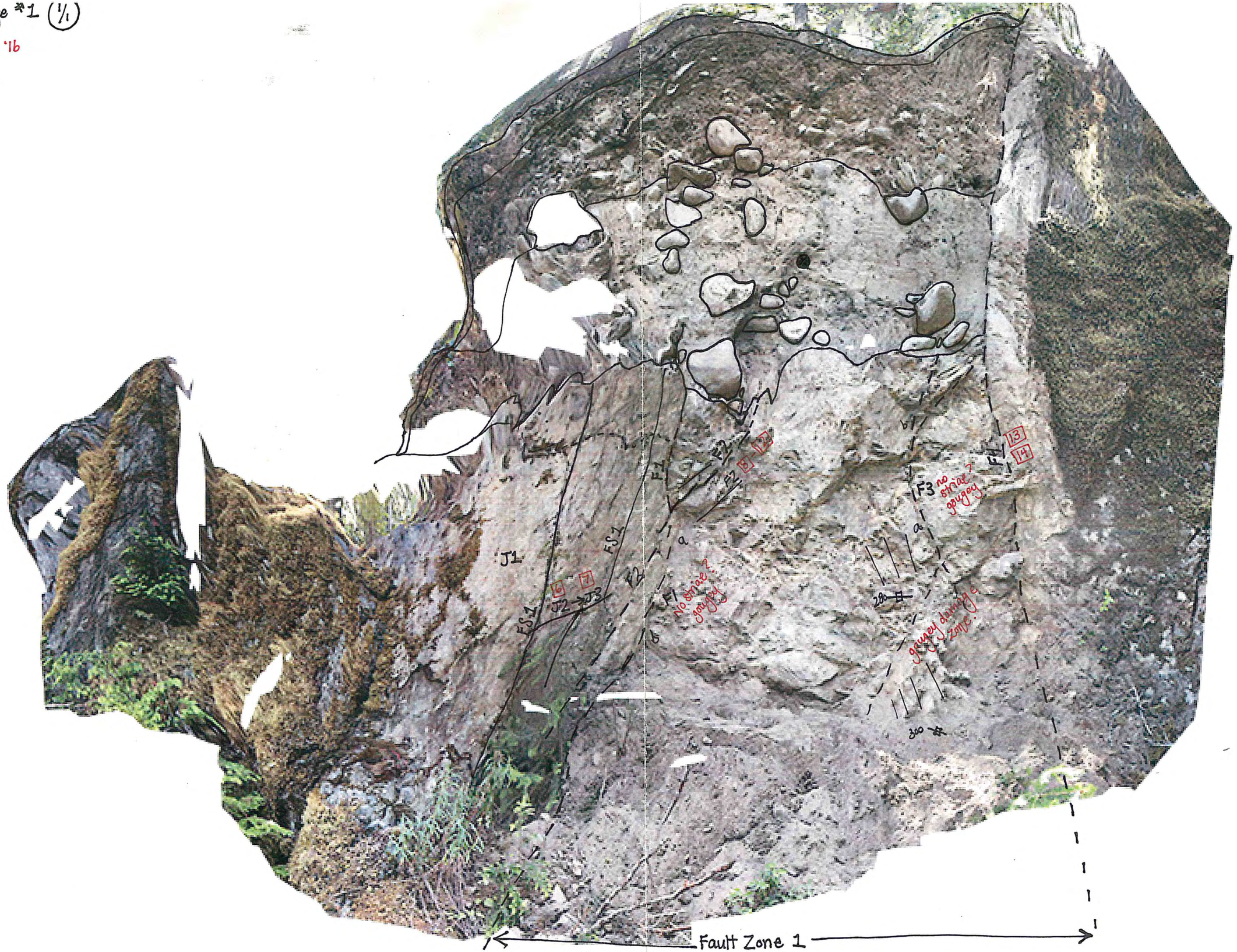


Wedges 2&3 (1/2) oct
150°
No striae observed.
F1, chl gouge in BR, rotated & frac clasts through gravel.
peb in flt gouge
open-work boulders protrude from wall, steeply dipping outward
① CUS peb gravel clast support, slt-granule matrix.
a
b
F1
F2
34

Wedges 2&3 (4/2) 087
150°

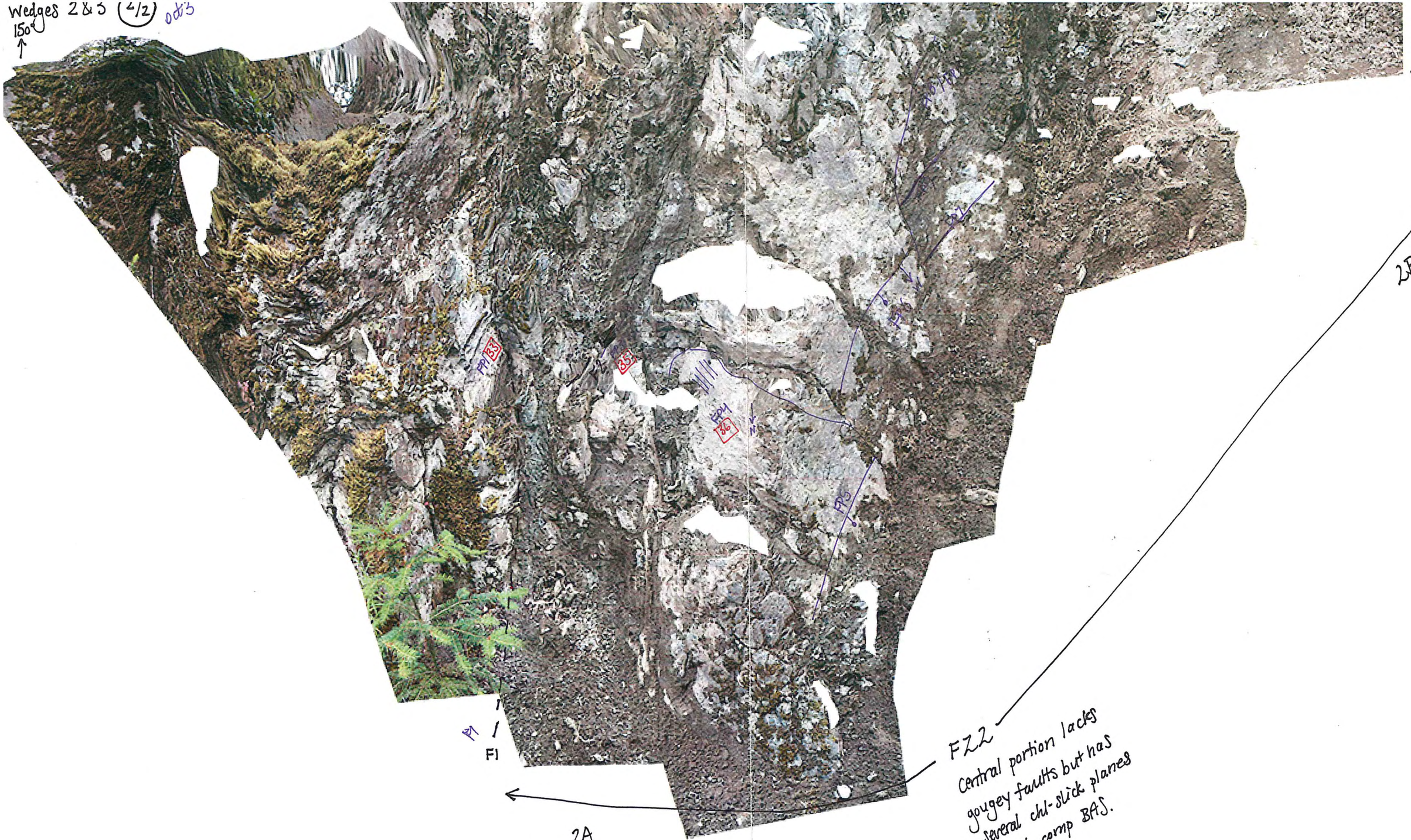




Back Wall / Wedges 4&5
4/4
MAINTHRUST
FP12
CR
27
D: ~020°/88°
cm-BX
mm-gouge
wt-gn m.

Wedges 485 (3/4)



Oct. 24 '14
CR: greenish wt vn BX
~seamount segmentation?
Re-activated.
Vein boulder float...
□ 101-2251.56

FP9 @ CR
~030/65°
1-3cm chert-rich gouge
sticky/sandy ≤ 1mm
2-10 cm cohesive BX.

gorgy
FB bounding FZ
through-going.
CR(B)?
22 ~300°/85°
05° → 129°
(Rake ~0°) Rlat. (B) N?
ShapS bound to BX gorgey FZ.
101-2243-5
CR: 'Old Fault w/ recent slip, OVP'
FZ 1
FP1 bounding FZ
FP1
CR(A)
FP(B) Merges upward w/9.
CR(B): 101-2246-9
050°/80°
45° → 065°
thin fault core w;
S. wall damage zone...
25

S

Qt3 GPR & ERT

N

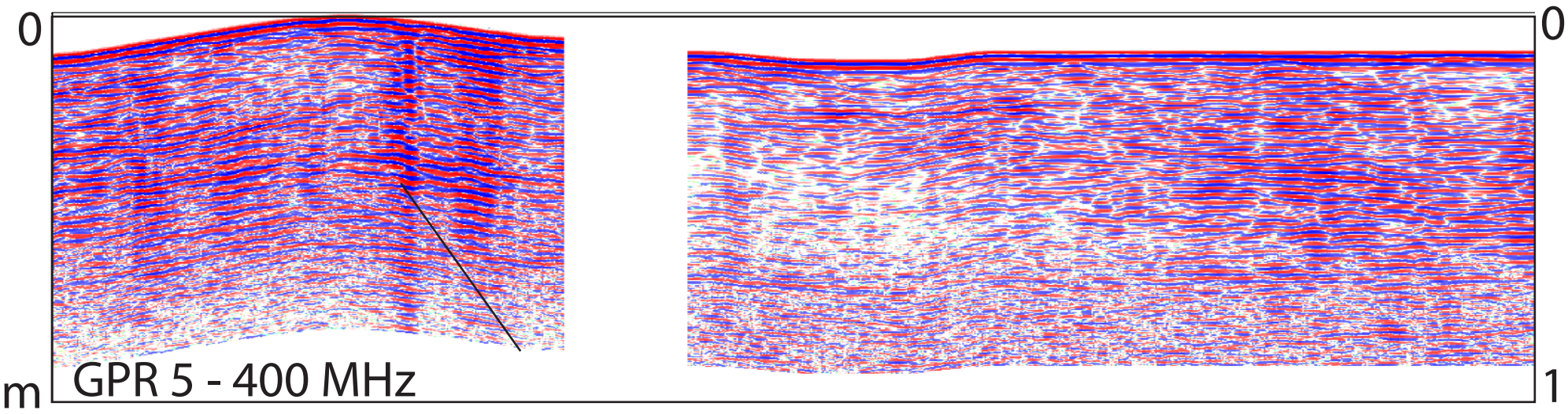

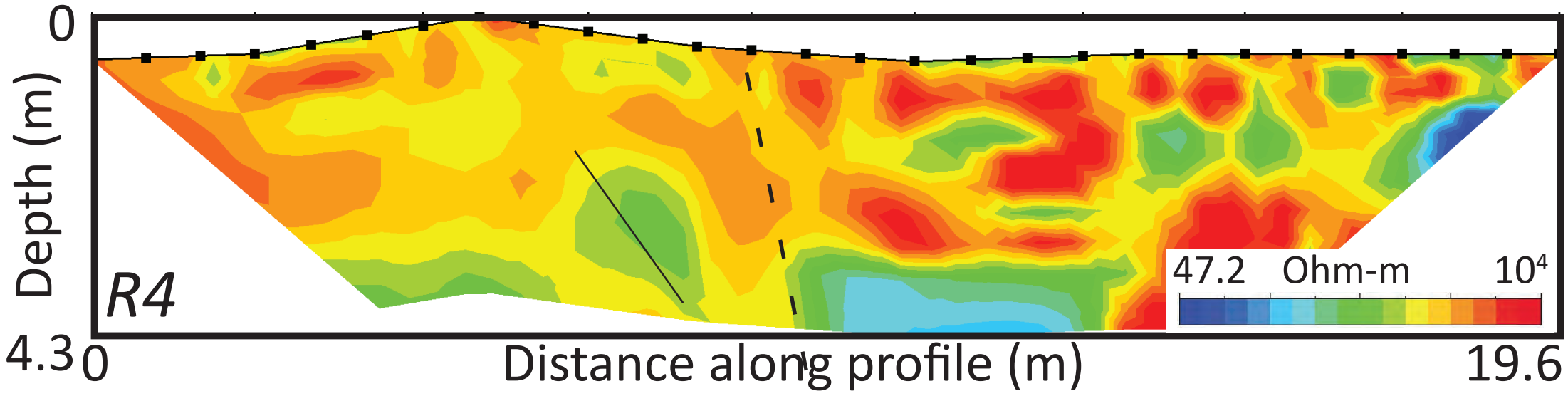

Projection of F2-6

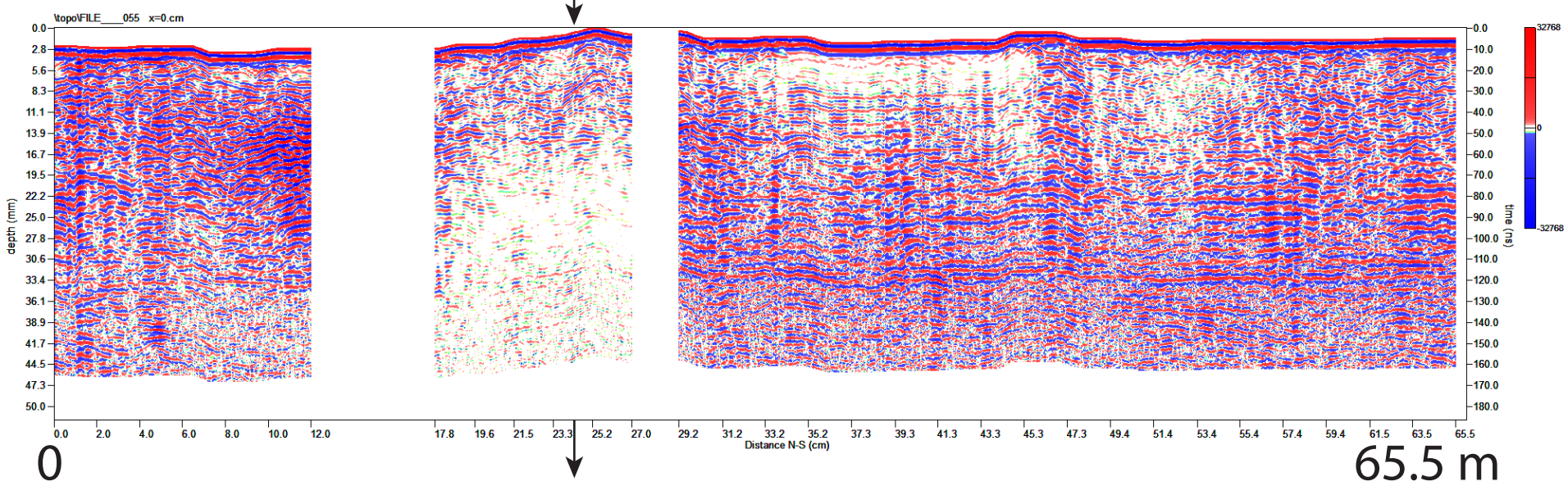

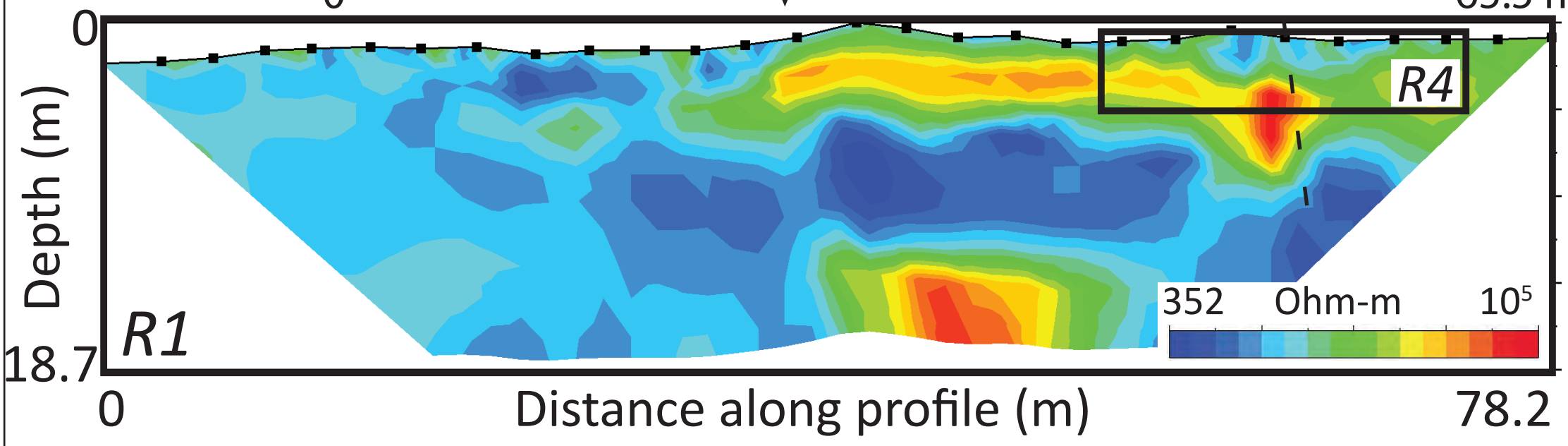

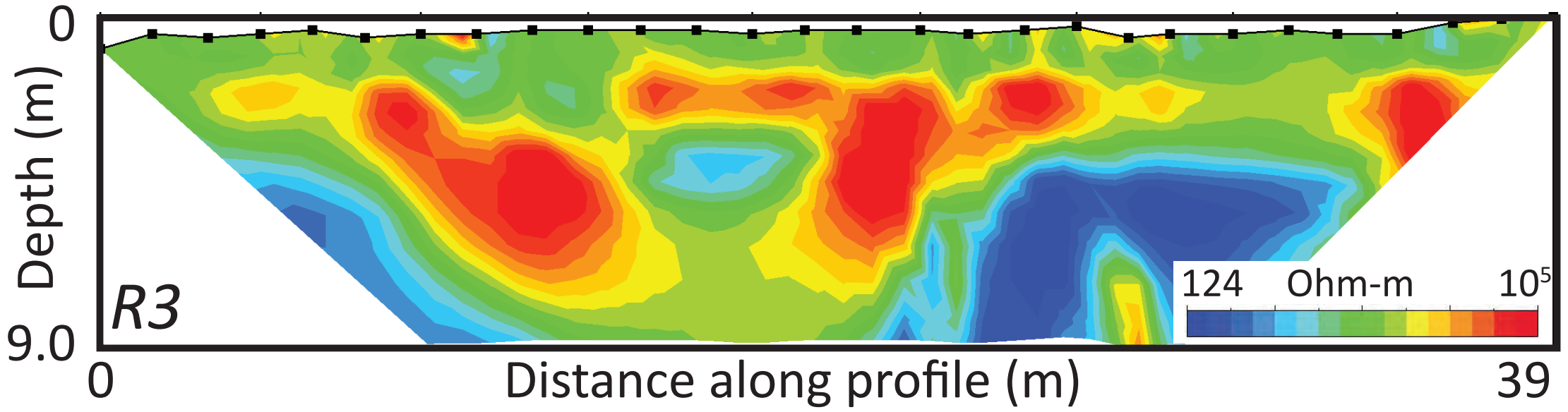

GPR_4a: 400 MHz along Qt3, R1

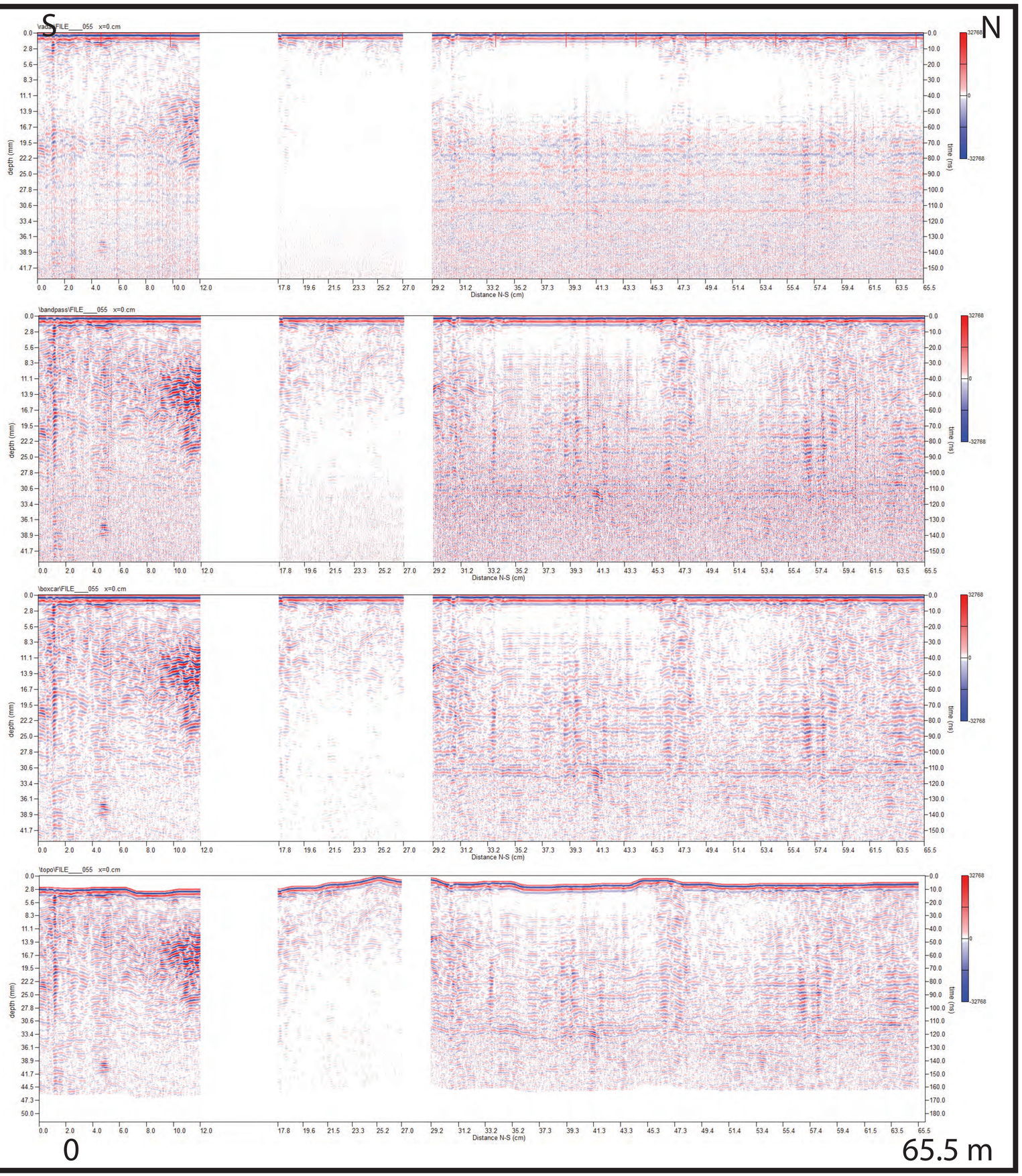

GPR_5: 400 MHz along Qt3, R4

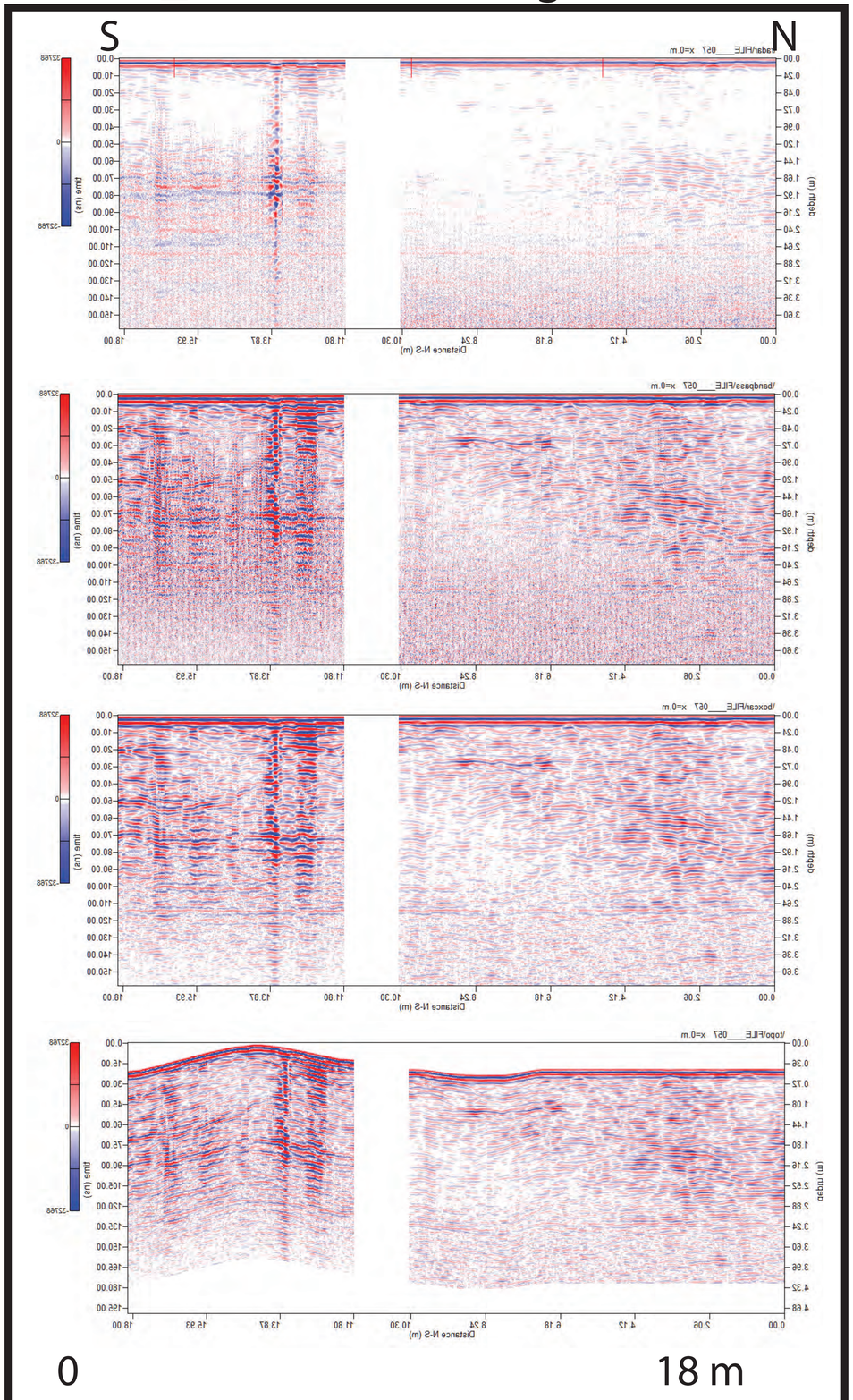

Qt4 GPR & ERT

S

Projection of F2-6

N

0

0

600 ns

GPR 17 - 100 MHz

15m

0

0

GPR 18 - 200 MHz

320 ns

19 m

0

Depth (m)

16.5

R2

370 Ohm-m 10^6

0

Distance along profile (m)

80

GPR_17 - 100 MHz

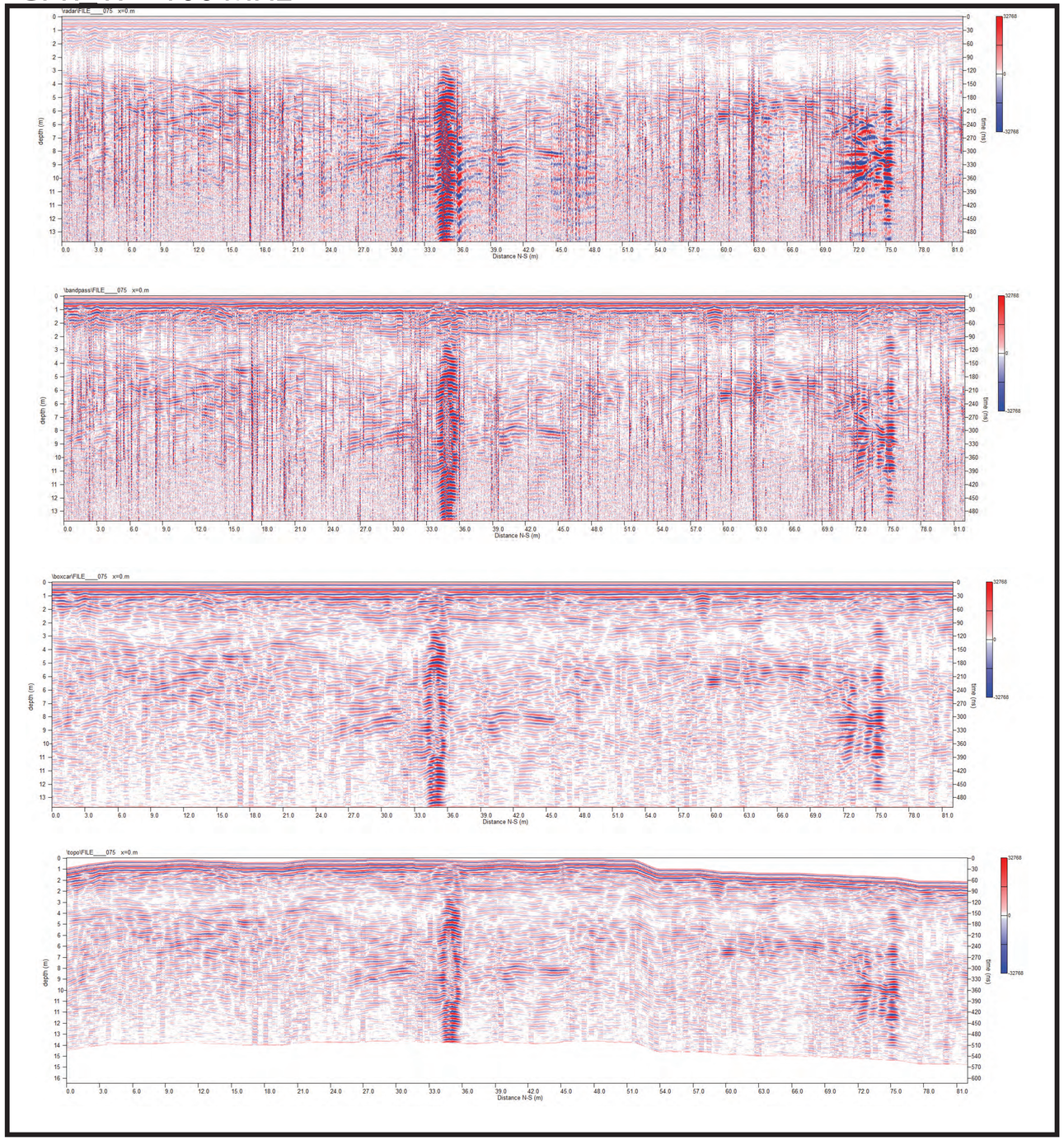

GPR_18 - 200 MHz

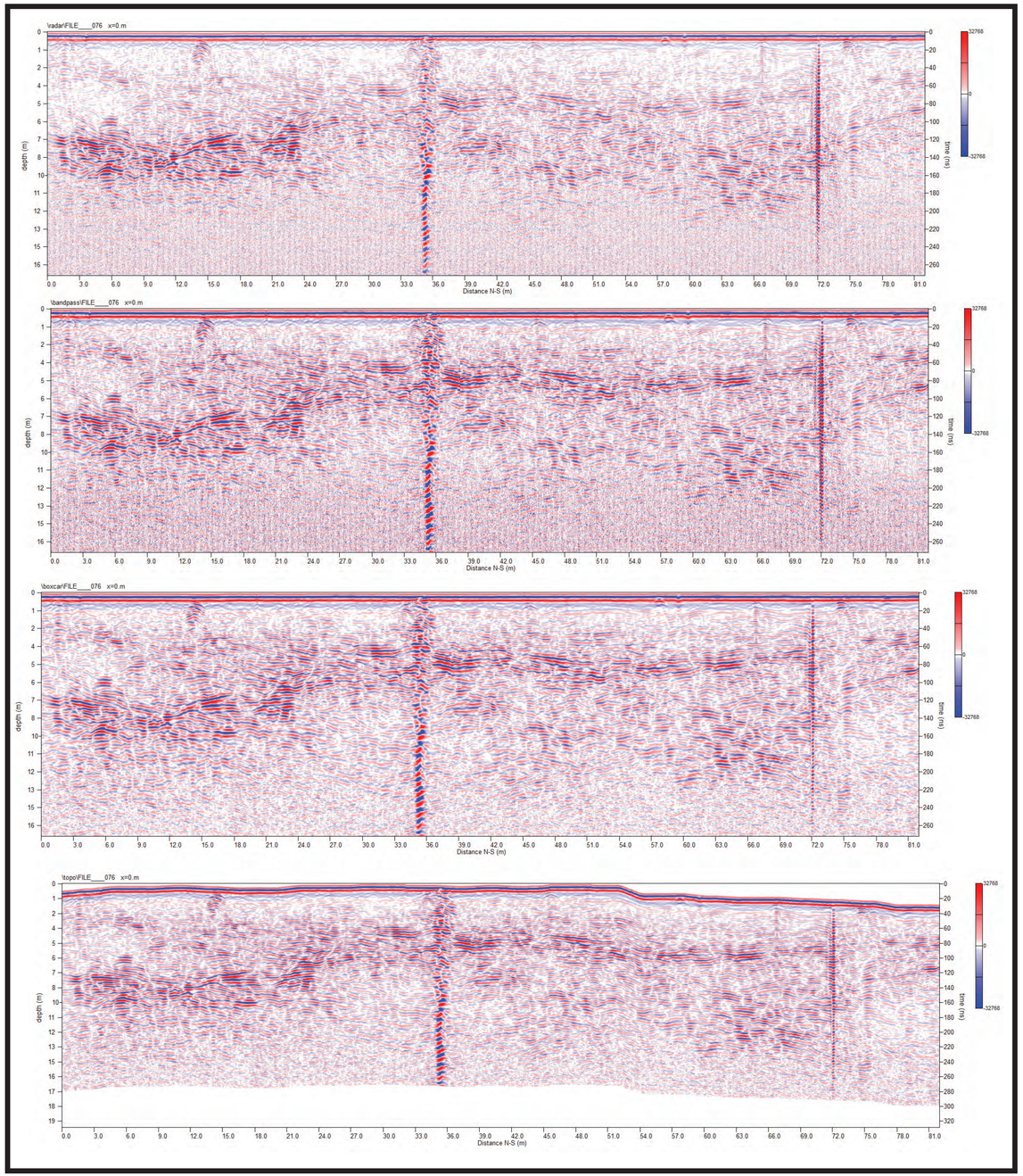

Projection of F2-6

S

N

0

Depth (m)

R6

1796 Ohm-m 23839

9.6

0

Depth (m)

R5

790 Ohm-m 50000

19

0

Distance along profile (m)

81

0

0

GPR16_100 MHz

540 ns

22 m

0

80.2 m

0

0

540 ns

22 m

0

80.2 m

0

0

GPR19_200MHz

340 m

17 m

0

80.2 m

GPR 1: S

N

0

0

150 ns

8.4 m

0

87.3 m

0

0

210 ns

400 MHz

15.3 m

0

341.6 m

GPR_16

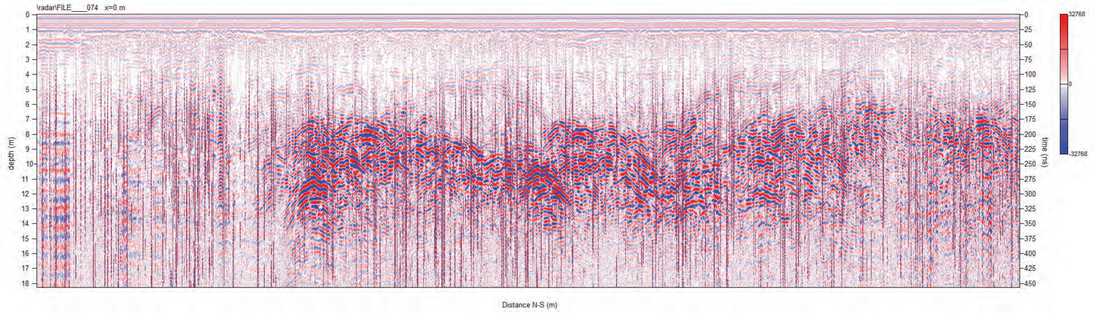
\radar\FILE____074 x=0.m
depth (m)
time (ns)
Distance N-S (m)

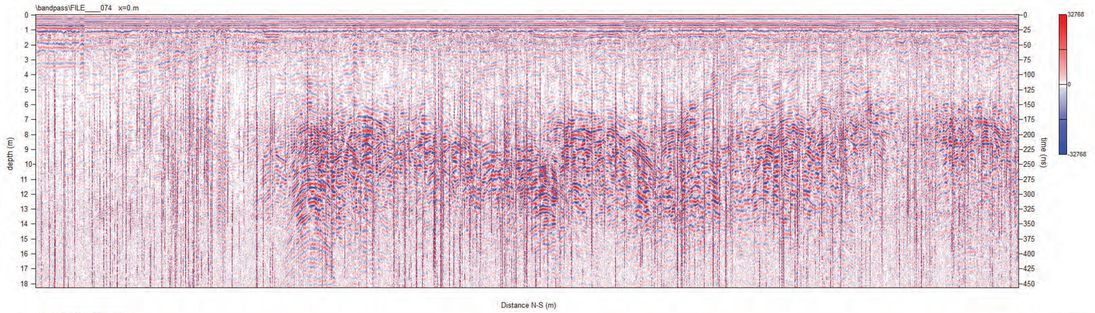
\bandpass\FILE____074 x=0.m
depth (m)
time (ns)
Distance N-S (m)

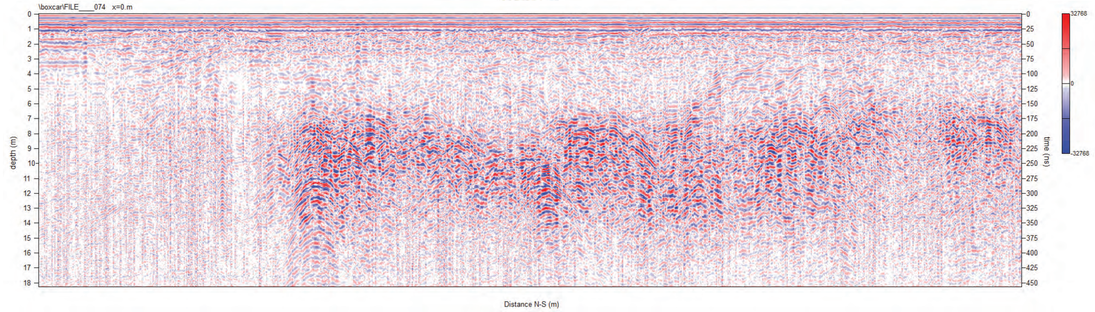
\boxcar\FILE____074 x=0.m
depth (m)
time (ns)
Distance N-S (m)

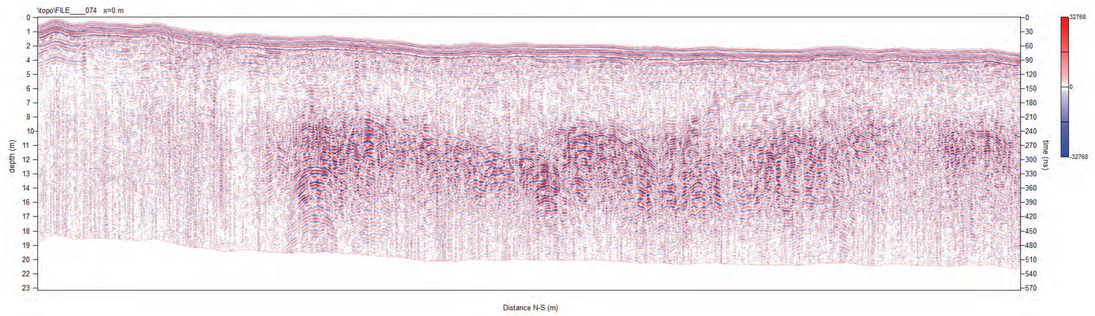
\topo\FILE____074 x=0.m
depth (m)
time (ns)
Distance N-S (m)

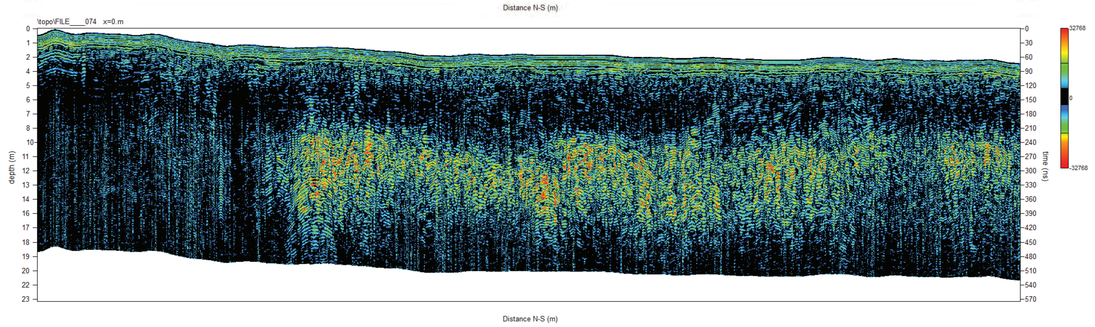
\topo\FILE____074 x=0.m
depth (m)
time (ns)
Distance N-S (m)

GPR_19

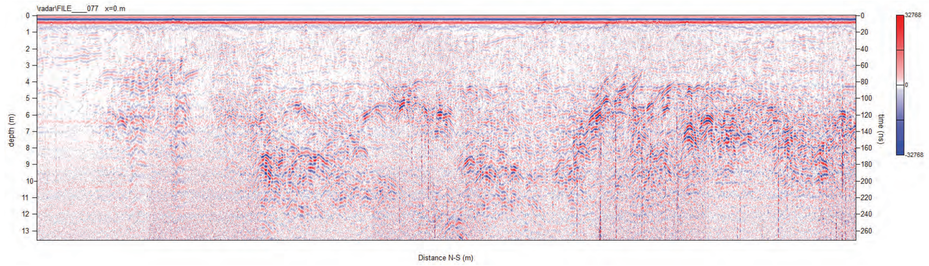
\radar\FILE____077 x=0.m
depth (m)
time (ns)
Distance N-S (m)

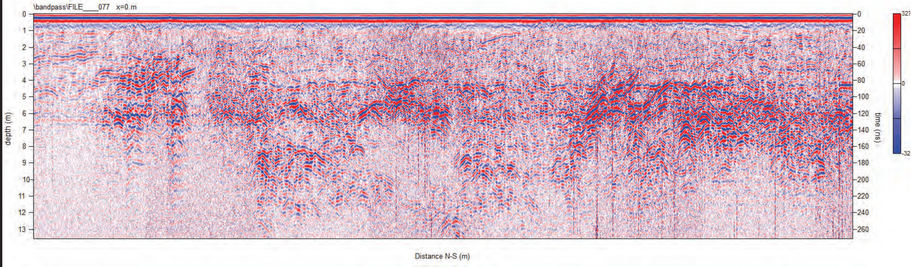
\bandpass\FILE____077 x=0.m
depth (m)
time (ns)
Distance N-S (m)

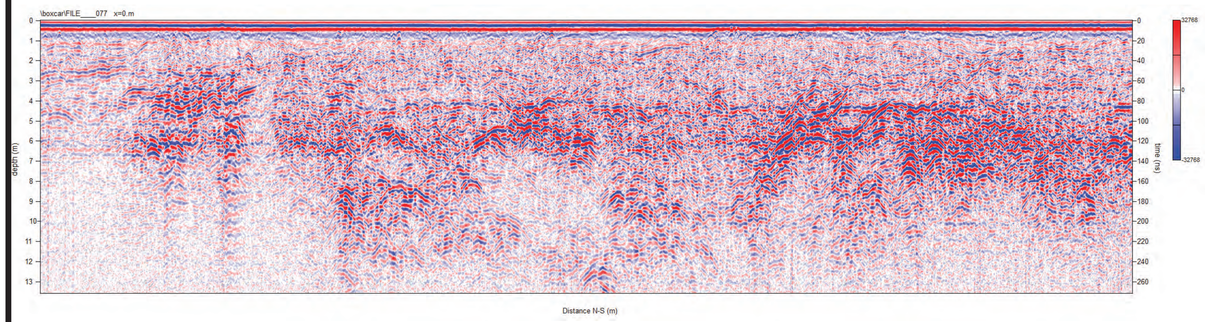
\boxcar\FILE____077 x=0.m
depth (m)
time (ns)
Distance N-S (m)

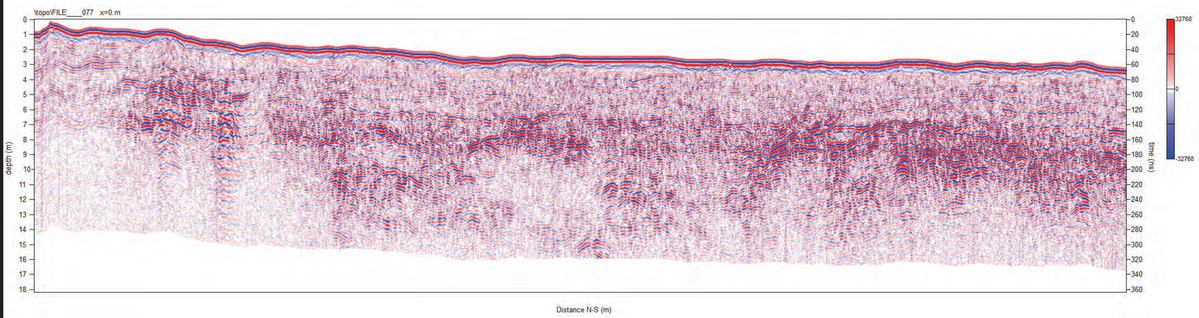
\topo\FILE____077 x=0.m
depth (m)
time (ns)
Distance N-S (m)

GPR_1a

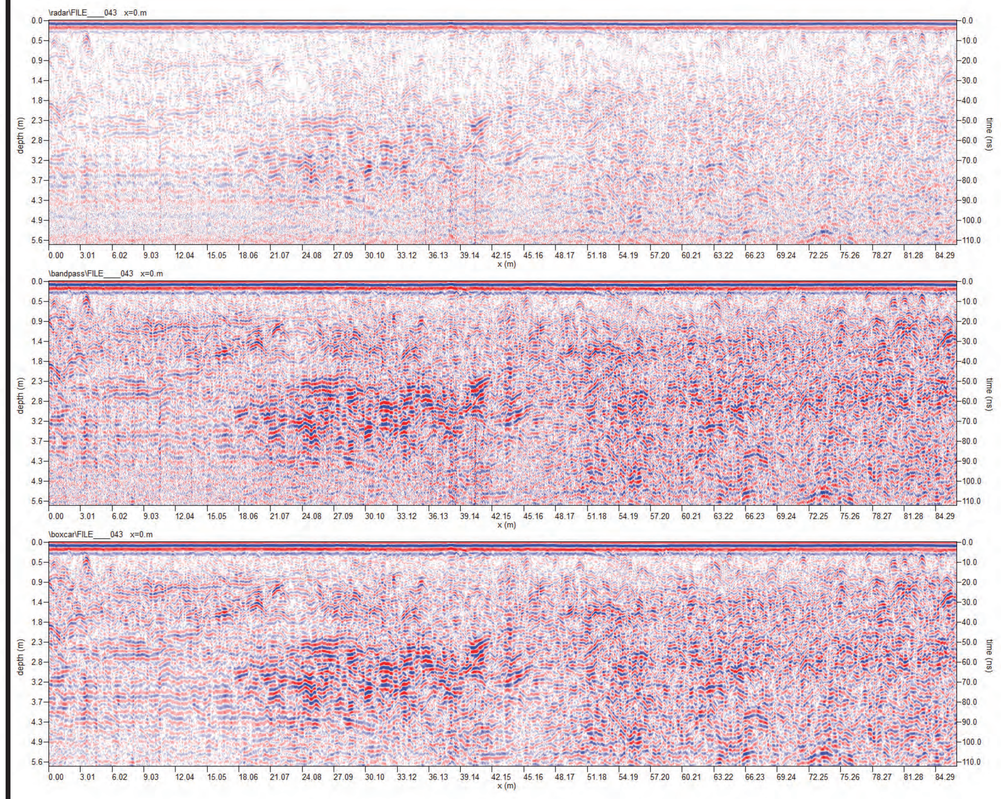
\radar\FILE____043 x=0.m
\bandpass\FILE____043 x=0.m
\boxcar\FILE____043 x=0.m
depth (m)
time (ns)
x (m)

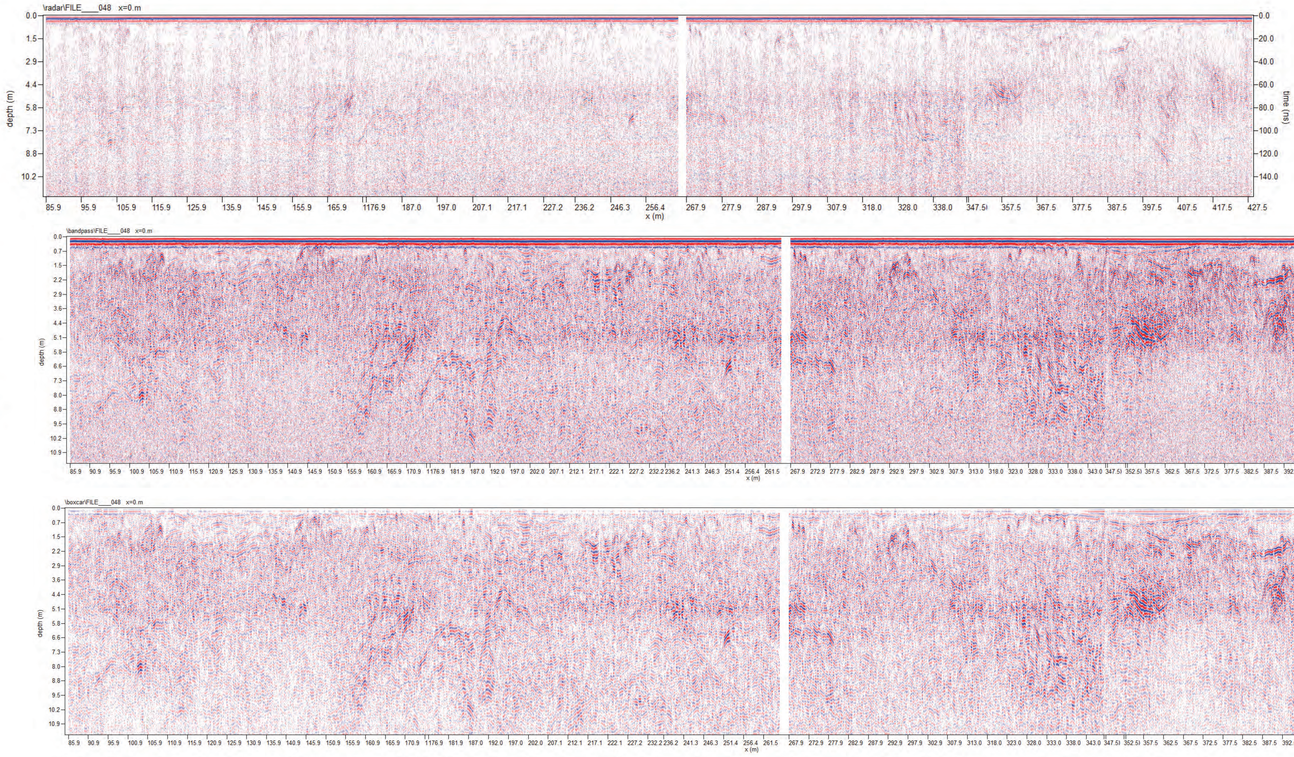
\radar\FILE____048 x=0.m
\bandpass\FILE____048 x=0.m
\boxcar\FILE____048 x=0.m
depth (m)
time (ns)
x (m)

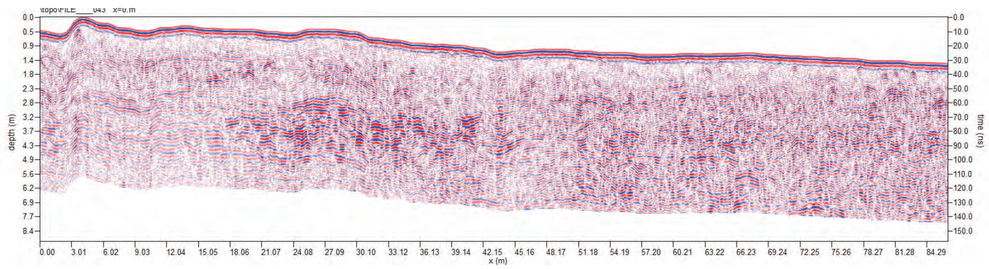
\topo\FILE____043 x=0.m
depth (m)
time (ns)
x (m)

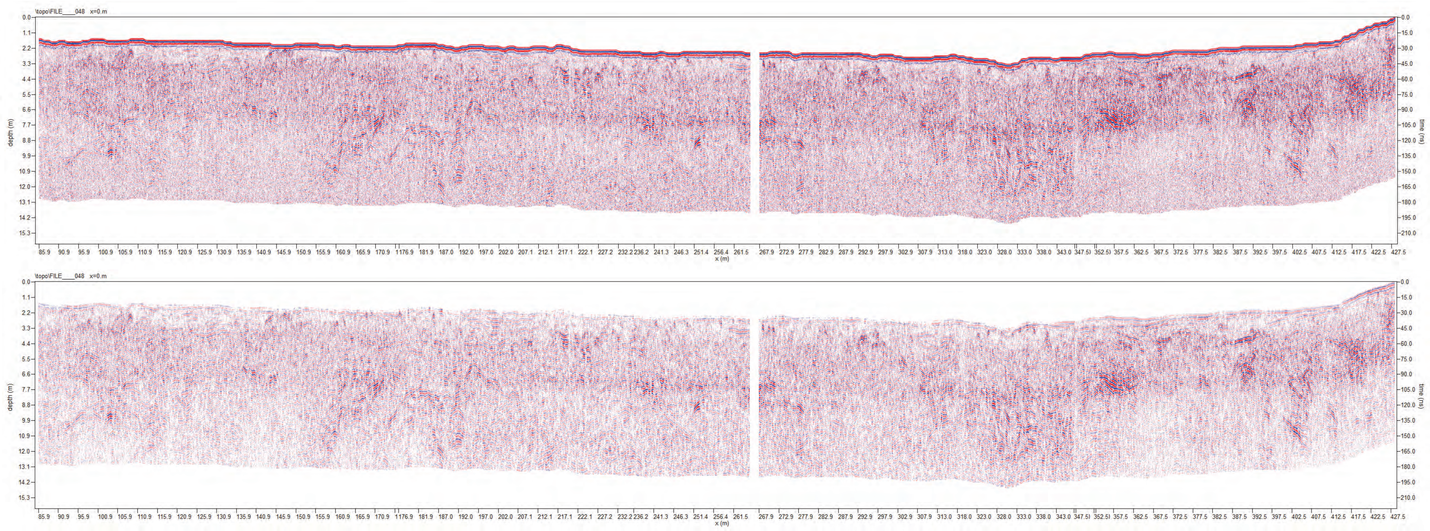
\topo\FILE____048 x=0.m
depth (m)
time (ns)
x (m)

Qt1 Leech, two exposures, RC5, RC 6, OSL 3

2015-AG-102 upper terrace quarry exposure - weak eastward imbrication of gravels 123°42'44.754"W 48°29'45.159"N

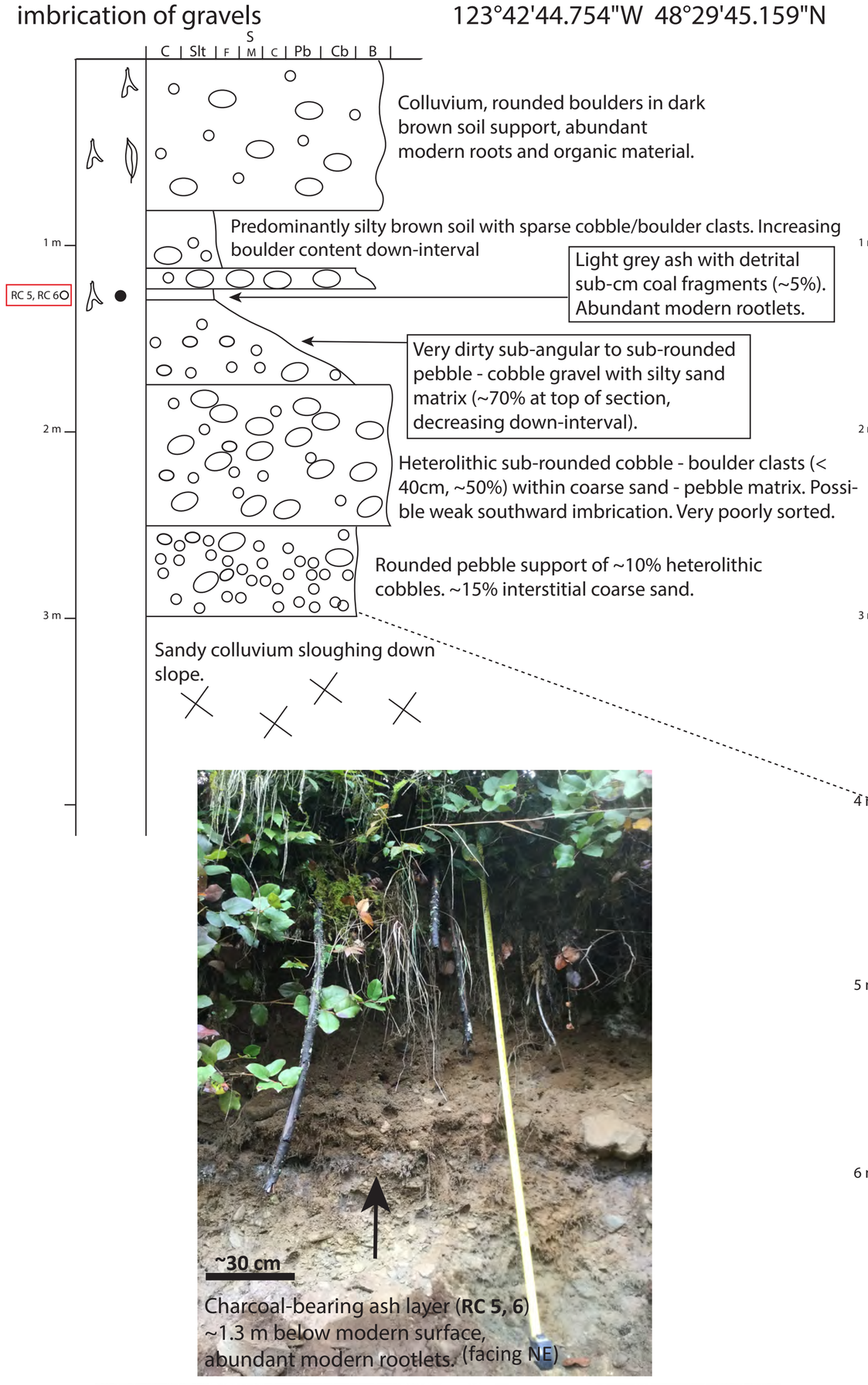

Charcoal-bearing ash layer (**RC 5, 6**) ~1.3 m below modern surface, abundant modern rootlets. (facing NE)

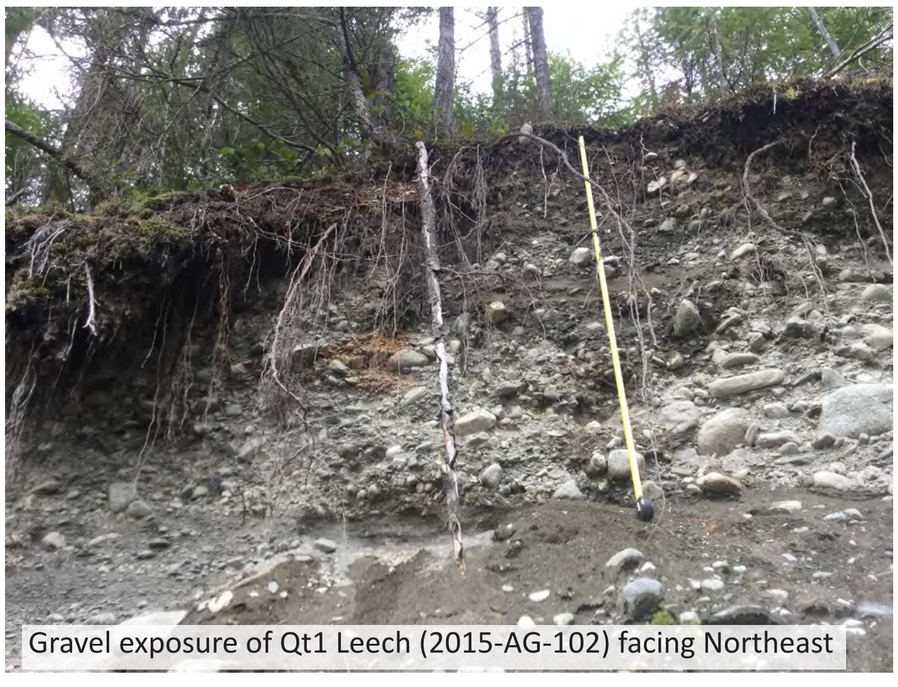

Gravel exposure of Qt1 Leech (2015-AG-102) facing Northeast

2015-AG-013 High terrace exposed north of the bridge, Leech River (by the bridge) 123°42'48.834"W 48°29'43.595"N

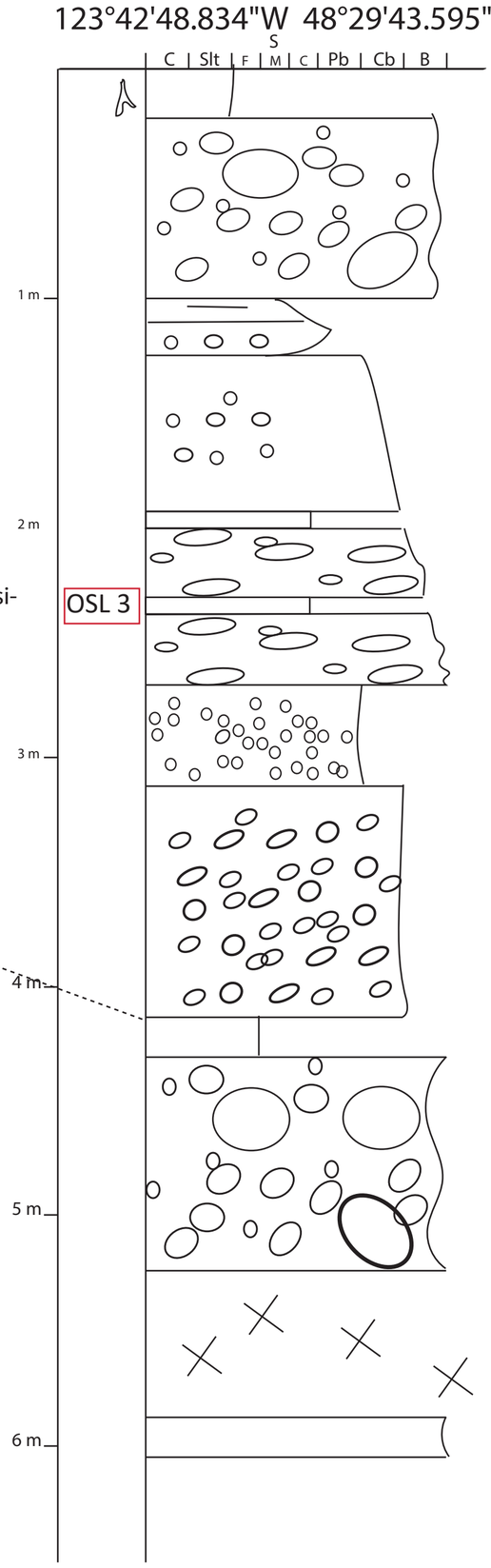

1. Modern fine dark brown soil.

2. Cobble to boulder heterolithic subrounded poorly sorted clast support of ~40% coarse-grained sand / silty matrix.Weak eastward imbrication. Clasts are 60 - 80 % schist, 10 - 20% medium-grained intermediate intrusive, <5% mylonite, ~10% other.

3. Discontinuous layers of coarse-grained sand and rounded pebbles.

4. Sub-rounded pebble to cobble , ~70% sub-spherical heterolithic clasts within coarse-grained sand matrix. Discontinuous layers of course-grained sand with moderate clay content (OSL 3) (~5%). Generally fining-upward sequence. Weak eastward imbrication. Clasts are 60 - 80 % schist, 10 - 20% medium-grained intermediate intrusive, <5% mylonite, ~10% other.

5. Very well-sorted rounded pebbles.

6. Moderately well-sorted gravel, very similar to Unit 4, lacking large boulders. ~30% sandy matrix. Weak eastward imbrication. Clasts are 60 - 80 % schist, 10 - 20% medium-grained intermediate intrusive, <5% mylonite, ~10% other.

7. Weakly undulating silty to medium-grained sand bed. ~5cm of normal offset along a north-dipping plane observed.

8. Very poorly sorted cobble to boulder (~50%) within a coarse-grained sand to cobble matrix. Exposed again ~6m below top of terrace on west side of exposure.

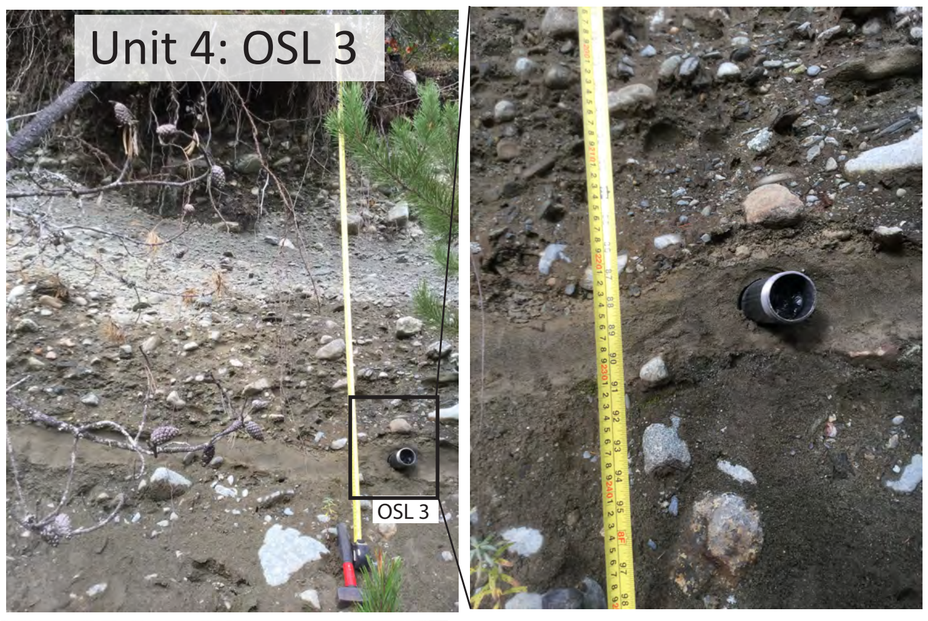





Qt4 Stratigraphy, east side of the Sooke River, terrace surface associated with eastward flow on the Leech River : 48.493328°N, 123.713062°W





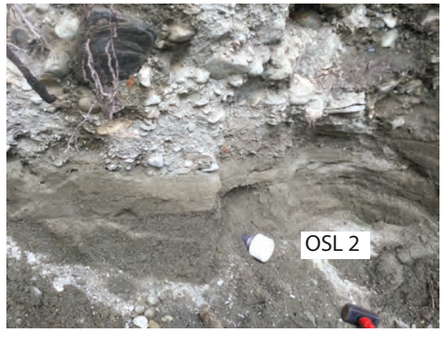

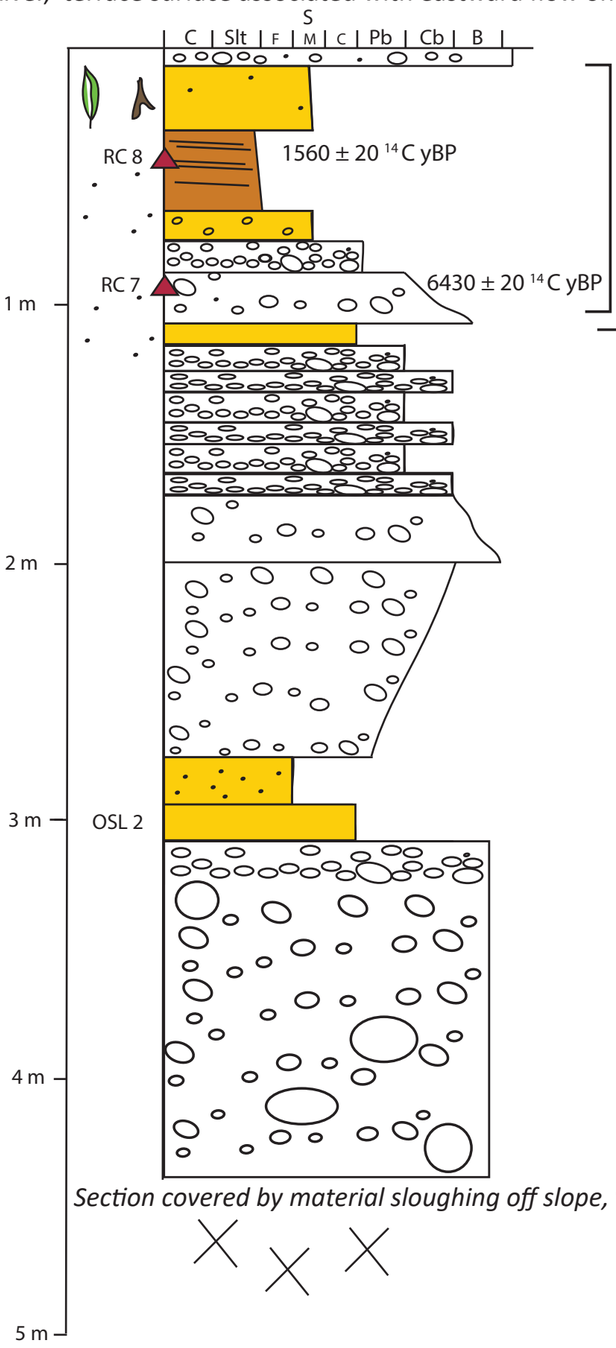

Section covered by material sloughing off slope, ~1 m above modern Sooke River

Unit 5: Generally ~1 m but up to 2 m thick, cobble-boulder gravel generally fining upwards from boulders at base to pebbles and cobbles at top. Boulder layer at base is open-work clast-supported, chaotic fabric, some weak south-dipping imbrication. Up to ~30% schist; unit grades up into pebble-cobble gravel (clast-supported with coarse sand matrix fill to open work). Clasts are rounded to subrounded, no cementation observed. Upper ~50 cm is grey silt to fine sand (probable overbank sands). Lower contact is clear, moderately undulaty up to 1 m deep over 3-4m wavelength. Well exposed for 15 - 20 m.

Unit 4: (4b) Discontinuous cm-scale interbeds of coarse sand granules, rounded pebbles, and cobbles (~20%). Clasts predominantly schist (~70%), strong southward imbrication. Bedding is weakly undulatory, gently dipping to the South.

(4a) Sub-rounded pebbly groundmass support of rounded heterolithic cobbles-boulders. Coarse sand and minor silt interstitial (10 - 15%). Gently imbricated towards the south. Increase in boulder content down-interval.

Unit 3: Clast-supported matrix-fill to open-work cobble to boulder gravel. Matrix is coarse sand to pebble. Clasts are mostly boulders (70%), ~30% small to large cobbles. Clasts are rounded to sub-rounded, highly varied in lithology (relatively few Leech River schist clasts, which is more predominant in the matrix (~50%, sub-angular to sub-rounded). Very crude stratification of bouldery layers with interbedded sandy pebble-cobble lenses (decimetre-scale ~20 cm) - discontinuous. Chaotic fabric - possible weak, gentle, north-dipping imbrication - also a few steep dipping large pebble-small cobbles. Matrix fill is mostly subhorizontal as shown by platy schist granules. Minor fine sand and silt in matrix (~5%). Light orange-grey weakly cemented (much less than Unit 1). Few modern roots. Lower contact is distinct and subhorizontal (gently undulatory- 10-20 cm deep and 1-2 m wide). This unit is ~1 m thick, well-exposed over ~15 m , discontinuous over ~30 m.

Unit 2: Well-sorted fine-grained sand with cm-wide tan silty band (~10 cm) above well-sorted, subangular coarse-grained sand (**OSL 2**) Sharp upper contact dips ~10° to the northeast (possibly due to slumping).

Unit 1: Poorly sorted clast-supported heterolithic pebble-boulder gravel with silt- (FG-CG)sandy silt very poorly sorted matrix fill, chaotic fabric. Clasts up to ~25 cm b axes, highly variable grain size distribution with irregular lenses of medium-coarse-grained pebble gravel with sandy-silt matrix. Sparse silt lenses <10 cm^2 adjacent to boulders. Clast fabric varies from chaotic to locally well-developed clast alignment dipping ~20° S (possible channel/bar edge?) In the central portion of the exposure over 1.5 m near vertical (70-80°dip) clast alignment (possible channel/bar margin) restricted to lower portion, not observed in upper 30 cm. Clast composition is heterolithic with abundant diorite, Leech River schist, rounded to sub-angular, predominantly subrounded. Matrix is dense, light beige-grey, possibly cemented. Very few rootlets. Lower contact is covered by sloughing colluvium, ~1 m above modern Sooke River (June 16 ,2016). Mylonitic EMe outcrop at southern end of exposure. This unit is ~1.3 m thick, exposed over ~8 m at the south end of 2015-AG-106 exposure, interpreted as a proximal glaciofluvial deposit due to the poor sorting and silt-rich matrix.

Exposure of inset channel in southern *Qt6*, east of the Sooke River: 48.490°N, 123.716°W

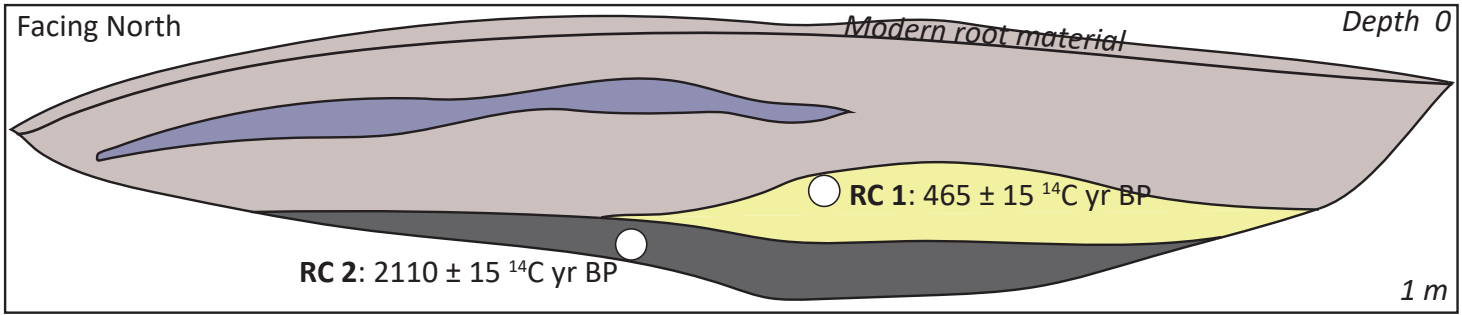

Heterolithic rounded pebble - cobble lens with ~70% sandy matrix support.

Medium grained dark brown sandy loam

Coarse grained schistose sand- granules with ~5% pebbles, cm-scale woody debris
Silty loam matrix ~20%

Weakly laminated dark orange-brown schistose clay rich silt - fine-grained sand.
Sparse mm-scale charcoal fragments, increase in orange colouration towards top of unit.

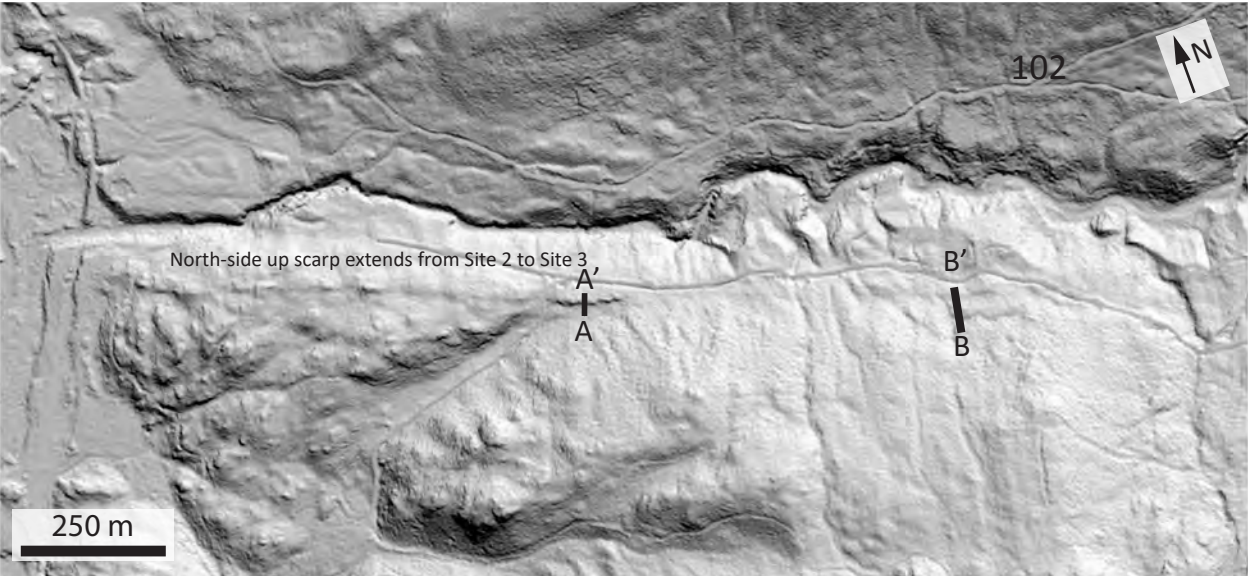

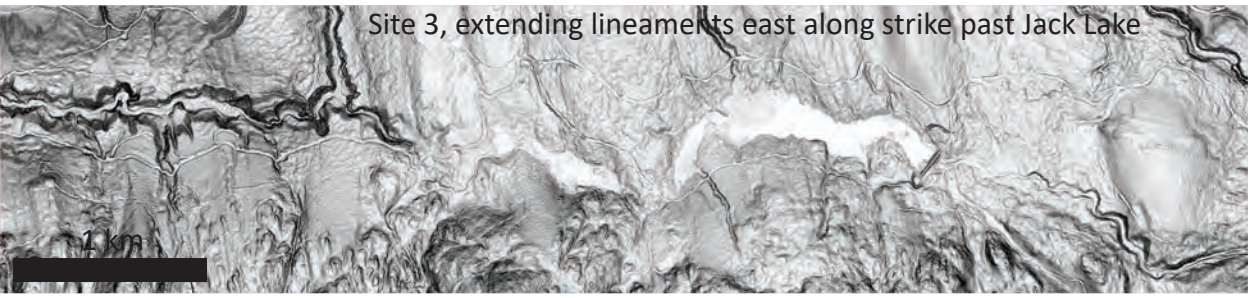

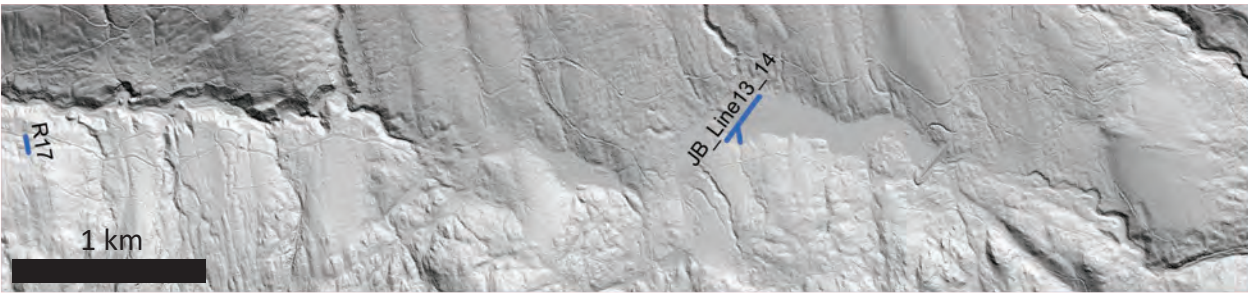

*The GPR data from Bednarski (2016), Line 3, was rotated into alignment with our resistivity profile (R18)
Note also how the linear southern boundary of Jack Lake extends to the east into subparallel bedrock scarps protruding from a till hill.

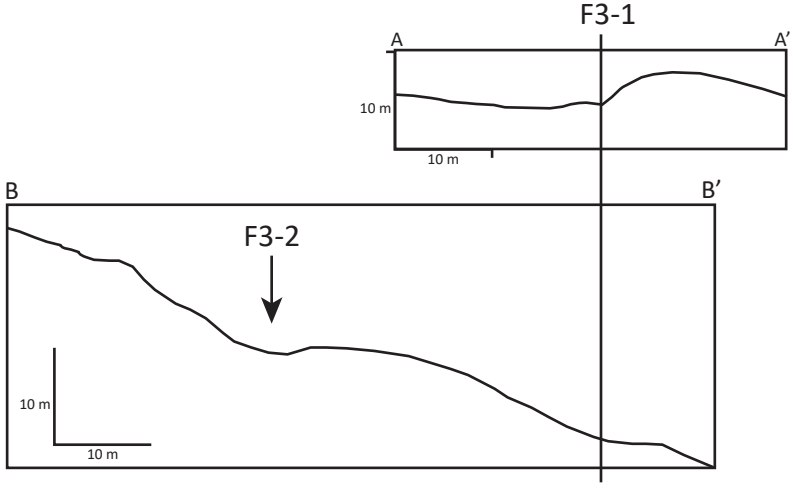





Clusters of euhedral pale blue very soft (H<2) asbestisform mineral on quartz-epidote-chlorite fault plane indicating components of normal slip-sense at Site 3-D. Mineral is unknown, I speculate it may be a serpentine alteration (chrysotile), or prehnite, and interpret these faults as being accretionary (e.g. Timpa et al., 2005).





Oxidized gouge-bearing seams within shear zone (F3-2) at Site 3-A. This style of scaly fabric has been documented on the San Andreas fault at depth (Bradbury et al., 2011), and on the Japan Trench (Kirkpatrick et al, 2014). On right panel, note cm-scale clay seam crosscutting scaly fabric, suggesting a reactivation of the mature structure.



~8 m wide, water conduit clay rich fault zone at Site 3-2 (F3-5)

Site 3 GPR & Resistivity (See Fig. 10)

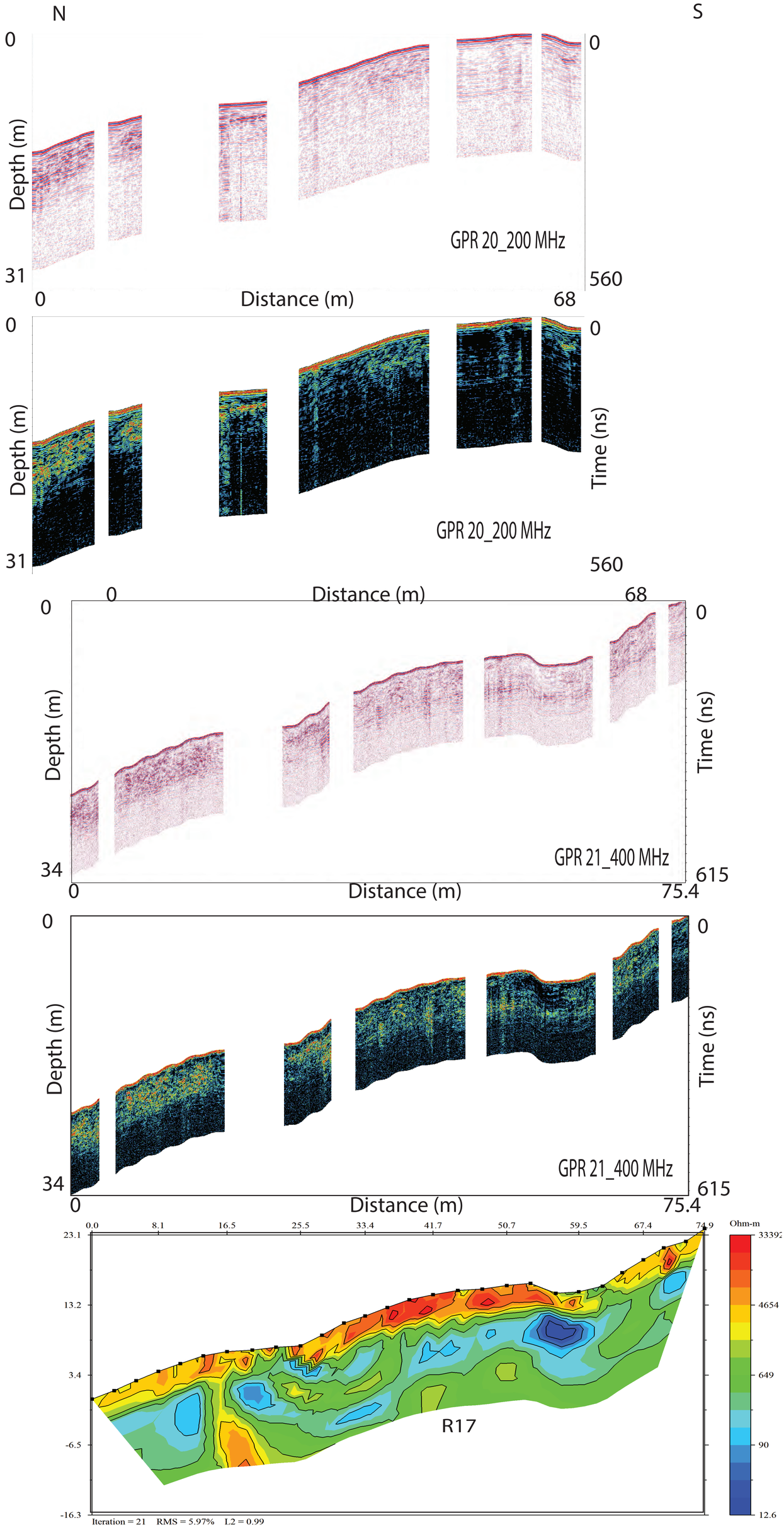

GPR_20a

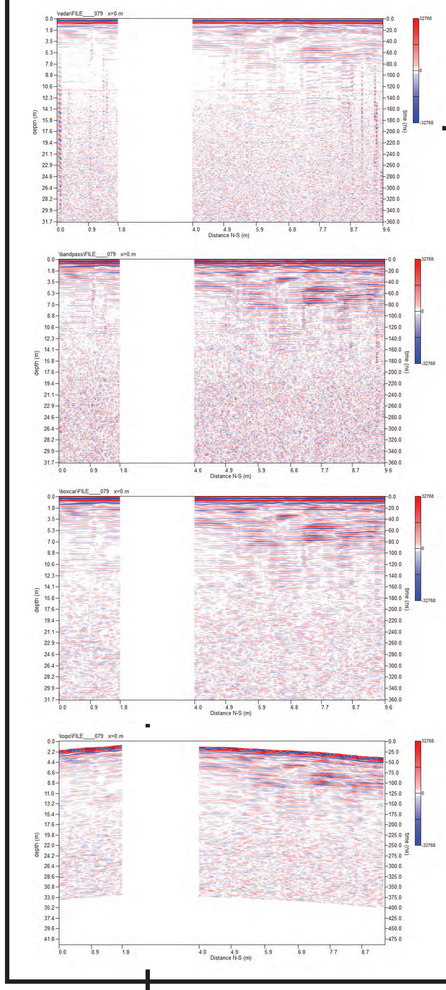

GPR_20

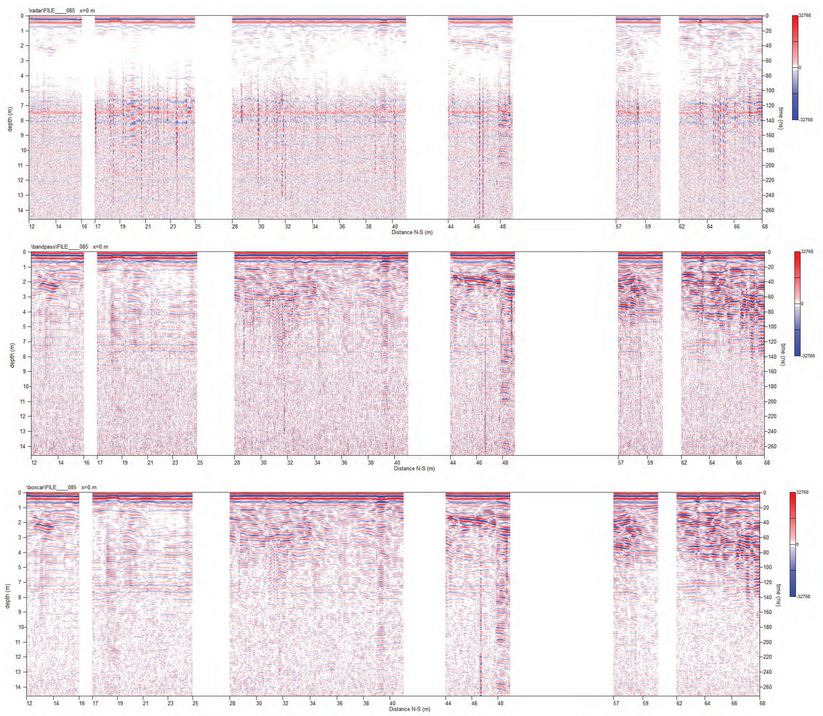

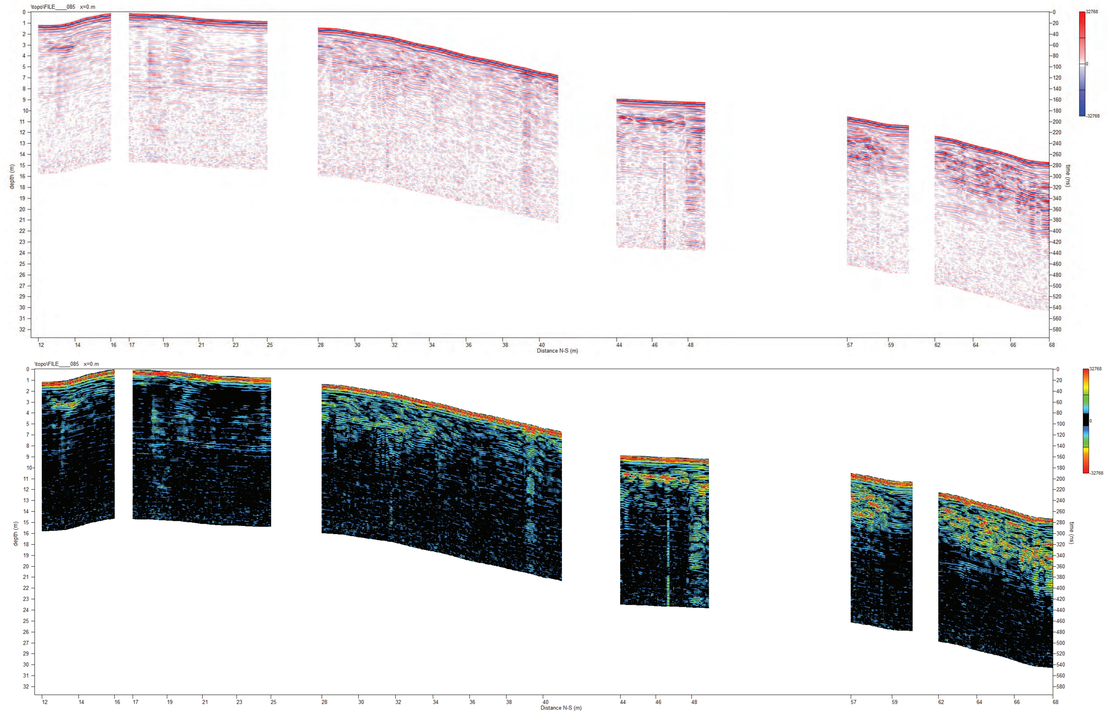

GPR_21

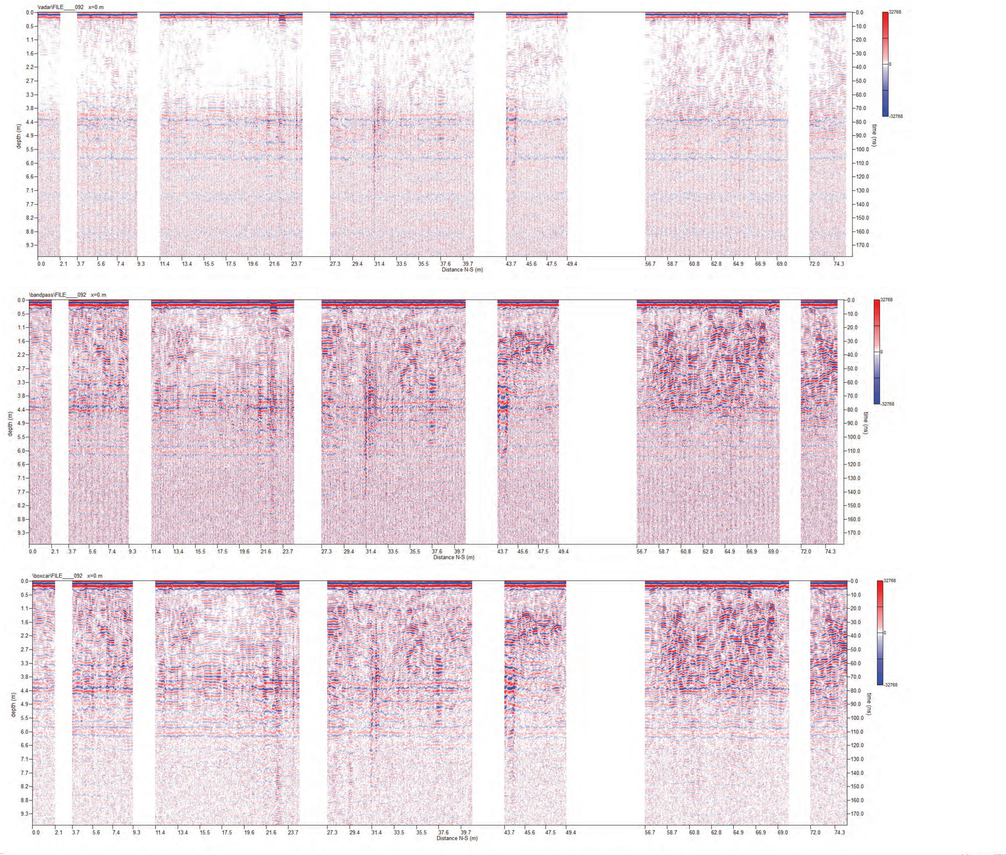

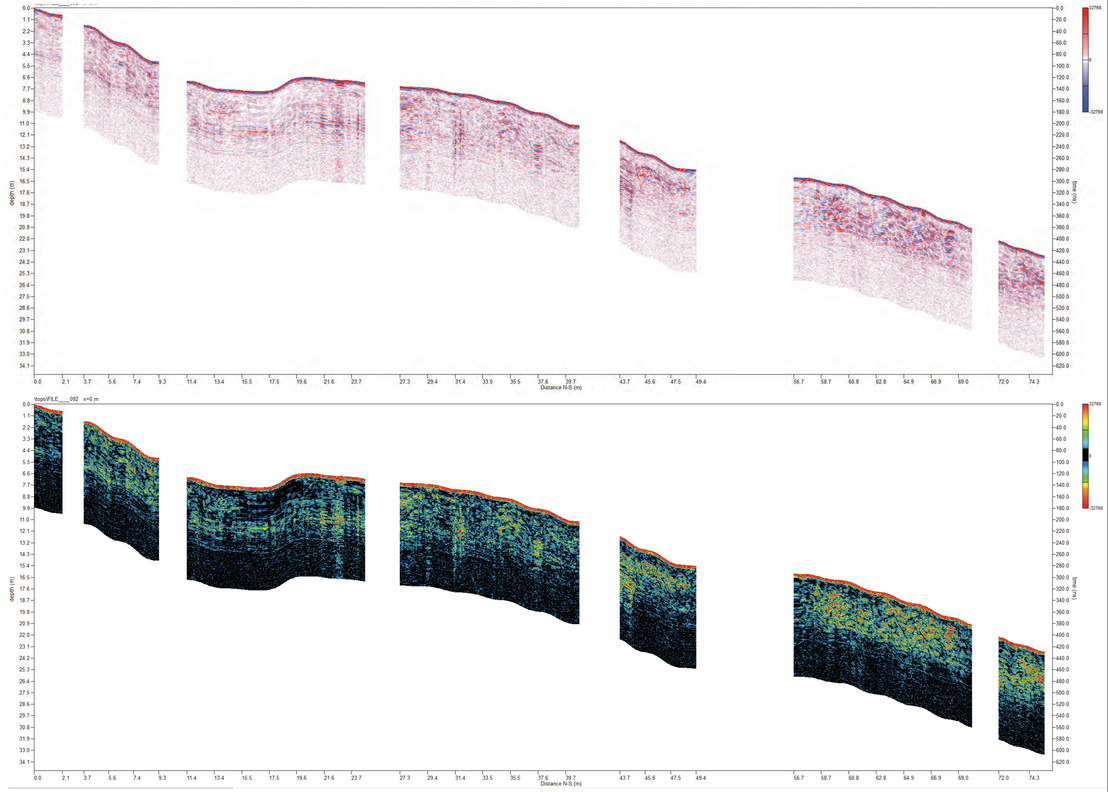

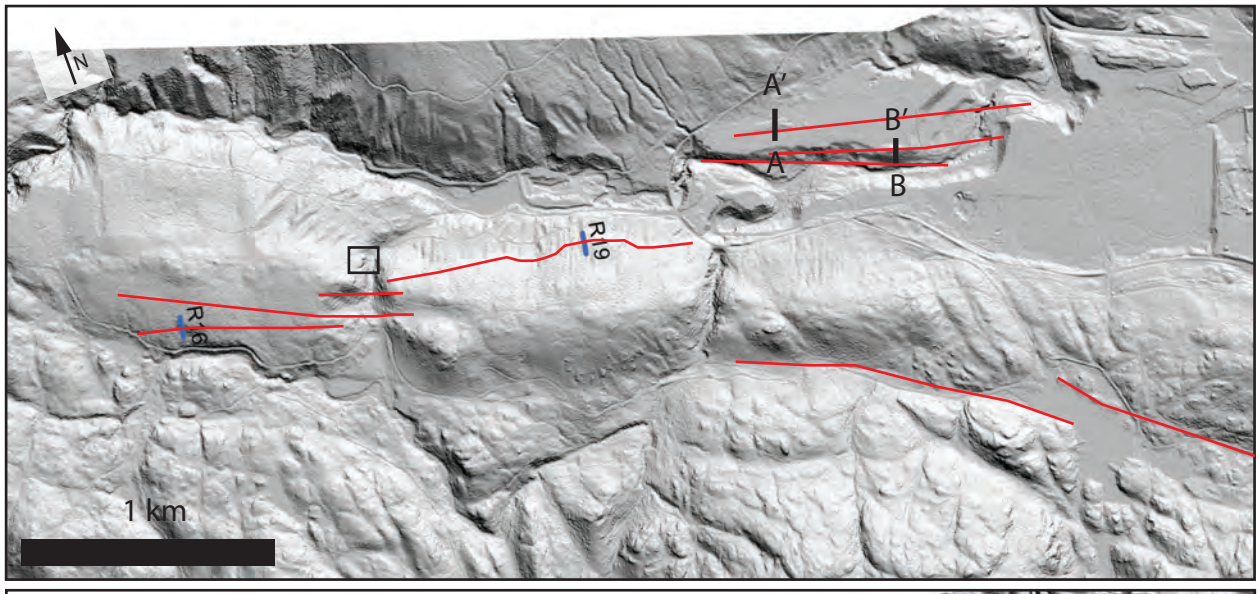

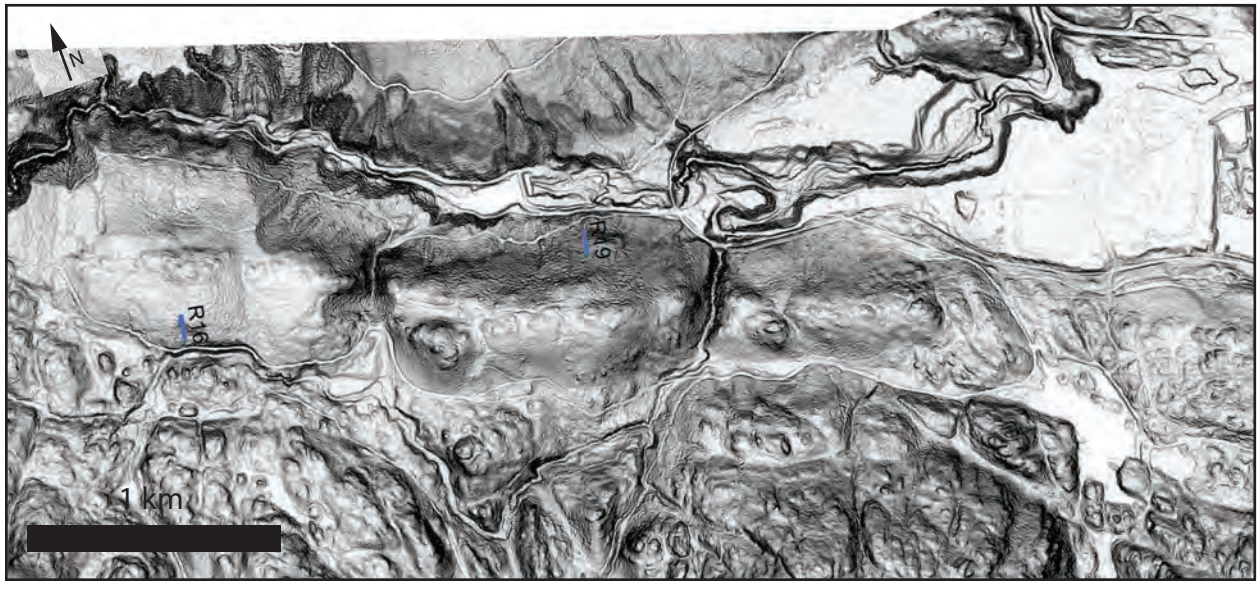



F4-2, in Old Gov't Gully (see hillshade)

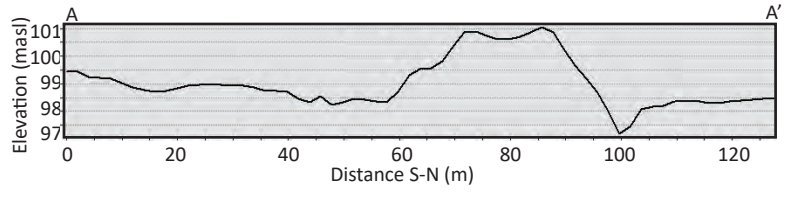

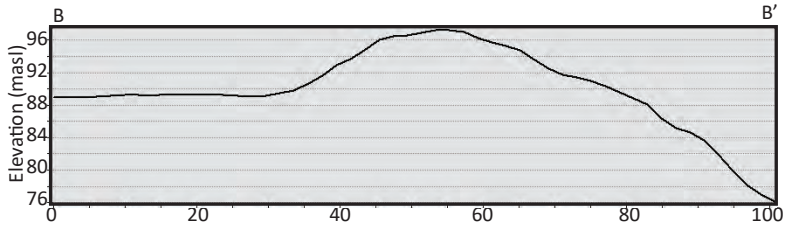



Bench between two breaks in slope on R19 survey line
(Possible old logging road)
Looking west across R19 profile.



Upper scarp traversed by R19,
~100 m along strike to the east (facing west)

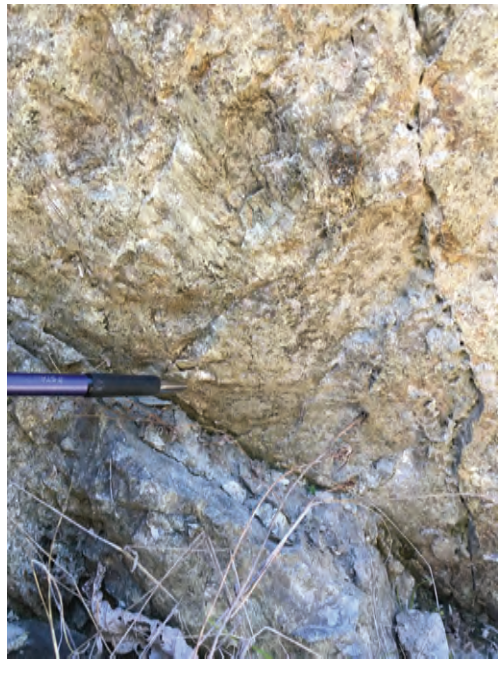

Bimodal slickenlines on **F4-1**, at Site 4-A. (333°/75°E)

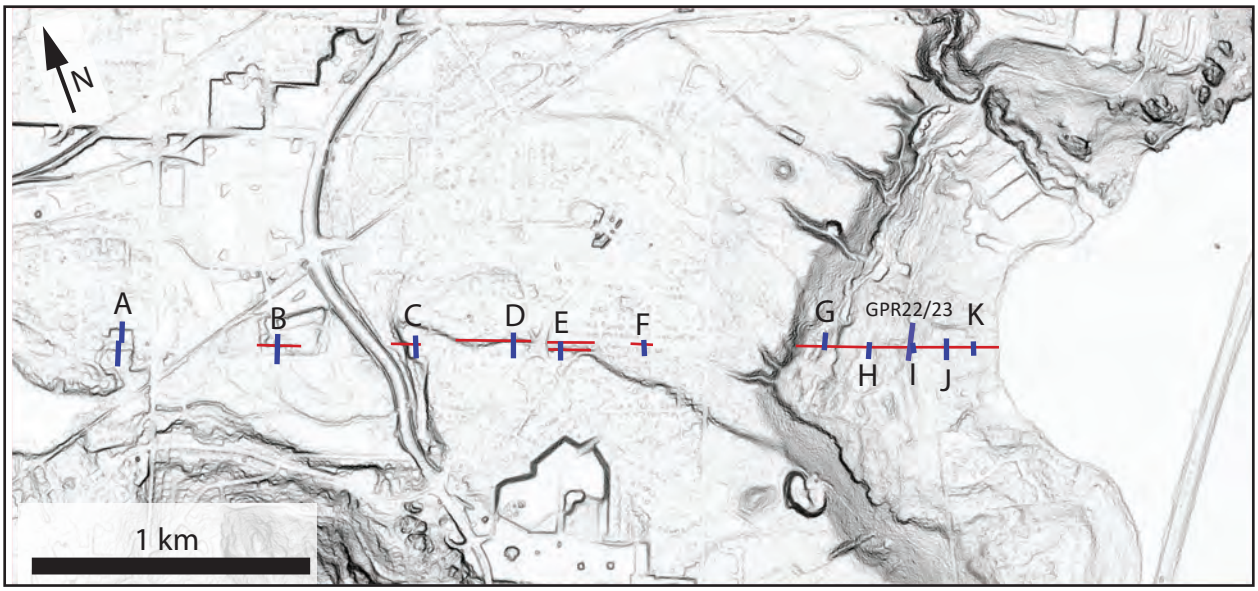

N S

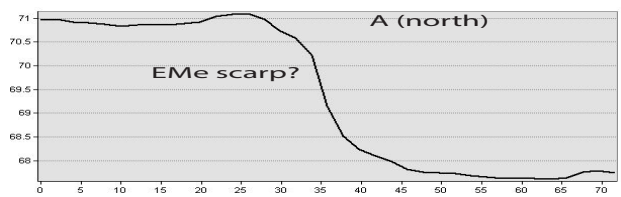

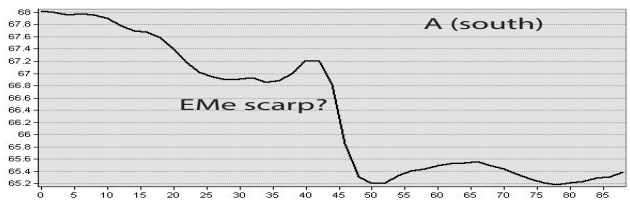

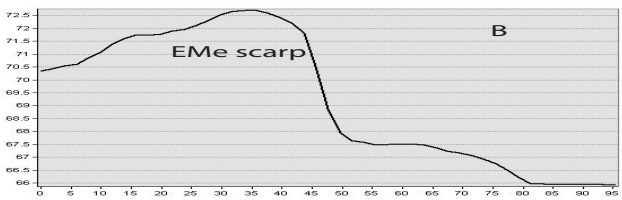

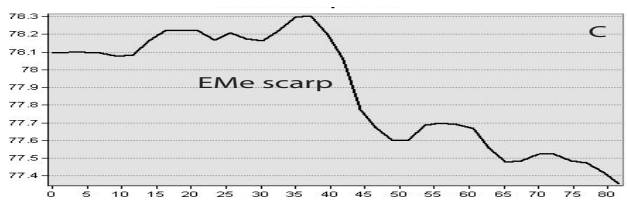

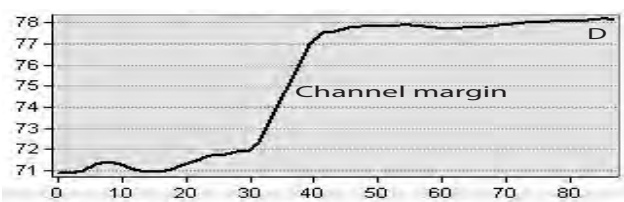

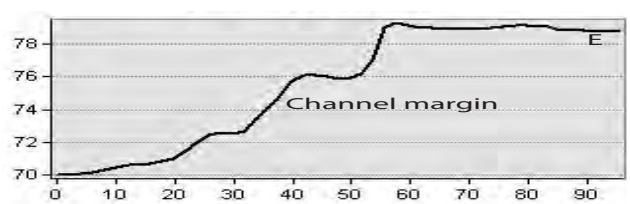

N S

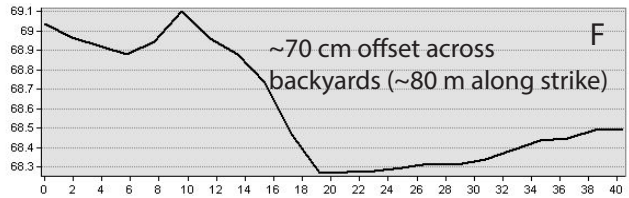

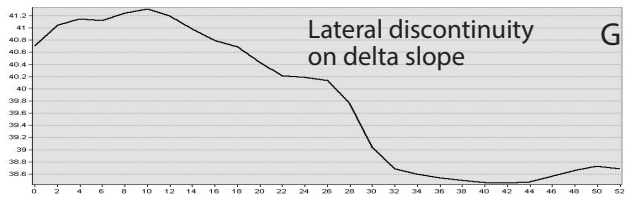

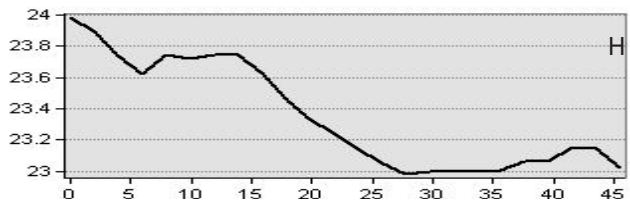

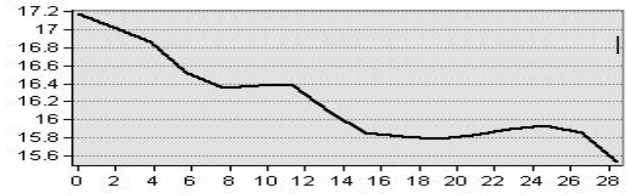

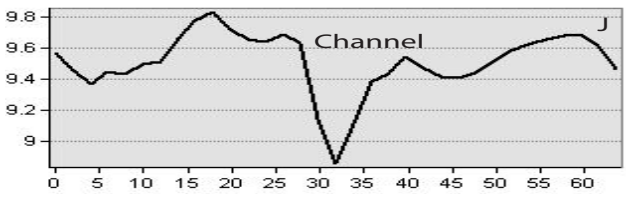

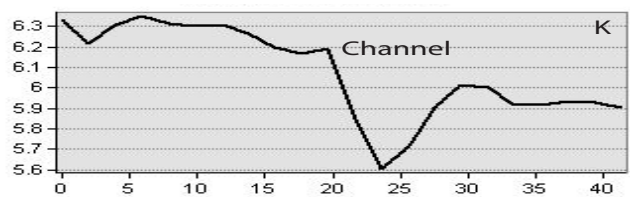

*Note varying scales and vertical exaggeration

Site 5 Colwood Delta slope image



Site 5 Colwood Delta aspect image

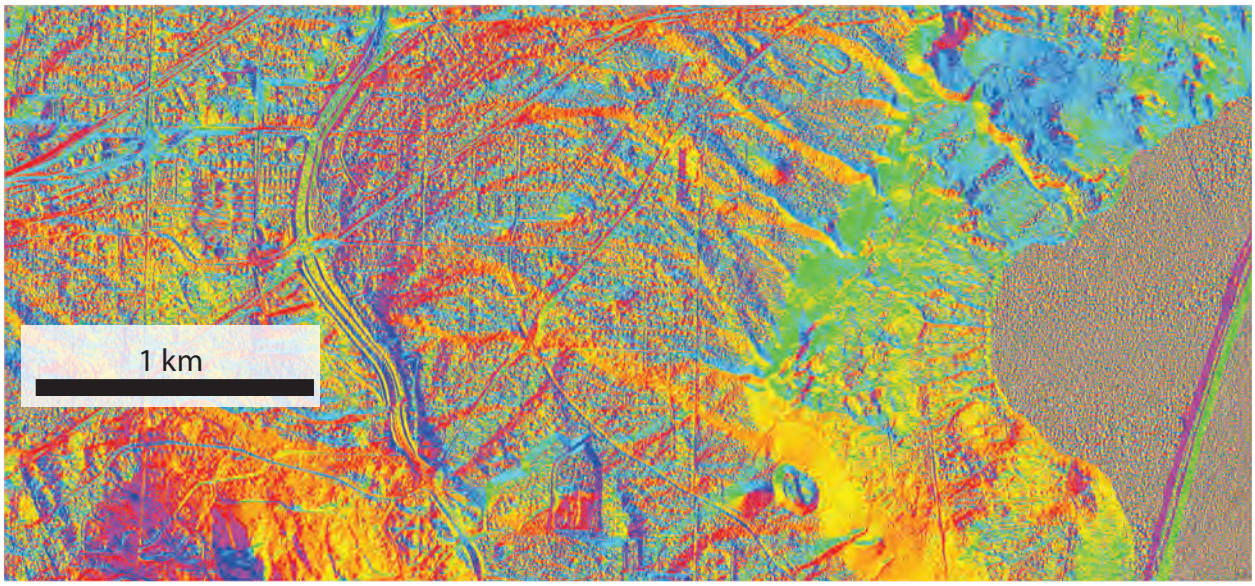

E1

'2016-fig-047'

109



See Notebook - Mosaic 2

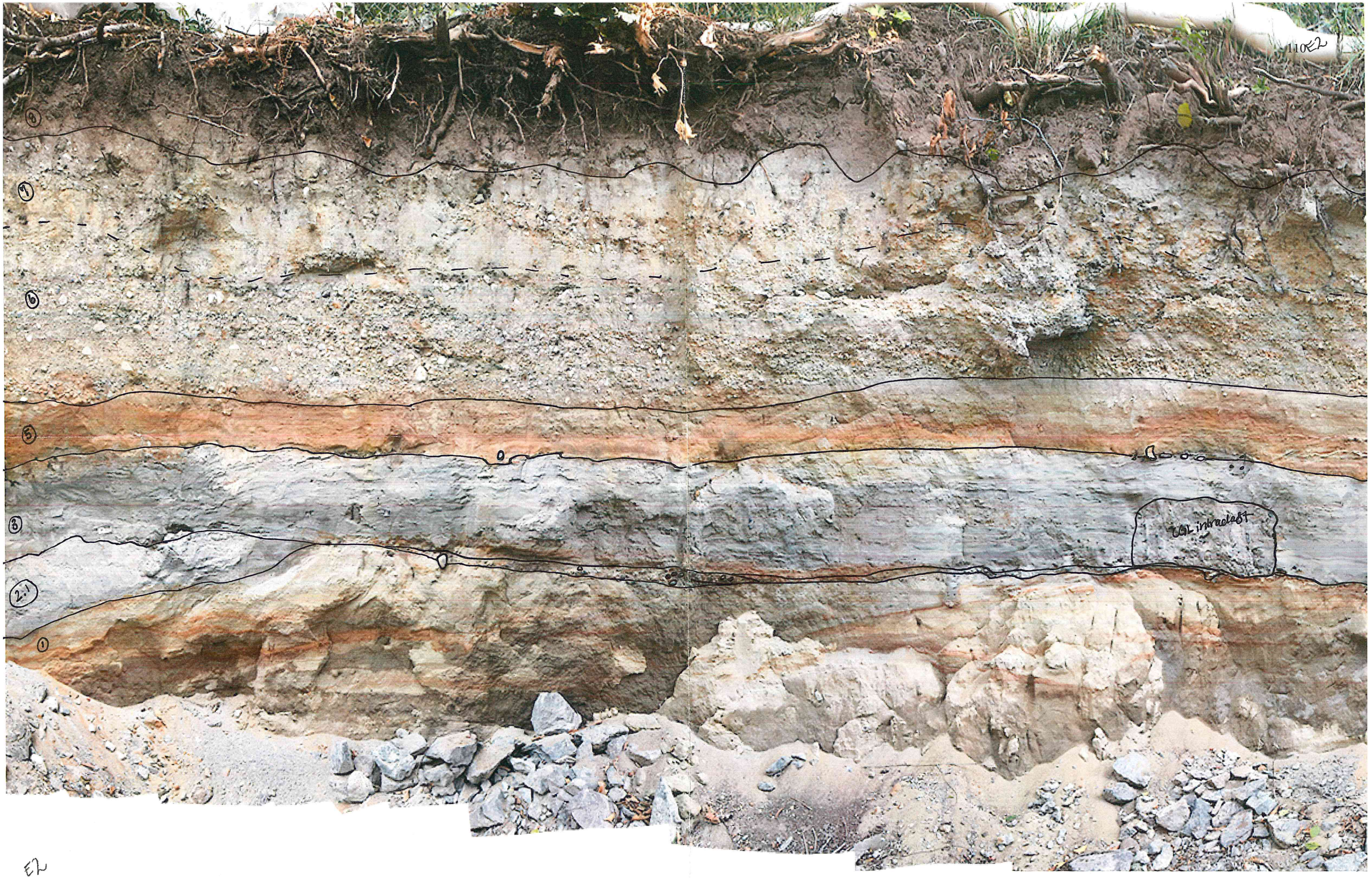

E2

E3



E4

③

⑦

⑥

⑤

④

①

E5



Eb



E7



e) dk gy cly <1mm striae on gently undulating fracture plane □
Rake ~90° ∅ laminae - Rep PL-1

f) lt gy MAB-Tam(?) slt w/ intercalated mm-scale MG gy sand (sub-vert planes, along apparent shear fabric.)

a) mm-wide wt coating, weak dip-slip grooves?

b) Poss wk grooves rake 20° (plunge S)

c) Rounded peb + sub-rounded slt clasts.

d) slt intraclasts - sub-rounded ≤ 3 cm

'2016-HG-011

E8



ox silty veins

Merged resistivity profile from Maria Thorlakson's Honours thesis (2016)

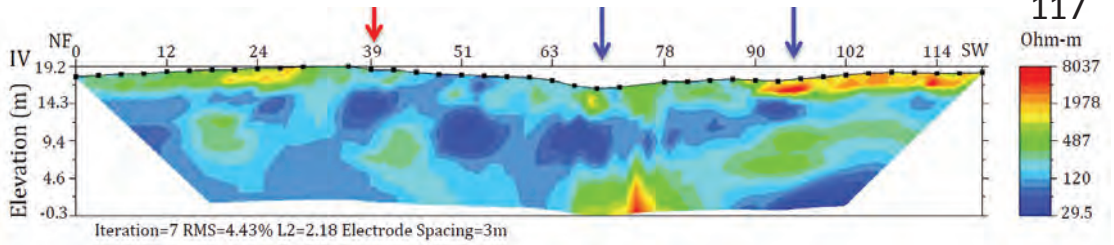

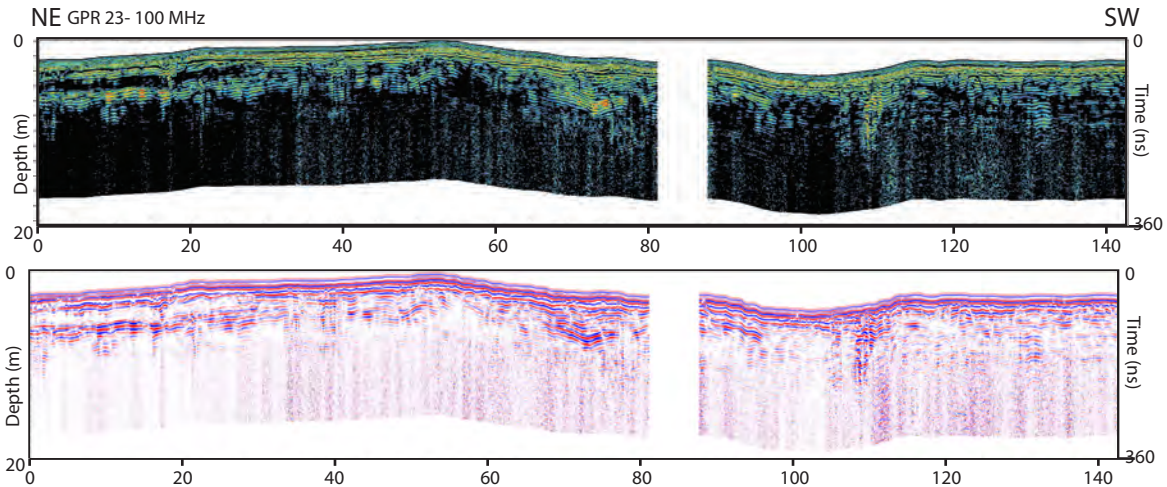

Note: ERT and GPR lines may not be exactly colocated, hence the differences in topography, which are derived from the same LiDAR-derived DEM. We returned to the same site one year later, and attempted to survey the same line, but they may be a few metres different across strike.

GPR 15: Likely imaging a channel margin on the outwash plain of the Colwood Delta (See. Fig. 12A)

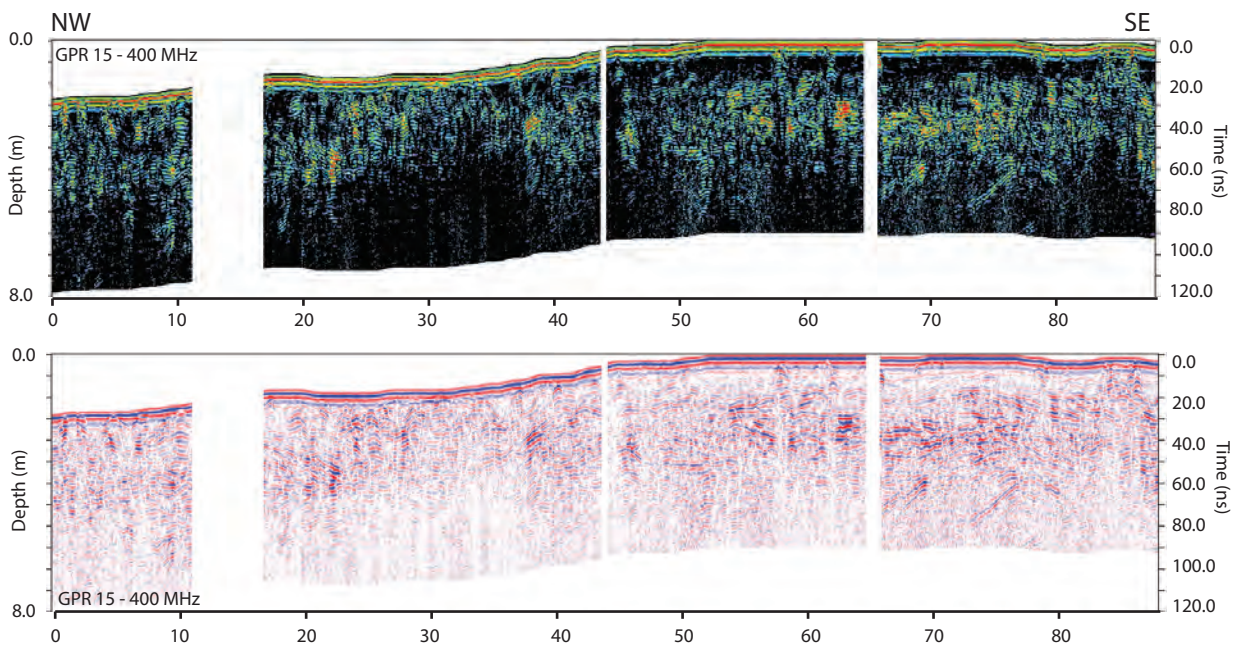

GPR 22: 400 MHz, colocated with GPR 23

